Title
The Influence of Distal Crater Ejecta on Planetary Surfaces: An Investigation of Lunar Cold Spots and Secondary Craters

Author
Powell, Tyler Michael

Publication Date
2023

Peer reviewed|Thesis/dissertation

UNIVERSITY OF CALIFORNIA
Los Angeles

The Influence of Distal Crater Ejecta on Planetary Surfaces: An Investigation of Lunar Cold Spots and Secondary Craters

A dissertation submitted in partial satisfaction
of the requirements for the degree
Doctor of Philosophy in Geophysics and Space Physics

by

Tyler Michael Powell

2023

ABSTRACT OF THE DISSERTATION

The Influence of Distal Crater Ejecta on Planetary Surfaces:
An Investigation of Lunar Cold Spots and Secondary Craters

by

Tyler Michael Powell
Doctor of Philosophy in Geophysics and Space Physics
University of California, Los Angeles, 2023
Professor David A. Paige, Chair

Impact craters dominate the landscapes of many planetary bodies. Among their most striking characteristics are their rays: radial streaks formed by high velocity ejecta launched to great distances. This dissertation investigates the influence of distal ejecta on planetary surfaces by studying two classes of features: secondary impact craters and lunar cold spots.

Secondary impact craters form when rock fragments ejected from a primary crater re-impact the surface at high velocity. Individual primary craters have been shown to produce upwards of 10^6-10^9 secondary craters which form nearly instantaneously in geologic time. This has led many to question whether crater chronology models can be applied effectively. In chapter 2, we develop a model for the global accumulation of secondary craters with time for Mars, accounting for the spatial clustering of secondaries. We show that the number of km-scale secondaries produced on Mars may exceed primaries after only a few 100 Ma. However, most secondaries are clustered around their parent primaries, and regions far from large primaries have significantly fewer secondaries than the global average. The crossover diameter between primary and secondary crater production on a typical surface is estimated to exceed 1 km after ∼1-2 Ga, though subsequent crater erasure has significantly influenced

the number of secondaries visible today.

In chapter 3, we produce updated global maps of nighttime temperature for the Moon using data from the Diviner Lunar Radiometer Experiment on the Lunar Reconnaissance Orbiter (LRO). We implement several improvements, including a correction for errors in instrument pointing, which result in a substantial increase in effective resolution. In addition, we develop a model which mostly removes the effect of topography on nighttime temperature by accounting for scattering and emission from the surrounding terrain. These improvements allow smaller and fainter thermal features to be identified than was previously possible.

Lunar cold spots are extensive ray-like regions of reduced nighttime temperature surrounding young impact craters on the Moon. In chapter 4, we show that South Ray crater at the Apollo 16 landing site has a faint cold spot. Its temperature anomaly and $\sim$2 Ma age are consistent with the fading rate of other large cold spots. Additionally, we show that the mean depth of astronaut footprints is greater at the Apollo 16 landing site than the other Apollo sites. This suggests that cold spots are caused by a decompaction of the upper regolith, consistent with estimates derived from thermal modeling. In chapter 5, we present the thermophysical properties of a global survey of cold spots and several new cold spots formed during the LRO mission lifetime. We show that the temperature anomaly of new cold spots scales with crater diameter, forming an upper envelope to the properties of pre-existing cold spots. This indicates a greater depth of regolith modification by larger cold spots. Using thermal modeling, we present bounds on the depth of regolith modification for new cold spots and estimate how this scales with crater size.

The dissertation of Tyler Michael Powell is approved.

Seulgi Moon

Mackenzie Day

David Jewitt

David A. Paige, Committee Chair

University of California, Los Angeles

2023

Đêm khuya ra đứng giữa trời,

Giơ tay ngoắc nguyệt,

nguyệt dời phương nao.

TABLE OF CONTENTS

1 Introduction **1**

2 The role of secondary craters on Martian crater chronology **8**

2.1 Introduction 9

2.2 Review of crater size-frequency distributions 10

2.3 Review of the debate over the effect of secondary craters 11

2.4 Constraining the flux of small primary craters 16

2.5 Production of secondaries by Martian primaries 19

2.5.1 New measurements of secondaries around large Martian primaries . . 22

2.6 Model of the global secondary SFD 28

2.7 Model of the spatial distribution of secondaries 35

2.8 Conclusions 39

3 High-resolution nighttime temperature and rock abundance mapping of the Moon using the Diviner Lunar Radiometer Experiment with a model for topographic removal **42**

3.1 Introduction 43

3.2 Data and methods 44

3.3 Diviner data set 44

3.3.1 Correction of angular pointing offsets 45

3.3.2 Effective field-of-view modeling 48

3.3.3 Slope-adjusted midnight brightness temperature 52

3.3.4 Bolometric temperature, regolith temperature, and rock abundance . 54

3.4 Thermal model for topography removal 56
3.4.1 Direct solar illumination 57
3.4.2 Indirect scattered and emitted radiation 58
3.4.3 Selection of albedo and emissivity for land scattering and emission . . 62
3.4.4 Topographic subtraction 65
3.5 Results and discussion 68
3.5.1 Global maps 68
3.5.2 Examples of map improvements 72
3.5.3 Validating rock abundance with manual boulder counts 74
3.6 Conclusions 81

4 Discovery of a lunar cold spot at Apollo 16's South Ray crater 84
4.1 Introduction 85
4.2 Data and methods 86
4.2.1 Diviner data and thermal model 86
4.2.2 Relative density from astronaut footprints 87
4.3 Results 88
4.3.1 Cold spot thermophysical properties 88
4.3.2 Correlation with other cold spots 91
4.3.3 In-situ regolith properties 94
4.4 Discussion 99
4.5 Conclusions 102

5 Thermophysical characteristics of lunar cold spots: a comparison between the contemporary and pre-existing populations 103

5.1 Introduction 104
5.2 Data and methods 105
5.2.1 Nighttime temperature of contemporary cold spots 105
5.2.2 Survey of pre-existing cold spots 107
5.2.3 Cold spot age estimates from superposed craters 108
5.3 Results and discussion 109
5.3.1 Thermophysical properties of contemporary cold spots 109
5.4 Cold spot retention 116
5.5 Conclusions 122

6 Conclusions and future prospects 124
6.1 Mapping of distant secondaries 124
6.2 Advances in thermal modeling 128
6.3 Cold spots and regolith evolution 132

LIST OF FIGURES

1.1 Lunar global nighttime temperatures showing cross-cutting ejecta rays 2

1.2 Nighttime temperature of the Tycho antipode deposit 4

1.3 Crater spatial distribution in the lunar mare 5

1.4 Apollo 17 ISR and Diviner bolometric temperature maps showing cold spots . . 6

2.1 Examples of secondary craters on Mars 12

2.2 Size-frequency distribution of new impact craters on Mars 16

2.3 Map of secondary craters around Lomonosov and Lyot crater 23

2.4 Size-frequency distribution of secondary craters around Martian primaries . . . 25

2.5 Radial drop-off of secondaries away from Lyot and Lomonosov crater 27

2.6 Modeled global secondary SFD for 2 Ma and 1 Ga 29

2.7 Analytical model for the global crossover diameter 32

2.8 Example of secondary accumulation accounting for spatial clustering 34

2.9 Cumulative histograms of modeled secondary density and crossover diameter . . 37

2.10 Modeled crossover diameter with time accounting for spatial clustering 38

3.1 Diviner angular offset correction 46

3.2 Spatial response of Diviner observations and of gridded spatial bins 49

3.3 Spatial bin effective resolution with latitude 50

3.4 Example of curve fitting to nighttime brightness temperature 53

3.5 Example of derived rock abundance and bolometric and regolith temperature . . 56

3.6 Bolometric and regolith temperature with latitude 58

3.7 Panorama of the Apollo 17 landing site with modeled temperatures 60

3.8 Emission phase function of the lunar surface at noon and midnight 63

3.9 Example of topographic removal at equatorial latitudes 66
3.10 Example of topographic removal at high latitudes 67
3.11 Global nighttime temperature and rock abundance maps 70
3.12 Correlation between new and old temperature and rock abundance maps 71
3.13 Slope-adjusted midnight temperature at Taurus-Littrow valley 73
3.14 Slope-adjusted midnight temperature at Tsiolkovskiy crater 75
3.15 Slope-adjusted midnight temperature for a cold spot 76
3.16 Boulder counts in the Apollo 17 landing site region 78
3.17 SFD of counted boulders in the Apollo 17 landing site region 79
3.18 Comparison between Diviner rock abundance and manual rock counts 80

4.1 Nighttime temperatures for South Ray and Bandfield cold spot 89
4.2 Fading behavior of large cold spots 93
4.3 Footprint derived relative densities for the Apollo sites 97
4.4 High-reflectance streaks associated with cold spots 100
4.5 Drop-off of small rocks with distance from South Ray crater 101

5.1 Example of a newly-formed crater in LROC imagery 105
5.2 Map of the global cold spot catalog 108
5.3 Examples of pre- and post- impact midnight temperature for new cold spots . . 110
5.4 Peak temperature anomaly and thermophysical properties versus crater diameter 112
5.5 Nighttime cooling curve and model fits for a new cold spot 113
5.6 Global size-frequency distribution of the cold spot population 117
5.7 Size-frequency distribution of contemporary lunar impacts 120
5.8 Cold spot fading based on global retention 121

6.1 Secondary fields around several lunar primaries 125
6.2 Secondary crater counts far from Copernicus crater 127
6.3 Example of global diurnal thermal model 129
6.4 3D thermal conduction model for small lunar PSRs 130
6.5 3D thermal conduction model for two locations on Mars 131
6.6 A hypothetical model for the mixing of regolith by cold spots 133

LIST OF TABLES

4.1 Summary of large cold spot properties 92

4.2 Summary of relative densities derived from astronaut footprints 96

5.1 Summary of contemporary cold spot properties 106

5.2 Summary of moderately-sized cold spot craters with derived ages 109

ACKNOWLEDGMENTS

This thesis would not have been possible without the support of many people.

Most importantly, I thank my Advisor, David Paige, for whom I have great admiration and respect. Dave allowed me to pursue my scientific interests freely while providing advice, guidance, and perspective at every turn. I owe my growth as a scientist mostly to this invaluable support.

In addition, I am fortunate to have had great collaborators and mentors throughout my time at UCLA and prior. There are too many to name them all, but here are a few. Ica Manas-Zloczower and Gholamreza Pircheraghi provided my first introduction to science, and patiently taught me the critical thinking necessary for research. Benjamin Greenhagen introduced me to the field of lunar and planetary science, encouraged me to pursue graduate school, and has continued to be a valuable mentor. Lior Rubanenko has been a great role model and showed me how to constantly be thinking of new, exciting ideas. Jean-Pierre Williams has generously shared his time and varied expertise with me across countless conversations. I thank my doctoral committee, David Jewitt, Mackenzie Day, and Seulgi Moon, for their challenging questions and supportive conversations in preparation of this thesis. My Paige-group office mates and the entire Diviner team have been willing to help and collaborate at any time, and all deserve much appreciation. I have learned a great deal about being a scientist from everyone listed and many others.

To the EPSS graduate students, thank you for making my time at in UCLA one that I will remember fondly. A special thank you to Ariel Graykowski, Akash Gupta, Yufan Xu, and Han Bao. With them, Los Angeles was truly a paradise.

And lastly, thank you to my family, who have always encouraged me to pursue my interests and passions, and have provided unending support throughout.

VITA

Education

2019-2023 Ph.D. Candidate (Geophysics & Space Physics), University of California, Los Angeles.

2019 M.S. (Geophysics & Space Physics), University of California, Los Angeles.

2017 B.S. (Chemical Engineering), Case Western Reserve University.

Research Experience

2017–2023 Graduate Student Researcher, Department of Earth, Planetary, and Space Sciences, University of California, Los Angeles. Advisor: David A. Paige.

2016–2017 APL NASA Intern and Temp-on-Call, John's Hopkins University Applied Physics Laboratory. Advisor: Benjamin T. Greenhagen.

2012–2016 Undergraduate Research Assistant, Department of Macromolecular Science and Engineering, Case Western Reserve University. Advisor: Ica Manas-Zloczower.

Mission Experience

2016–2023 NASA Lunar Reconnaissance Orbiter (LRO), Diviner Lunar Radiometer Experiment (DLRE) Science Team.

Teaching Experience

2019 Earth's Energy: Diminishing Fossil Resources and Prospects for a Sustainable Future (EPSS 101).

PUBLICATIONS

Venkatraman, J., Horvath, T., **Powell, T.M.**, and Paige, D.A. (2023). Statistical estimates of rock-free lunar regolith thickness from Diviner. *Planetary and Space Sciences*, 105662.

Graykowski, A., Lambert, R.A., ... **Powell, T.M.**, ... and Transom, I.M. (2023). Light curves and colors of the ejecta from Dimorphos after the DART impact. *Nature*, 616(7957).

Powell, T.M., Horvath, T., Lopez-Robles, V., Williams, J.-P., Hayne, P.O., Gallinger, C.L., Greenhagen, B.T., McDougall, D.S., and Paige, D.A. (2023). High-resolution nighttime temperature and rock abundance mapping of the moon using the Diviner Lunar Radiometer Experiment with a model for topographic removal. *J. of Geophysical Research: Planets*, 128.

Williams, J. P., Greenhagen, B. T., ... **Powell, T.M.**, ... and Sullivan, M. T. (2022). Temperatures of the Lacus Mortis region of the moon. *Earth and Space Science*, 9(2).

Powell, T. M., Rubanenko, L., Williams, J. P., and Paige, D. A. (2021). The role of secondary craters on Martian crater chronology. In *Mars Geological Enigmas* (pp. 123-145). Elsevier.

Rubanenko, L., **Powell, T.M.**, Williams, J.-P., Daubar, I., Edgett, K.S., and Paige, D.A. (2021). Challenges in crater chronology on Mars as reflected in Jezero crater. In *Mars Geological Enigmas* (pp. 97-122). Elsevier.

Williams, J.-P. , Bandfield, J.L., Paige, D.A., **Powell, T.M.**, ... and Costello, E.S. (2018). Lunar cold spots and crater production on the moon. *J. of Geophysical Research: Planets*, 123(9), 2380-2392.

CHAPTER 1

Introduction

Impact craters are the most widespread geologic feature in the solar system. They are the dominant landform on many planetary bodies, including the Moon, Mercury, the southern highlands of Mars, and most small satellites and asteroids. Some planets, like the Earth, have comparatively few craters. This is a rare condition indicative of recently active surface processes capable of erasing craters, like plate tectonics on the Earth or volcanism on Venus and Io. Although the evidence of cratering has been obscured, these planets, too, have experienced numerous impacts throughout their histories.

Impact craters are influential at all spatial scales. Giant impacts have been invoked as an explanation for many anomalous features throughout the solar system, including the tilted rotational axis of Uranus (Harris and Ward, 1982; Benz et al., 1989; Rogoszinski and Hamilton, 2021), the creation of Earth's Moon (Canup and Asphaug, 2001; Canup, 2004; Canup et al., 2013), and the formation of the northern lowlands of Mars (Wilhelms and Squyres, 1984; Frey and Schultz, 1988; Nimmo et al., 2008). At large scales, the dramatic pockmarked appearance of many planetary surfaces can be explained by the accumulation of craters over billions of years. Overlapping ejecta deposits of large craters and basins constitute much of the stratigraphy observed during the Apollo missions (Howard et al., 1974; Oberbeck, 1975). Over time, smaller impacts are responsible for the erosion of surface features by removing and redistributing material, resulting in the degradation of steep slopes and sharp lateral contrasts (Fassett and Thomson, 2014; Fassett et al., 2022). At the smallest scales, impacts break rock into fine grained regolith particles, and small impacts continue to evolve the regolith over time though mixing (Gault et al., 1974) and by welding regolith

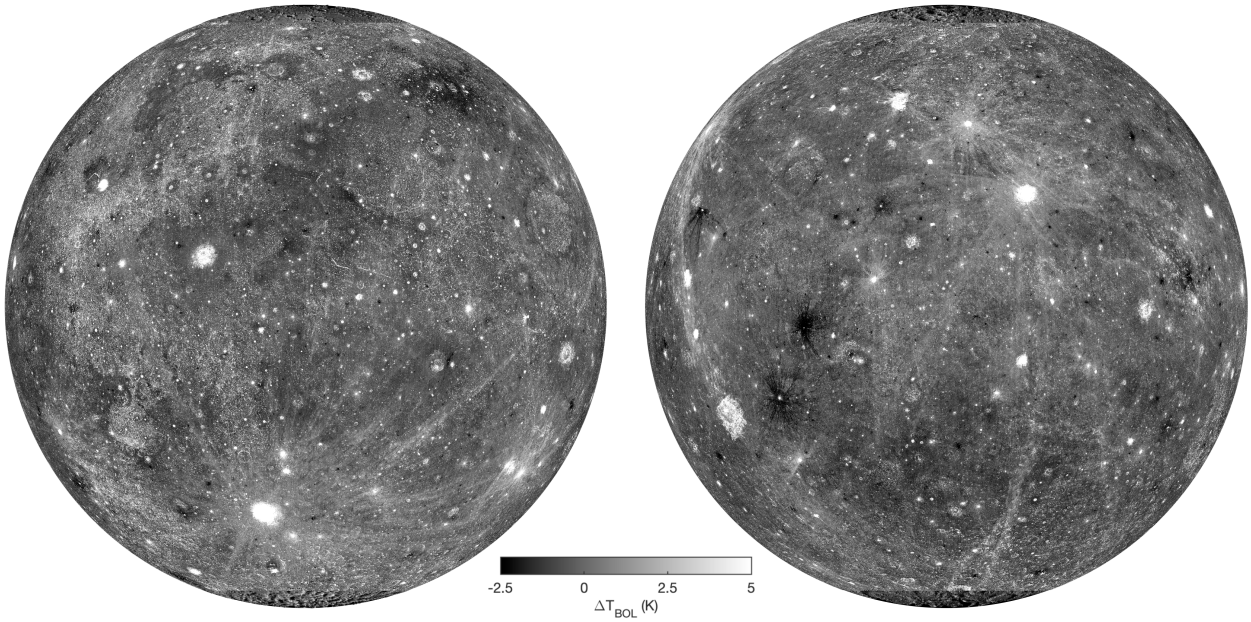

Figure 1.1: Lunar global nighttime bolometric temperature anomaly for the nearside (left) and farside (right) showing cross-cutting ejecta rays (Powell et al., 2023).

grains into breccias or glassy agglutinates (Duke et al., 1970; McKay et al., 1971).

Among the most enigmatic characteristics of craters are their rays: radial streaks formed when material ejected from the crater re-impacts the surface at high velocity (Oberbeck, 1971b; Hawke et al., 2004). Most of the material excavated during crater formation is redistributed close to the crater in its continuous ejecta blanket: ∼90% within ∼5 crater radii (Housen and Holsapple, 2011; Melosh, 1989). The remaining material, termed distal ejecta, is launched to greater distances. A quick inspection of the Moon shows that individual crater rays can extend to great distances, sometimes large fractions of the way around the Moon, and much of the lunar surface is crosscut by extensive ray systems (figure 1.1). Distal ejecta, while accounting for a minority of the total ejected mass of a crater, plays a important role in the evolution of planetary surfaces.

Crater ejecta is responsible for the lateral mixing of planetary surfaces by redistributing material along rays (Arvidson et al., 1975; Petro and Pieters, 2006, 2008). The samples collected at the each of Apollo landing sites contained regolith grains and rocks with petrologies

that indicate diverse provenances of origin. For example, highlands material makes up ∼20% of regolith grains at the Apollo 11 Tranquility Base despite it being ∼50 km from the nearest highlands geologic unit (Wood et al., 1970; Wood, 1970). This arises from a combination of lateral mixing by ejecta (Li and Mustard, 2005) and vertical mixing by craters which excavate highlands material from below the overlying mare basalt flows (Simon et al., 1983). Lunar science has benefited greatly from this lateral mixing, as it enabled a diverse sampling of lunar composition from only a few locations visited by the Apollo missions.

Our understanding of impact crater formation and ejecta mechanics is largely derived from terrestrial explosion craters, laboratory experiments, and planetary remote sensing (Braslau, 1970; Oberbeck, 1971a; Melosh, 1989; Housen and Holsapple, 2011). These models reproduce the near-field distribution of ejecta fairly successfully. However, the effects of high-velocity distal ejecta, though known to be significant, are still poorly understood. This is in part because the amount of distal ejecta drops-off with distance from the crater, and the small-scale but extensive features that they create require comparably high resolution imagery to be observed and are often eroded on shorter timescales than the crater itself. Recent years have seen dramatic improvements in the quality and volume of planetary data sets, and new insights suggest that distal ejecta plays a larger role in surface modification than was previously thought.

The light lunar plains are a smooth, flat, mare-like regions with composition and albedo similar to the highlands that cover ∼9.5% of the lunar surface. Global mapping of these features shows that they mostly fall along rays emanating from Orientale basin (∼950 km diameter), evidence that the ejecta of large impact basins create substantial landforms on a global scale which are able to persist for billions of years (Meyer et al., 2016). Smaller craters are also capable of global modification. Nighttime temperature mapping of the Moon reveals an anomalously rocky region located at the antipode of Tycho crater, an ∼85 km crater with prominent rays (figure 1.2). Ballistic modeling of Tycho ejecta and geologic evidence suggests that this feature likely formed from a focusing of high-velocity ejecta at the antipode, forming rocky impact melt deposits (Bandfield et al., 2017; Curren et al., 2018).

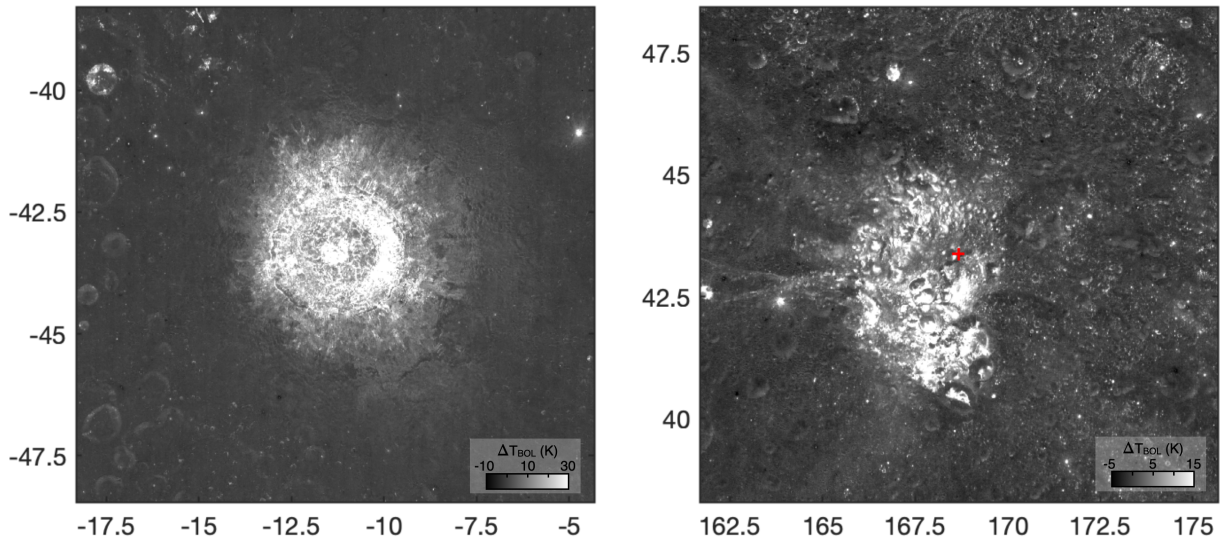

Figure 1.2: Midnight bolometric temperature anomaly (Powell et al., 2023) for a) Tycho crater and b) a rocky deposit at Tycho crater's antipode. The red marker indicates the location of the antipode.

Repeated imagery of the Moon (Speyerer et al., 2016) and Mars (Malin et al., 2006; Daubar et al., 2013) over the last decade has led to the identification of several newly-formed craters. Their unaltered ejecta show reflectance changes extending to great distances, 100s of crater radii in some cases. Lunar repeat imagery also shows newly-formed 'splotches' which don't have identifiable impact craters (Speyerer et al., 2016). Some of these may be caused by unresolved craters, but clustering in splotch timing suggests that many are formed by distal ejecta from far-off, unidentified primaries.

In this thesis, we use new data sets to investigate two classes of features associated with distal ejecta: secondary impact craters and lunar cold spots. Primary craters are formed when asteroidal or cometary material collides with a planetary surface at hypervelocity. Some of the material fragments ejected from the crater are energetic enough to form craters of their own, termed secondary craters, upon re-impacting the surface. Primary craters are often surrounded by a swarm of smaller secondary craters. Global imaging of the Moon and Mars with near complete spatial coverage has enabled the cataloging of all craters larger

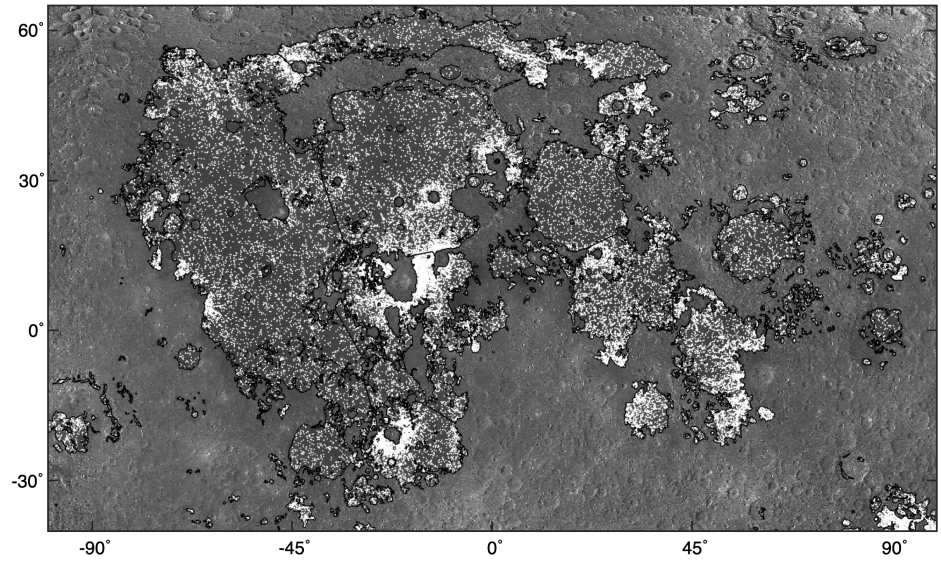

Figure 1.3: Spatial distribution of craters >1 km in the lunar mare from the Robbins (2019) crater database. Secondaries are often concentrated around large primaries.

than 1 km on both planetary bodies (Robbins and Hynek, 2012; Robbins, 2019). These products reveal regions with elevated crater spatial density associated with the far-reaching secondary fields of large primary craters (figure 1.3).

The significance of secondaries for crater counting and the mixing of the regolith has been a topic of significant debate since the 1960s (Shoemaker, 1965). Some have argued that the majority of secondaries can be identified by their morphology and clustering, and therefore secondaries have a minimal influence on derived surface ages if obvious secondaries are carefully excluded from crater counts (König, 1977; Neukum et al., 2001; Hartmann and Daubar, 2017). Others have noted that secondary craters sufficiently far from their parent primary look nearly indistinguishable from primary craters of the same size and are often not clearly clustered (Shoemaker, 1965; Soderblom et al., 1974; McEwen and Bierhaus, 2006). Furthermore, because the power-law slope of the secondary crater SFD is typically steeper than that of primary craters, secondaries should become more abundant than primaries below some size threshold (Shoemaker, 1965; Soderblom et al., 1974; Werner et al., 2009) and may be the dominant driver of impact gardening (Costello et al., 2018, 2021). To reconcile these

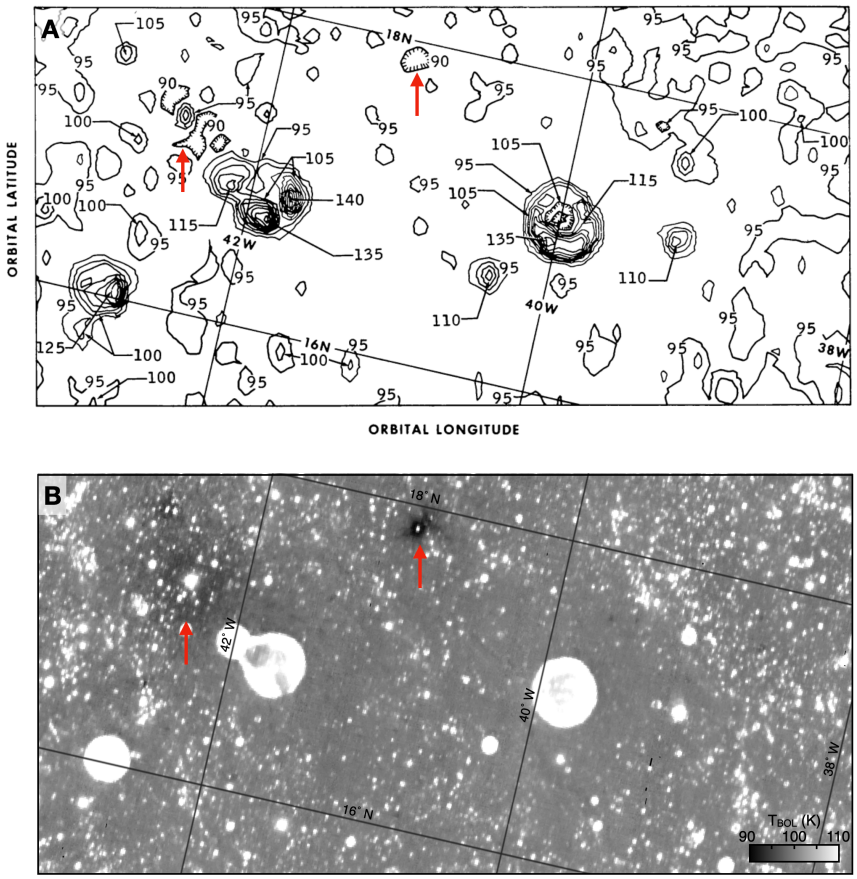

Figure 1.4: A) Apollo 17 Infrared scanning radiometer (ISR) nighttime temperature map containing 2 cold spots (Mendell and Low, 1975) compared with B) Diviner bolometric midnight temperature (Powell et al., 2023). Note that features in the ISR map are offset ∼1° west from the standard LRO reference frame (LRO Project, 2008).

viewpoints, in chapter 2 (Powell et al., 2021) we: 1) investigate the size-frequency and spatial distribution of secondaries associated with several large Martian primaries; and 2) develop a model for global secondary accumulation, accounting for the spatial clustering of secondaries around their parent primary.

Nighttime temperature mapping of the Moon by the Diviner Lunar Radiometer Experiment on the Lunar Reconnaissance Orbiter (LRO) (Paige et al., 2010a) has revealed a new class of thermophysical anomaly called "cold spots" around small (<2 km) lunar craters. These are ray-like low temperature regions which indicate a decompaction of the upper cen-

timeters of regolith to tremendous distances: hundreds of crater radii in some cases (Bandfield et al., 2014). Some examples of unusually cold regions were originally noted in data from the Infrared Scanning Radiometer on-board the Apollo 17 Command-Service Model (Mendell and Low, 1974, 1975), however there was insufficient high-resolution data at the time to tie these features to impact craters or to distinguish the ray-like structure of cold spots (figure 1.4). Cold spots are among the youngest known population of impact craters with a global size-frequency distribution (SFD) consistent with a retention age of ∼150 ka, with some large cold spots reaching ages of ∼1 Ma (Williams et al., 2018a). Cold spots represent a previously unknown but ubiquitous process which may significantly contribute to the evolution of the upper regolith. However, the magnitude and mechanism of modification is still poorly understood.

In this thesis, we characterize the thermophysical properties and fading behavior of lunar cold spots. This is broken into 3 chapters. In chapter 3 (Powell et al., 2023), we produce updated nighttime temperature maps of the Moon and develop a thermal model that removes the effects of topography. In chapter 4, we show that our updated temperature maps reveal a faint cold spot around South Ray crater, a ∼700 m diameter crater at the Apollo 16 landing site. We use Diviner nighttime temperatures and Apollo 16 in-situ measurements to investigate the thermophysical properties of South Ray crater's cold spot. In chapter 5, we show that several new craters formed within the last ∼13 years have cold spots. We compare the properties of these new cold spots with a population of pre-existing cold spots to understand their formation and fading behavior.

Chapter 6 serves as a conclusion. We discuss the broad implications of our results and propose several future investigations which expand on the work presented in this thesis.

CHAPTER 2

The role of secondary craters on Martian crater chronology

This chapter was published in: Powell, T. M., Rubanenko, L., Williams, J. P., & Paige, D. A. (2021). The role of secondary craters on Martian crater chronology. In *Mars Geological Enigmas* (pp. 123-145). Elsevier.

Abstract

The influence of secondary craters on the accuracy of crater chronology has been heavily debated. We review the production of secondaries on Mars and their cumulative effect on the global crater size-frequency distribution (SFD). We characterize the SFD of secondaries produced by four large primaries (∼50–220 km) and develop a model for secondary accumulation with time, accounting for spatial clustering. The number of km-scale secondaries produced globally may exceed primaries by an order of magnitude on Ga timescales. However, most secondaries are clustered around their parent primary, and regions far from large primaries have lower concentrations of secondaries. We estimate that the crossover diameter between primaries and secondaries on a median surface exceeds 1 km after ∼1–2 Ga, though subsequent crater erasure has significantly influenced the number of secondaries visible today. Because of the high spatial variability of secondaries, care should be taken when using small craters for crater counts.

2.1 Introduction

Impact craters dominate the landscapes of many planetary bodies. On Mars, a variety of geologic processes active throughout its past have erased pre-existing craters, resulting in some regions with very few craters, and other regions that have retained a high spatial density of craters from billions of years of bombardment. Early studies recognized that the relative abundance of impact craters on a surface could be used as an indicator of its age (Baldwin, 1949; Kreiter, 1960; Öpik, 1960; Shoemaker et al., 1963). Lunar samples obtained from the Apollo missions provided radiometric and cosmic ray exposure ages for several regions of the Moon, and crater counts in these regions were used to calibrate models of the absolute cratering rate (Arvidson et al., 1975; Neukum, 1983; Hartmann and Neukum, 2001; Neukum et al., 2001; Stöffler and Ryder, 2001; Robbins, 2014). The field of "crater chronology" has since become one of the most fundamental tools in planetary science and is the principal method of estimating surface age throughout the solar system. An understanding of crater chronology is critical to interpreting the timing of major events in Mars' past.

Primary impact craters form when asteroidal or cometary material collides with the surface at hypervelocity, ∼10 km/s on average for Mars (Ivanov, 2001). This results in the formation of a roughly circular depression Melosh (1989). Some of the ejected target material fragments are energetic enough to form craters of their own upon re-impacting the surface; these are termed secondary craters or "secondaries." Primary craters are often surrounded by a swarm of smaller secondary craters; single primary impacts have been shown to produce 10^6–10^9 secondary craters, which form nearly instantaneously in geologic time (Bierhaus et al., 2001; McEwen et al., 2005; Dundas and McEwen, 2007; Preblich et al., 2007; Williams, 2018). This introduces a complication for crater chronology, which relies on the predictable accumulation of craters with time following a knowable size distribution and rate. The effect of secondary craters on the ages derived from crater counting has been heavily debated since the 1960s. In the last few decades, several high-resolution and high-quality imaging datasets with good global coverage have become available for Mars which

allow us to better constrain the production of primary and secondary craters and assess the importance of secondaries for crater chronology there. In this work, we (1) review the history of the secondary crater literature, (2) use a global catalog of Martian craters to constrain the number of secondaries produced by several large primary craters (∼50–220 km), and (3) present a new model for the global accumulation of secondary craters with time, including the effect of spatial clustering of secondaries around large primaries.

2.2 Review of crater size-frequency distributions

The size-frequency distribution (SFD) of craters can be approximated as a power law, often expressed using the cumulative SFD (Crater Analysis Techniques Working Group, 1979):

$$N = CD^{-b} \tag{2.1}$$

where N is the number of craters larger than diameter D, C is a coefficient, and b is a power-law index that controls the ratio of large craters to small craters. This appears as a straight line on a plot of log D versus log N with a slope of $-b$. The cumulative representation is commonly used due to its simplicity; a list of crater diameters can be sorted in descending order and plotted against their rank, where the largest diameter occurs at $N = 1$. The cumulative number of craters is often divided by the count area, A, to produce a spatial density. In this chapter, we will denote absolute crater number using capital letters and crater spatial density using lowercase letters: $n = cD^{-b}$ where $c = C/A$.

The differential SFD is the derivative of the cumulative SFD, or the number of craters within some diameter range divided by the bin width (Crater Analysis Techniques Working Group, 1979):

$$\frac{dN}{dD} = bCD^{-(b+1)} \tag{2.2}$$

While less intuitive than the cumulative SFD, the differential SFD corresponds to the number of craters within some size range and is not affected by the distribution of all larger craters.

In practice, crater populations do not strictly follow a single power law across all diame-

ters. However, this approximation is often appropriate for describing craters within limited size ranges, and the concept of power-law slope is valuable for discussing variations in more complicated crater SFDs. Production functions (PFs) describe the SFD of craters produced on a planetary surface during some time. The commonly used Neukum PF (Neukum et al., 2001) and Hartmann PF (Hartmann, 2005; Hartmann and Daubar, 2017) were developed using the observed SFD of lunar craters. The historical cratering rate was determined by correlating the absolute ages of lunar samples to crater counts on related geologic units (Arvidson et al., 1975; Neukum, 1983; Hartmann and Neukum, 2001; Neukum et al., 2001; Stöffler and Ryder, 2001; Robbins, 2014). This rate has been relatively constant during the last 3 Ga, with a much higher flux prior to this. In the absence of datable surface samples for Mars, the Martian Neukum/Ivanov and Hartman PFs have been scaled from their lunar counterparts by accounting for differences in the mean impact velocity, gravity, and proximity to the asteroid belt between the two bodies (Ivanov, 2001; Hartmann, 2005; Hartmann and Daubar, 2017). The Martian Hartmann PF also includes a correction for the loss of small craters due to atmospheric effects (Hartmann, 2005). PFs can also be developed using the SFD of the impactor population instead of crater counts. For example, the Williams PF uses the observed flux of bolides entering the Earth's atmosphere (Brown et al., 2002) and crater scaling relationships (Holsapple, 1993) to model the primary PF for the Moon and Mars (Williams et al., 2014). Rubanenko et al. (2021) discuss crater SFDs and the application of crater chronology in more detail.

2.3 Review of the debate over the effect of secondary craters

The first studies to discuss the size distribution of impact craters were performed using the smallest craters on the Moon observable through Earth-based telescopes (Young, 1940). Hartmann (1964) measured the distribution of lunar craters larger than ∼8 km in diameter and reported a slope of approximately -2 (note unless otherwise specified, slopes given in this chapter are cumulative). In 1964 the Ranger VII mission to the Moon imaged Mare Cognitum

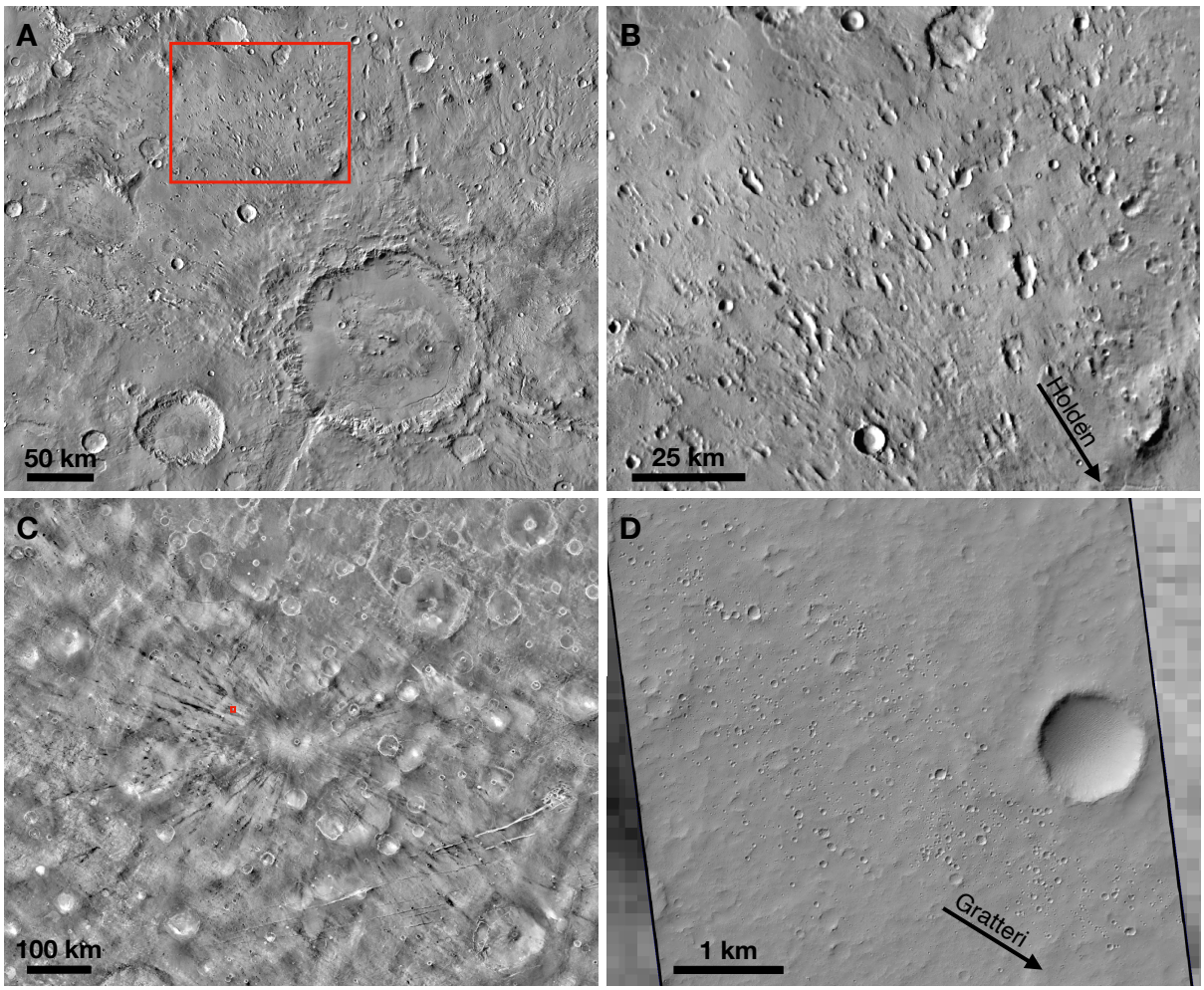

Figure 2.1: Two examples of primary craters with systems of secondary craters. (A) Holden crater (153.8 km, -26.4°N, -34.0°E) and (B) a field of nearby secondaries in the THEMIS daytime IR Global Mosaic (Edwards et al., 2011). (C) Gratteri crater (6.9 km, -17.7°S, -160.1°E) showing distinctive low thermal inertia rays extending several hundred kilometers in the THEMIS nighttime IR Global Mosaic (Edwards et al., 2011). (D) A High Resolution Imaging Science Experiment (HiRISE) image of a cluster of secondaries ∼120 km or ∼34 crater radii from Gratteri crater (HiRISE EPS_026579_1630). Secondaries close to their primary tend to have distinctive irregular morphologies, while distant secondaries are more circular and can be difficult to distinguish from primaries.

at high resolution, providing the first observations of features smaller than ∼100 m on the lunar surface. This expanded the lunar crater SFD to significantly smaller sizes. Shoemaker (1965) found that the SFD of craters smaller than ∼1 km has a slope of approximately -3.5, significantly steeper than the slope observed for larger craters. This is sometimes referred to as the "steep branch" of the SFD, relative to the "shallow branch" for craters larger than ∼1 km. Clusters of secondary craters associated with the ray systems of nearby large primary craters were abundant in Mare Cognitum images. Shoemaker (1965) classified craters as primary or secondary based on their clustering and morphology. Secondaries found close to large primaries tend to be shallower in depth than primaries of the same size and have irregular shapes (Shoemaker, 1965). They often form in distinct clusters or chains, sometimes so closely packed that they create elongate composite craters (figure 2.1A and B). T his distinctive morphology is likely caused in part by the relatively low velocities and close proximity of impactors (Shoemaker, 1965; Melosh, 1989). Farther away from the primary, secondaries become less clustered and greater impact velocities result in more circular secondary craters (figure 2.1C and D). These distant secondaries, sometimes termed "field," "background," or "unrecognized" secondaries, can be more difficult to distinguish from primary craters.

Shoemaker (1965) states that the fraction of secondaries in Mare Cognitum becomes larger at smaller sizes: most craters larger than 1 km were classified as primary while the majority of craters between 300 m and 1 km were classified as secondary. Counts of secondaries around large lunar primaries (Shoemaker, 1965; Wilhelms et al., 1978) and terrestrial explosion craters (Roberts, 1964) revealed power-law slopes of roughly -4, similar to the steep slope observed for lunar craters smaller than ∼1 km. Shoemaker (1965) proposed a model of total crater accumulation where primary craters dominate at large sizes but secondary craters overtake them below some "crossover diameter," which varies by terrain age (discussed further later) and Shoemaker (1965) estimates is ∼200 m for the lunar maria. Shoemaker's argument has sometimes been interpreted to be that the "steep branch" observed in the SFD below 1 km is caused predominantly by secondary craters. However,

Shoemaker preferred a model for primary production that included a steepening at smaller sizes based on the size distribution of near-Earth objects (Brown, 1960), which is consistent with our current understanding of sub-km primary production in the inner solar system (Ivanov, 2006; Williams et al., 2014; Speyerer et al., 2016). Soderblom et al. (1974) adapted this model for Mars and proposed that most of the craters smaller than 1 km on Mars were of secondary origin.

While secondaries clearly contribute to observed crater populations, there has been disagreement on the effect that secondaries have on the validity of crater chronology. The Hartmann PF excludes obvious secondary craters but includes both primaries and some unknown fraction of background secondaries, making the assumption that the more randomly distributed background secondaries also record chronological information (Hartmann and Daubar, 2017). Some have argued that the majority of secondaries can be identified by their morphology or clustering, and therefore secondaries have a minimal influence on derived surface ages if obvious secondaries are carefully excluded from crater counts (König, 1977; Neukum et al., 1975, 2001). Because the largest craters on the surface contribute most of the secondary craters, the crossover diameter should progress to larger sizes for older terrains (Neukum, 1983; Neukum and Ivanov, 1994; Werner et al., 2009). This effect is illustrated well by the results of Wilhelms et al. (1978) who found that secondaries formed by lunar basins result in a crossover diameter in the highlands of ∼20 km, much larger than the 200 m value Shoemaker (1965) proposed for the younger Maria. Neukum and Ivanov (1994) found that when "obvious" secondaries were excluded from counts, the SFD maintained an increase in slope for craters smaller than ∼1 km for terrains of all ages and argued that this meant that the PF reflected predominantly primaries. The observation of a steep slope for 200–600 m diameter craters on Gaspra, which is expected to have very few secondaries because of its low escape velocity, provided additional evidence that the primary impactor population includes a steepening below ∼1 km (Chapman et al., 1996).

Others have noted that secondary craters sufficiently far from their parent primary look nearly indistinguishable from primary craters of the same size and are often not clearly

clustered (Shoemaker, 1965; Soderblom et al., 1974; McEwen and Bierhaus, 2006). This is exemplified by young Martian craters with well-preserved secondary-containing ray systems, which extend hundreds of crater radii in some cases (McEwen et al., 2005; Tornabene et al., 2006; Preblich et al., 2007; Quantin et al., 2016; Williams, 2018; Williams et al., 2018b), as revealed by their thermal signature observed by the Thermal Emission Imaging System (THEMIS) on the Mars Odyssey spacecraft (Christensen et al., 2004). In particular, a $\sim$10 km rayed crater on Mars, Zunil (7.7°N, 166.2°E), is estimated to have produced $\sim 10^8$ secondary craters larger than 10 m in diameter (McEwen et al., 2005; Preblich et al., 2007). This is comparable to the number of primary craters of the same size expected to have been produced during the last few Ma, the estimated age of Zunil. Almost all of these were formed at ranges greater than $\sim$16 crater radii and lack the distinctive morphological characteristics commonly used to identify secondary craters. This finding, as well as a similar study of secondary craters on Europa published around the same time (Bierhaus et al., 2005), led to renewed interest in the problems that secondaries could pose for chronology models. This led some researchers to suggest that the small crater population on Mars may be dominated by "field" or "background" secondaries of distant large primaries and that the PFs developed from crater counts excluding only obvious secondaries may not be representative of the primary crater population (McEwen and Bierhaus, 2006). Modeling work by Bierhaus et al. (2018) demonstrates that there is likely significant variation in the expression of secondary crater populations throughout the solar system, depending on effects like surface gravity, escape velocity, and typical impact velocity. For example, field secondaries may be especially important for the Moons of Saturn, where their relatively low surface gravities result in more globally distributed secondaries. Conversely, bodies with high surface gravity like the Moon and Mars show more clustered secondary fields. This results in a high regional variability in crater spatial density.

These stances have not yet been fully reconciled. Ultimately, the relative importance of secondaries can be determined if both (1) the production rate of primaries and (2) the distribution of secondaries produced by individual primaries are known. While conceptually

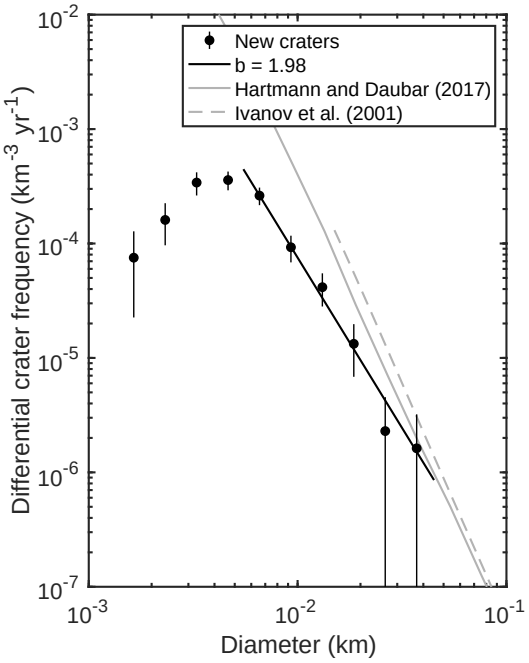

Figure 2.2: New primary craters observed by the High Resolution Imaging Science Experiment (Daubar et al., 2013, 2014; Hartmann and Daubar, 2017) in root-2 bins normalized to an annual flux. Note that in the figure in Williams (2018), data were plotted at bin edges rather than the geometric bin centers as is done here. The SFD of ∼15 m new craters identified on Mars is approximately three to five times lower than expected from the production functions. The best fit differential slope is -2.98 (or $b = 1.98$) for craters larger than 5.5 m. Modified from Williams (2018).

simple, obtaining definitive measurements for either of these has proved complicated, though modern datasets with high resolution and global coverage are providing valuable insights. We address both components in the following sections.

2.4 Constraining the flux of small primary craters

One of the largest debates in the study of secondary cratering is: Do commonly used PFs largely reflect primary crater production, or have they been significantly influenced by sec-

ondary craters and thus represent the accumulation of primaries plus some unknown fraction of secondaries? The identification of several small craters formed on Mars within the last few decades provides a unique opportunity to isolate the current primary cratering rate. Malin et al. (2006) identified 19 new craters using the Mars Orbiter Camera (Malin et al., 1992) on the Mars Global Surveyor spacecraft. New craters were identified by the appearance of dark spots in repeated imagery, which result from the removal of a surface layer of bright dust by the impact blast. Daubar et al. (2013, 2014) expanded this survey using observations from the Context Camera (CTX) (Malin et al., 2007) and High Resolution Imaging Science Experiment (HiRISE) (McEwen et al., 2007) The most recently published SFD includes 110 impacts with dates constrained by CTX before and after images (Daubar et al., 2014). Over half of the impact sites are clusters of craters instead of individual primary craters due to fragmentation of the impactor in the atmosphere. Effective crater diameters for the clusters were estimated by summing the volumes of craters within each cluster: $D_{eff} = (\sum_i D_i^3)^{1/3}$ (Malin et al., 2006; Daubar et al., 2013; Ivanov et al., 2014). The effective diameters of these impacts range from ∼1 to ∼40 m. These are expected to be primaries as they appear across extensive areas of Mars and have a range of formation dates. Additionally, creating secondaries of this size would require a primary crater at least a few 100 m in diameter (Schultz and Singer, 1980), which has not been observed.

Figure 2.2 shows the SFD of new Martian craters identified by Daubar et al. (2013, 2014). The number of new craters ∼15 m in diameter is three to five times lower than predicted by the Hartmann and Ivanov PFs. The SFD of new craters also has a shallower slope than either PF in this size range, resulting in better agreement with the PFs for the largest new craters observed. The cause for these discrepancies is currently unresolved, though several possible explanations have been proposed.

One option is that the counts used to derive the PFs include unrecognized field secondaries, resulting in an over-prediction of the number of decameter-sized craters. Hartmann et al. (2018) use the observation that ∼50% of new craters form clusters to estimate the secondary contribution for several regions of Mars. They propose that the total number of

primary craters in a region should be roughly double the number of clusters, and that any additional individual craters may be field secondaries. Using this approach, they estimate that ∼40–80% of craters ∼20–250 m in diameter may be field secondaries, with greater percentages at smaller sizes. The catalog of new craters likely oversamples crater clusters because their larger footprint is easier to detect from orbit than the equivalently sized individual primary (Daubar et al., 2019), so these results may be an upper bound. Williams et al. (2014) demonstrate that a PF developed using the current flux of terrestrial bolides agrees with the Hartmann PF. Because the Williams PF represents only primary impacts, this result indicates that the Hartmann PF should contain relatively few secondaries in the decameter size range. Additionally, the formation rate of new craters on the Moon agrees with the lunar Neukum PF, differing by only ∼33% (Speyerer et al., 2016). This suggests that secondary craters do not make a significant contribution to the lunar PFs, from which their Martian counterparts are derived.

The catalog of new Martian impacts is also known to be incomplete. Because new impacts are detected by the formation of dark spots, the catalog is biased toward the dustiest areas of Mars. This was addressed in Daubar et al. (2013) by considering only regions with a high dust cover index. However, Daubar et al. (2014) show that dark spots are not uniformly distributed even in dusty regions. Compensating for spatial variations in detection efficiency may increase the new crater SFD by a factor of ∼1.7 or more. This may also partially explain the shallow slope of the new crater SFD, as it is likely that small craters are more affected by the variations in the terrain properties that cause non-uniform dark spot detection (Daubar et al., 2015). Additionally, dark spots may fade due to Aeolian processes. A study of dark spot changes over time shows that the median blast zone has a lifetime of ∼8 Martian years, an order of magnitude longer than the average interval between CTX images for detected dark spots (Daubar et al., 2016). However, some small craters do show more rapid changes and some potentially may fade prior to detection.

Alternatively, ablation or deceleration of impactors in the atmosphere could result in smaller craters, especially if fragmentation occurs prior to impact. The Hartmann PF and

Williams PF account for the influence of the atmosphere on crater size (Popova et al., 2003), though it is possible that these models underpredict this effect (Ivanov et al., 2014). It is also possible the observed SFD is the result of real fluctuations in the impact rate. While current crater chronologies suggest that the cratering rate has been relatively constant over the last ∼3 Ga, it may vary on short timescales due to collisions or breakup events in the asteroid belt, but it is still under investigation at what crater diameters this effect would be noticeable (Bottke et al., 2007; Nesvorný et al., 2009; Vokrouhlický et al., 2017; Mazrouei et al., 2019; Terada et al., 2020; Kirchoff et al., 2021).

Considering the many assumptions involved with developing a crater chronology for Mars and the complicated processes that may influence new crater detection, the agreement of the new crater SFD with the Hartmann and Ivanov PFs is generally quite good. The observed discrepancy likely results from some combination of the previously discussed effects. However, regardless of the dominant cause, these results confirm that the "steep branch" of the Martian SFD observed for craters <1 km cannot solely be attributed to secondaries. An extrapolation of the "shallow branch" to these smaller sizes underpredicts the number of new craters by a factor of $\sim 10^2$, much greater than the observed discrepancy of 3–5.

2.5 Production of secondaries by Martian primaries

The total number and size distribution of secondaries produced by individual primaries has proven difficult to fully characterize observationally. The common approach is to consider only obvious secondaries using indicators like clustering or by their distinctive morphology, including location in rays. Shoemaker (1965) identified obvious secondary craters around Langrenus crater (130 km, -8.9°N, 60.9°E) on the Moon and found that the SFD approximately followed a power-law distribution with a slope of roughly -4. The largest secondary identified around Langrenus was ∼5% the size of the primary. This agreed fairly well with counts of secondaries around the Sedan nuclear explosion crater (390 m) on Earth which also showed a slope of -4, though the largest secondary was ∼8% the size of the primary

(Shoemaker, 1965). Schultz and Singer (1980) studied the secondary populations of a small sample of large craters on the Moon, Mercury, and Mars and found that few secondaries are formed larger than 5% the size of the primary, though examples of larger secondaries are not uncommon. Target properties also influence secondary production on Mars. Calahorra crater (34.2 km, 26.45°N, -38.65°E), which formed in Chryse Planitia, showed a similar ejecta structure and secondary distribution to craters on Mercury and the Moon (Schultz and Singer, 1980). However, Arandas crater (24.8 km, 42.41°N, -15.03°E) and Davies crater (48.1 km, 45.96°N, 0.09°E), which formed in the fractured plains region and have extensive flow lobes, showed very few secondaries larger than 2% of their diameter.

Robbins and Hynek (2011b) use a global database of all Martian craters larger than 1 km (Robbins and Hynek, 2012) to examine the secondary populations of 24 large Martian primaries ∼20 to ∼220 km in diameter. They classify craters in their nearby secondary field as primaries or secondaries using morphological indicators. The secondary SFDs have a wide range of power-law slopes between -3.3 and -8 over certain diameter ranges. The secondaries considered in this survey typically peak in number at 2.4 crater radii and extend to roughly 6 crater radii. Robbins and Hynek (2011a) studied the distant secondaries of Lyot crater (220 km, 50.8°N, 29.3°E) and identified ∼150 clusters of secondaries as far as 5200 km or ∼50 crater radii away. The number of distant craters identified is about an order of magnitude fewer than the number of secondaries proximal to Lyot crater, though this is an underestimate as only clusters of secondaries were included. However, this demonstrates that secondary contamination can occur even in regions that are far from large primaries. Robbins and Hynek (2014) catalog all Martian craters as primary or secondary and estimate that at least 19% of the craters >1 km globally are secondaries. This study presents a conservative underestimate, as many distant secondaries which lack clear morphological indicators were likely not identified.

Several other rayed craters in addition to Zunil were identified in THEMIS nighttime imagery (Tornabene et al., 2006). Quantin et al. (2016) performed crater counts on and between the rays of Gratteri crater (6.9 km, -17.7°N, -160.1°E). They estimate that half of

the secondaries of Gratteri crater are located within rays and clusters that occupy 2% of the area around Gratteri, and the other half are scattered between obvious rays. Corinto crater (13.8 km, 16.95°N, 141.72°E) is a rayed crater in Elysium Planitia. Williams et al. (2018b) and Williams (2018) performed counts of meter-to-decameter-sized craters in two regions overlapped by Corinto rays at distances of 520 and 660 km. The crater SFDs deviate from the Hartmann PF at small sizes in both locations, with steep power law slopes varying from -3.6 to -8.2 over limited size ranges. Regions not overlapped by obvious rays also show this increase in slope, though the total spatial density of craters in inter-ray regions is lower than inside rays. Williams (2018) estimates that Corinto crater may have produced over 10^9 meter-to-decameter-sized secondary craters.

Zunil and Gratteri craters have few secondaries within 10 crater radii with their largest secondaries ∼2% the size of the primaries. This contrasts notably with the densely packed fields of proportionately larger secondaries observed around 100 km-scale primaries (Schultz and Singer, 1980; Robbins and Hynek, 2011b). Preblich et al. (2007) note that few large blocks are found around Zunil and suggest that small fragments, which landed within a few crater radii, and consequently had lower velocities, may not have been energetic enough to form noticeable secondary craters. However, the reason for this difference remains an open question.

Vickery (1986, 1987) studied the secondary fields of several primaries on the Moon, Mercury, and Mars and found that the maximum secondary size decreases with distance from the primary. This was used to characterize the size–velocity relationship of ejecta fragments. The ejection velocity for each secondary was determined from their range to the primary. Crater scaling laws (Schmidt and Holsapple, 1982; Schmidt and Housen, 1987) were used to infer the size of the inciting ejecta fragment from the secondary crater size. The upper envelope of ejecta fragment size and ejection velocity was fit using a power law: where the velocity exponent β typically varied between ∼1.5 and 2.5 (Vickery, 1987). Singer et al. (2020), in a study of the secondary fields of several lunar craters, show that variation in β likely depends on the size of the primary crater. The maximum ejecta fragment size

falls off more rapidly with velocity for larger primary craters.

2.5.1 New measurements of secondaries around large Martian primaries

Robbins and Hynek (2011b) noted that the regions surrounding several large primaries show an enhancement in the total spatial density of craters a few kilometers in diameter and steep-sloped SFDs. This indicates that the effect of secondaries is noticeable in these regions even without classifying craters as primary or secondary. A less explored method for estimating secondary production is to compare the SFD of all craters between a region proximal to a large primary and a nearby reference region of similar age and geology. Subtracting the SFDs between these two regions results in a distribution of "excess" craters which we assume to be mostly secondaries. A major advantage of this approach is that it is agnostic to classification criteria like morphology or clustering. We use this approach and a catalog of Martian craters >1 km (Robbins and Hynek, 2012) to investigate four large primary craters, three of which were also studied in Robbins and Hynek (2011b). For each, we consider a region extending to ∼8 crater radii, beyond which the crater spatial density is indistinguishable from the background spatial density (Robbins and Hynek, 2011b). Reference regions were selected which occur on similar terrain and are likely to be of similar age. Lomonosov crater (120 km, 64.9°N, -9.2°E) is located in the relatively sparsely cratered Northern Plains, which causes the excess crater spatial density in its vicinity to be easily noticeable (figure 2.3A). Lyot crater (220 km, 50.5°N, 29.3°E) is also located in the Northern Plains; however, many of the secondaries to the south overlap a more heavily cratered landscape (figure 2.3B). To avoid this complication, we only consider the region north of Lyot crater and assume that the same number of secondaries was produced in the south. We also investigate an unnamed 77.6 km crater (-30.28°N, -160.18°E) and 50.8 km Kalpin crater (8.93°N, 141.28°E).

One limitation of this approach is that it is often difficult to identify large, uninterrupted regions with similar age and geology on Mars. As a result, many primary craters with prominent secondary fields are poor candidates for this method because their secondaries overlap more than one terrain type or overlap the secondary fields of other nearby primaries.

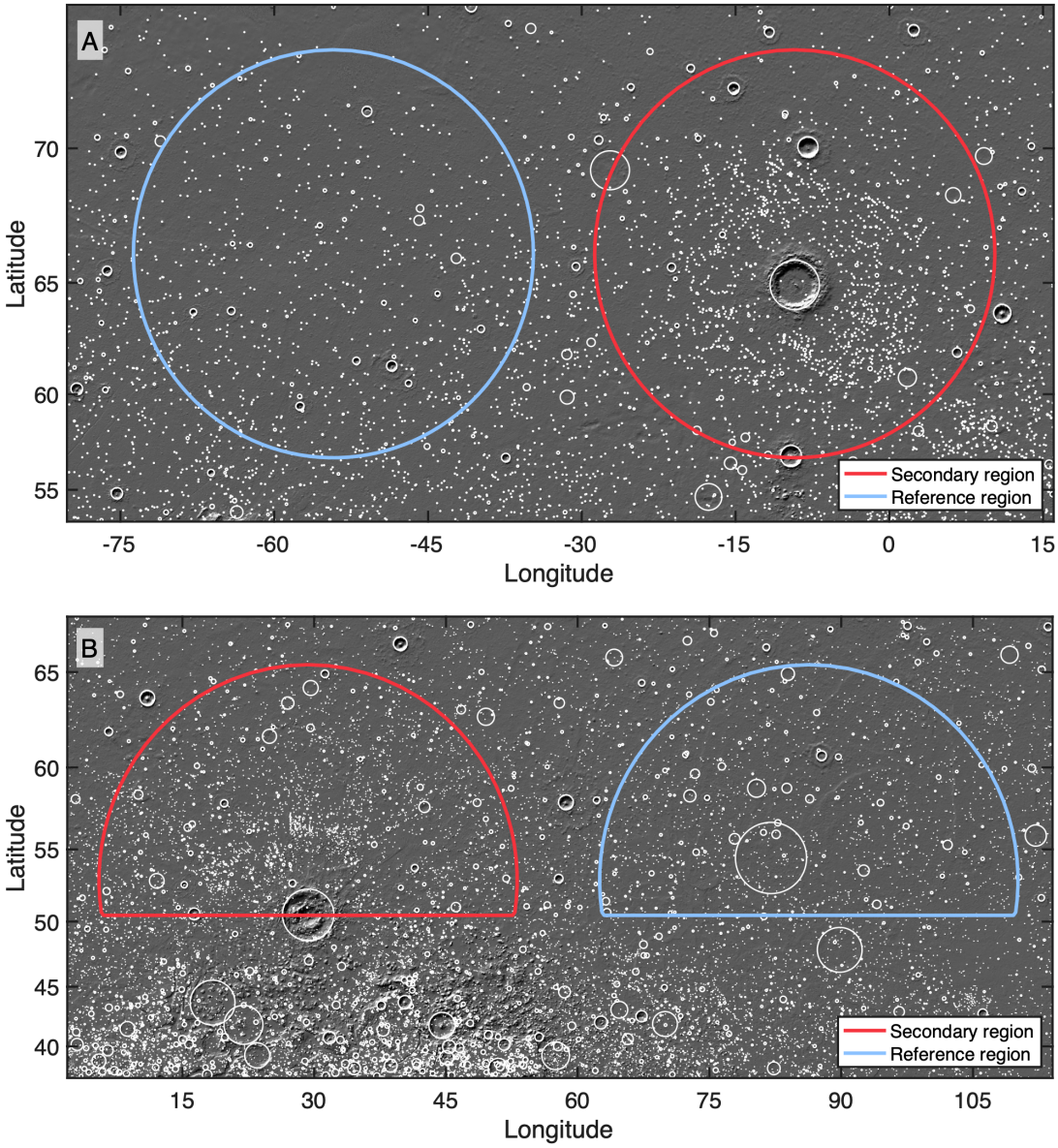

Figure 2.3: Craters >1 km in regions around (A) Lomonosov and (B) Lyot crater from the Robbins and Hynek (2012) crater catalog overlaid on the Mars Orbiter Laser Altimeter (MOLA) shaded relief map (Smith et al., 2001). The count region around each crater extends to 8 crater radii. For Lyot crater, we only consider the northern half of this region as a change in terrain type to the south causes an increase in crater density unrelated to secondaries.

Additionally, erosional processes that may erase craters, such as infill by regolith or ice deposition/sublimation, can be fairly localized. Crater erasure is further discussed in Rubanenko et al. (2021). We minimize these effects by focusing on craters found in expansive regions of similar terrain and with relatively uniform background crater densities like the Northern Plains, as these regions are likely to have experienced a similar history of primary cratering and crater erasure. However, it is important to note that local difference may still persist.

Figure 2.4 shows the differential crater SFD for each candidate site. The spatial densities of the secondary field regions generally agree with the reference regions for large craters (>10 km), which are expected to be mostly primaries. This indicates that the two regions have similar ages and experienced a comparable primary cratering history. The secondary field regions show a noticeable excess of small craters (1–10 km) relative to their reference regions. We assume that this is primarily the result of abundant secondaries. Crater erasure in the reference region may also play a role, though this is unlikely to be the dominant difference due to the choice of regions with similar geologic context. The distribution of excess craters, obtained by subtracting the SFDs between the two regions, is fit using a power law:

$$N_{s,i} = C_{s,i} D^{-b_s} = (f D_{p,i})^{b_s} D^{-b_s} \tag{2.3}$$

where b_s is the power-law slope and $C_{s,i}$ is the coefficient. We express $C_{s,i}$ in terms of the expected size of the largest secondary, which is some fraction, f, the size of the primary, $D_{p,i}$. Note that we do not directly measure the largest secondary. Rather, $f D_{p,i}$ corresponds to what the size of the largest secondary would be if the power law that fits the SFD at smaller sizes continues to $N_{s,i} = 1$.

The slope of the SFDs range from -3.7 to -4.3, consistent with previous studies (Shoemaker, 1965; Wilhelms et al., 1978; Robbins and Hynek, 2011b). However, we require an f of ∼7–12% to explain the number of excess craters. This is greater than the 5% value that has been used in studies estimating the global secondary SFD (Soderblom et al., 1974; Werner et al., 2009). While this difference may seem small, $N_{s,i}$ is a strong function of f. Using $f = 5\%$ and $b_s = 4$ under-predicts the number of inferred secondaries by about an

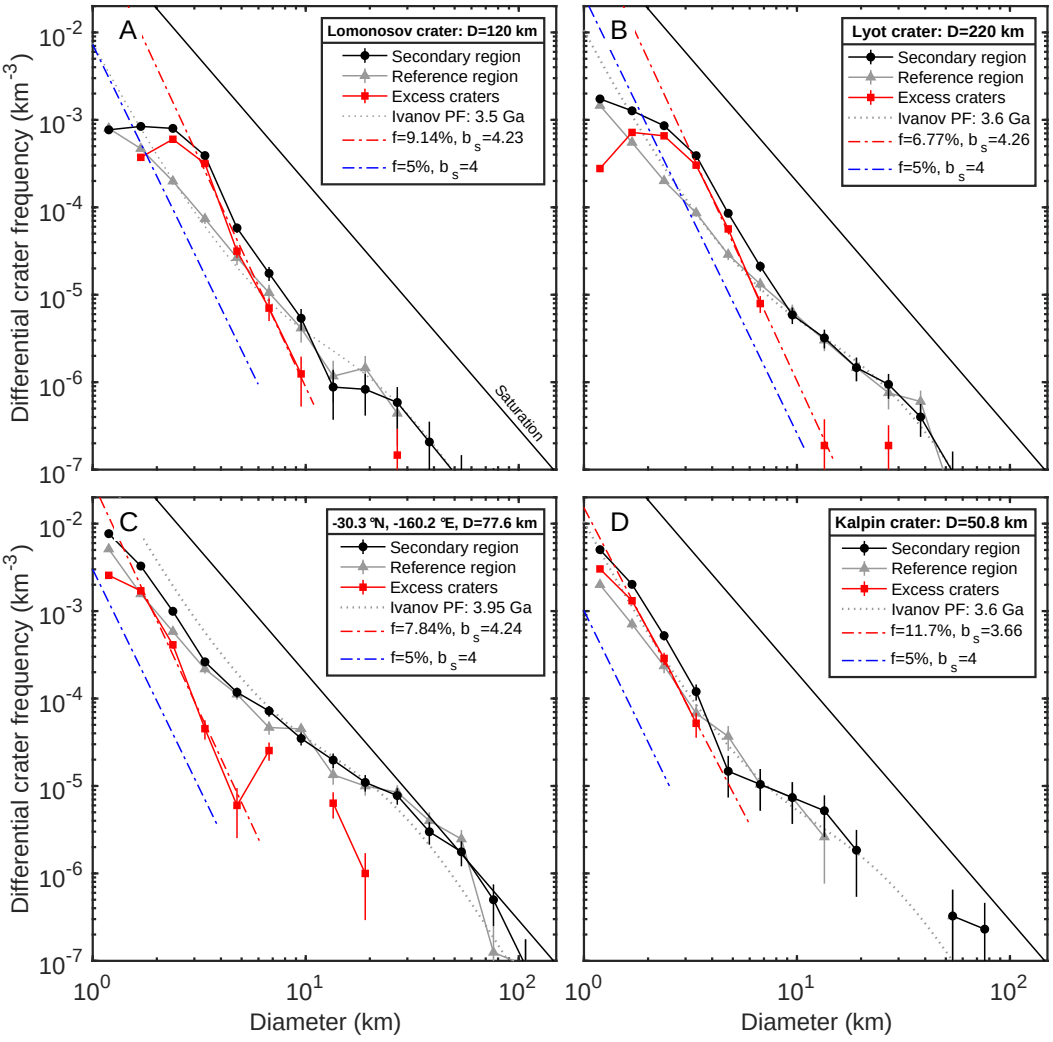

Figure 2.4: Differential SFDs of the regions around four Martian craters (A-D) with noticeable secondary fields compared to the SFDs of nearby reference regions. For Lyot crater, only the northern secondary field is considered (figure 2.3B). We fit the distribution of excess craters to a power law with slope $-b_s$ and a coefficient that is scaled to the size of the primary by f, the ratio of the expected diameter of the largest secondary to the primary diameter (equation 2.3). The dotted gray lines show Ivanov PF isochrons for reference (Ivanov, 2001) and the solid black lines indicate saturation equilibrium (Hartmann, 1984).

order of magnitude (figure 2.4). This highlights that using the size of the largest observed secondary to define the secondary SFD at smaller sizes may result in significant errors.

The distribution of inferred secondaries deviates from the power-law fit at small diameters. While the distribution of secondaries is expected to transition to a shallower slope at some diameter (McEwen et al., 2005; Melosh, 1989), we suggest that the roll-off observed in this case is likely due to the erasure of small craters by erosional processes such as crater infill by regolith or ice deposition/sublimation. This is demonstrated by the crater SFDs of the reference regions, which deviate from the PF at small sizes. It is likely that more craters, both primaries and secondaries, were produced in the 1 km size range than are currently represented. Secondaries may be especially susceptible to erasure because they are shallower than primaries of the same size. This roll-off may also be partially due to incompleteness of the Robbins and Hynek (2012) crater catalog in these regions of Mars. The THEMIS daytime IR mosaic (Christensen et al., 2004) that was used to produce the crater catalog had a global coverage of >99% at the time; however, there were some small regions that lacked coverage, particularly in the northern high latitudes (Robbins and Hynek, 2012).

Distant secondaries are also formed at greater ranges than the ∼8 crater radii that we consider here. Despite many studies of secondary populations, the total number of distant secondaries has proved difficult to characterize in large part because their spatial density rapidly becomes lower than the spatial density of background primaries. The radial drop-off of inferred secondaries close to the crater, where an excess crater spatial density can be measured, may help to inform the number of distant secondaries. We consider only craters larger than 2.5 km because of the potential erasure of smaller craters. Figure 2.5 shows the decrease in crater spatial density radially away from Lomonosov and Lyot craters. In both cases, almost no secondaries are formed within 2 crater radii. The secondary spatial density peaks between 2 and 4 crater radii and decreases rapidly beyond this. We characterize this drop-off by fitting a power law to the excess crater spatial density: $n \propto r^{-\alpha}$. For Lomonosov crater, we find an α value of ∼4.5 between 3 and 8 crater radii. The spatial density at ∼8 crater radii is very close to the spatial density of the reference region, indicating that there

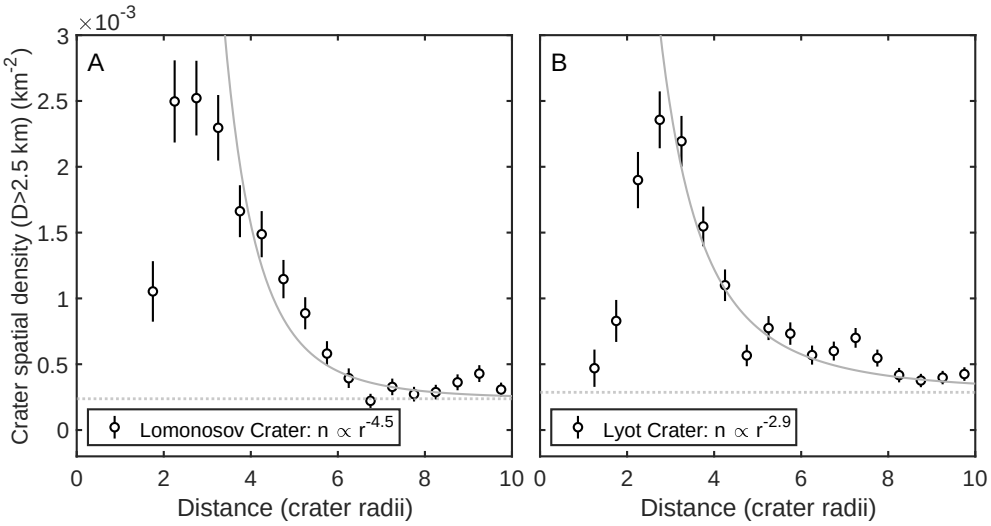

Figure 2.5: The decrease in the spatial density of >2.5 km craters radially away from (A) Lomonosov and (B) Lyot crater. A power law is fit to the spatial density above background to characterize the drop-off of inferred secondaries. The background spatial density, indicated by the dotted line, is defined as the spatial density of >2.5 km craters in the reference region.

are few >2.5 km secondaries at this distance.

For Lyot crater, we find an α value of $\sim$2.9, a more gradual drop-off in inferred secondaries than we observe for Lomonosov. There are several possible explanations for this difference: (1) Lyot crater impacted close to the heavily cratered Martian highlands, which may result in more primaries in the region around Lyot than there are in the reference region. Even at a distance of 8–10 crater radii, the crater spatial density is slightly greater than that of the reference region. If the background spatial density in figure 2.5B is adjusted to be the average value at 8–10 crater radii, the radial drop-off of inferred secondaries has an α similar to that of Lomonosov. However, the reference and secondary regions agree for large craters (figure 2.4B), indicating that both regions are likely sampling fairly similar terrain. (2) Interestingly, the peak crater spatial density around Lyot is slightly lower than around Lomonosov, despite Lyot being significantly larger and presumably capable of producing many more secondaries of any given size. Lyot also requires a lower value of f than Lomonosov (figure 2.4B),

indicating that Lyot's secondary field contains fewer secondaries than Lomonosov relative to its size. One explanation for this difference may be that many of Lyot's proximal secondaries have been degraded. Inspection of Lyot's nearby secondary field reveals many subdued, irregular depressions that are not classified as craters in the Robbins and Hynek (2012) catalog, but which may have been distinct craters in the past. In comparison, the secondaries around Lomonosov are more circular and have noticeably sharper rims. This could also explain the relatively gradual drop-off of secondaries away from Lyot; if the peak spatial density was greater, this would result in a more rapid drop-off with distance. (3) It is also possible that Lyot simply produced fewer secondaries relative to its size than Lomonosov, and that these secondaries were emplaced at relatively greater distances.

If the drop-off behavior we observe for Lomonosov and Lyot continues beyond the region we consider here, we infer that 70–95% of all secondaries should be between 2.5 and 8 crater radii, and 5–30% may be formed at greater ranges. This is roughly consistent with Robbins and Hynek (2011a) who found about an order-of-magnitude fewer distant secondaries of Lyot crater than nearby secondaries, though that study did not account for distant secondaries that were not obviously clustered and only clusters with a majority of craters larger than $\sim$1 km were considered. We emphasize that additional work characterizing the number and spatial distribution of distant secondaries is necessary.

2.6 Model of the global secondary SFD

Soderblom et al. (1974) provide a framework for analytically modeling the global secondary SFD, which we present here with some modifications: (1) we consider a more realistic non–power law PF for primary craters and (2) we consider that the number of secondaries produced by each primary may be greater than previously thought. The global secondary crater SFD is the sum of the secondaries produced by each individual primary (Shoemaker, 1965; Soderblom et al., 1974):

$$N_s = \sum_{i=1}^{\infty} N_{s,i} = \sum_{i=1}^{\infty} (f D_p(i))^{b_s} D^{-b_s} \tag{2.4}$$

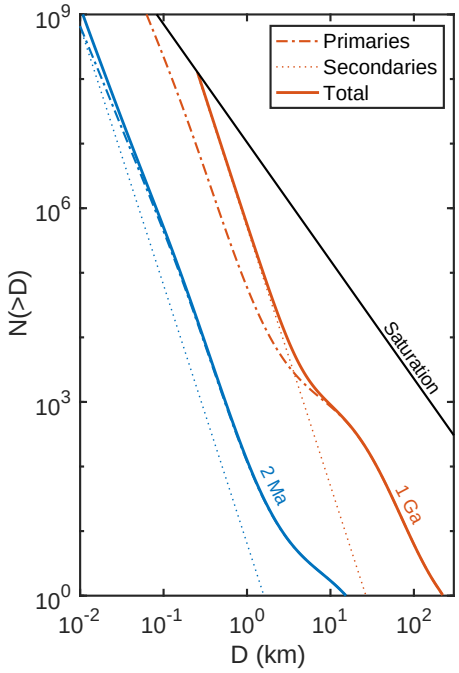

Figure 2.6: The predicted global cumulative SFD of primary and secondary craters produced on Mars after 2 Ma and 1 Ga using $f = 10\%$ and $b_s = 4$. The primary SFD is determined by the Ivanov PF. The secondary SFD is determined by summing the SFD of secondaries produced by all primaries (equation 2.4). Most km-scale craters are primary on Ma timescales. However, after 1 Ga, secondaries dominate the global SFD for craters smaller than a few kilometers. This demonstrates that the global crossover diameter increases with time. The black line indicates saturation equilibrium (Hartmann, 1984).

where $D_{p,i}$ is the diameter of the ith largest primary crater formed on Mars after some time, b_s is the power-law slope of secondaries, and f is the ratio between the size of the expected largest secondary to the size of the primary. This is a slight modification from Soderblom et al. (1974) who integrated over all primaries instead of using a discrete sum. However, our approach is more easily applied to arbitrary primary SFDs. The size distribution of primary craters is determined by a PF. The global secondary SFD can be calculated for any primary PF by solving equation 2.4 numerically (our results shown in figure 2.6, figure 2.7 use the Ivanov PF). However, we first consider the simple case where the primary SFD follows a power-law distribution with a constant cratering rate as this has a closed-form analytical solution. The cumulative number of primary craters on Mars after some time assuming a power-law PF is as follows:

$$N_p = CD^{-b_p} = (\gamma At)D^{-b_p} \tag{2.5}$$

where A is area (of Mars in this case), t is time, and γ is a constant cratering rate. The primary slope, b_p, has been shown to vary with size but is $\sim$2 on average for craters larger than 1 km. We rearrange equation 2.5 to find the diameter of the ith largest crater:

$$D_p(i) = (\gamma At/i)^{1/b_p} \tag{2.6}$$

Substituting equation 2.6 into equation 2.4, we obtain the cumulative number of secondaries produced by a power-law distribution of primaries:

$$N_s = f^{b_s}(\gamma At)^{b_s/b_p} D^{-b_s} \cdot \sum_{i=1}^{\infty} i^{-b_s/b_p} \tag{2.7}$$

The factor outside of the summation is the expression for the secondary SFD produced by the single largest primary. The summation is a coefficient that scales this to account for all primary craters. For $b_s > b_p$, this converges to the Riemann zeta function, $\zeta(b_s/b_p)$. For reasonable values of and ($\sim$4 and $\sim$2), ζ is $\sim$1.64, so the secondaries produced by the single largest primary account for a large percentage of the total number of secondaries: $1/\zeta \approx 60\%$.

$$N_s = f^{b_s}(\gamma At)^{b_s/b_p}\zeta(b_s/b_p) \cdot D^{-b_s} \tag{2.8}$$

Equation 2.8 reveals several interesting behaviors of secondary accumulation not exhibited by primaries. Most notably, secondaries accumulate non-linearly with time, even for a constant primary cratering rate: $N_s \propto t^{b_s/b_p}$. This is because nearly all of the secondaries are produced by the largest several primaries, and the size of the largest primary increases with time (equation 2.6). A consequence of this is that the secondary SFD "moves" relative to the primary SFD, causing the crossover diameter to progress to larger sizes for greater ages (figure 2.6). This has been noted by several authors (Neukum, 1983; Neukum and Ivanov, 1994; McEwen et al., 2005; Werner et al., 2009; Robbins and Hynek, 2014); however, the expression presented here illustrates why this must be the case. This also shows that background secondaries should not accumulate steadily with time.

The secondary SFD also depends non-linearly on the surface area of the planet as A^{b_s/b_p}; a larger "accumulation surface" will collect larger craters than a smaller one during the same interval. For example, the surface area of Mars is 3.8 times the surface area of the Moon. Ignoring differences in the primary production or secondary formation between these two bodies (though effects like gravity, target properties, and typical impact velocity certainly play a role (Bierhaus et al., 2018)), we might expect a factor of ∼14 more secondaries form on Mars than the Moon during the same time interval simply as a consequence of a larger surface area, though preservation differences will significantly influence what is visible today.

The scale factor f^{b_s} indicates that the secondary SFD is extremely sensitive to the distribution of secondaries produced by each primary. Previous studies of global secondary accumulation have used $f \approx 5\%$ (Soderblom et al., 1974; Werner et al., 2009). In section 2.5.1, we suggest that the population of km-scale secondaries around several large primary craters requires an f that may be as high as 10%.

This doubling of f corresponds to an increase in the global secondary SFD by a factor of 16 for $b_s = 4$. Figure 2.7 shows the evolution of the global mean crossover diameter with time calculated for two PFs: (1) a simple two-branch power-law model with an increase in slope below ∼1 km and (2) the Ivanov PF that was calculated numerically from equation 2.4. These models agree fairly well when considering ∼km-sized craters on Ga timescales,

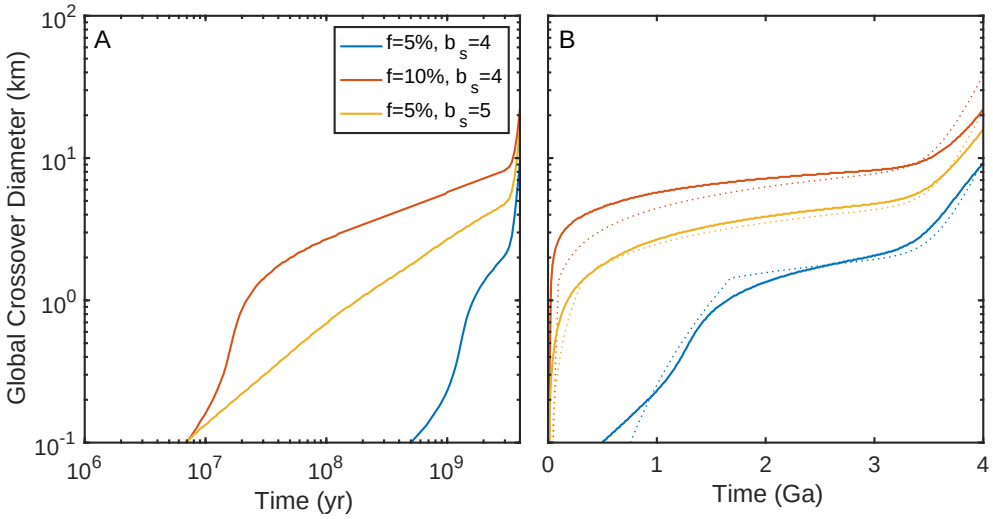

Figure 2.7: The global crossover diameter between primary and secondary craters for various values of f and b_s. For (A), time is in log-scale and shows the period from 1 Ma to 4 Ga; For (B), time is linear and focuses on Ga timescales. The primary SFD is determined by the Ivanov PF and the secondary SFD is calculated using equation 2.4. The dotted lines show the crossover diameter predicted for a hypothetical two-branch primary production: $b_p = 2$ for craters >1 km and $b_p = 3.7$ for craters <1 km. The global crossover diameter is very sensitive to f and b_s, which determine the number of secondaries produced by each primary.

though variations in the Ivanov PF above 1 km result in factor of 2–3 offsets between the two models. Using values of $f = 5\%$ and $b_s = 4$, the global crossover diameter exceeds 1 km after ∼1.5–2 Ga, consistent with the findings of Werner et al. (2009). However, for $f = 10\%$, the global crossover diameter exceeds 1 km for surfaces as young as ∼20 Ma. This sensitivity highlights the necessity for improved models and measurements of the production of secondary craters.

This model implicitly assumes that the secondary SFD maintains a steep slope for all diameters. However, for a steep power-law distribution, the total volume of ejected fragments necessary to produce progressively smaller secondaries eventually exceeds the total mass excavated by the primary (Melosh, 1989; McEwen et al., 2005). Therefore steep SFDs cannot continue to arbitrarily small sizes and must level off after some number of secondaries are produced. The number of secondaries that a primary is able to produce is difficult to observe, but perhaps the best estimate comes from young craters with well-preserved secondary fields. Zunil (10.1 km) is estimated to have produced $\sim 10^8$ decameter-sized craters (McEwen et al., 2005; Preblich et al., 2007). Williams (2018) estimate that Corinto crater (13.8 km) produced over 10^9 meter-to-decameter sized secondary craters with fairly steep-sloped SFDs at these sizes. This may continue to smaller sizes, though resolution limitations prevent the observation of this. Additionally, modeling work by McEwen et al. (2005) suggests that the production of this many secondaries does not violate reasonable physical constraints. For surfaces older than a few Ma, global crossover occurs before 10^8 craters are produced (figure 2.6). Therefore the results presented in figure 2.7 would not be significantly affected for surfaces older than this if 10^8 craters is the appropriate constraint. As the crossover diameter increases with time, the number of secondaries required to reach crossover decreases. For example, the global crossover diameter after 1 Ga occurs at just a few thousand secondary craters (figure 2.6).

It is important to note that figure 2.7 presents the globally averaged crossover diameter. If these secondaries were uniformly distributed across the surface of Mars, this would imply that 1 km craters could not be used reliably for chronology on Ga old surfaces. However,

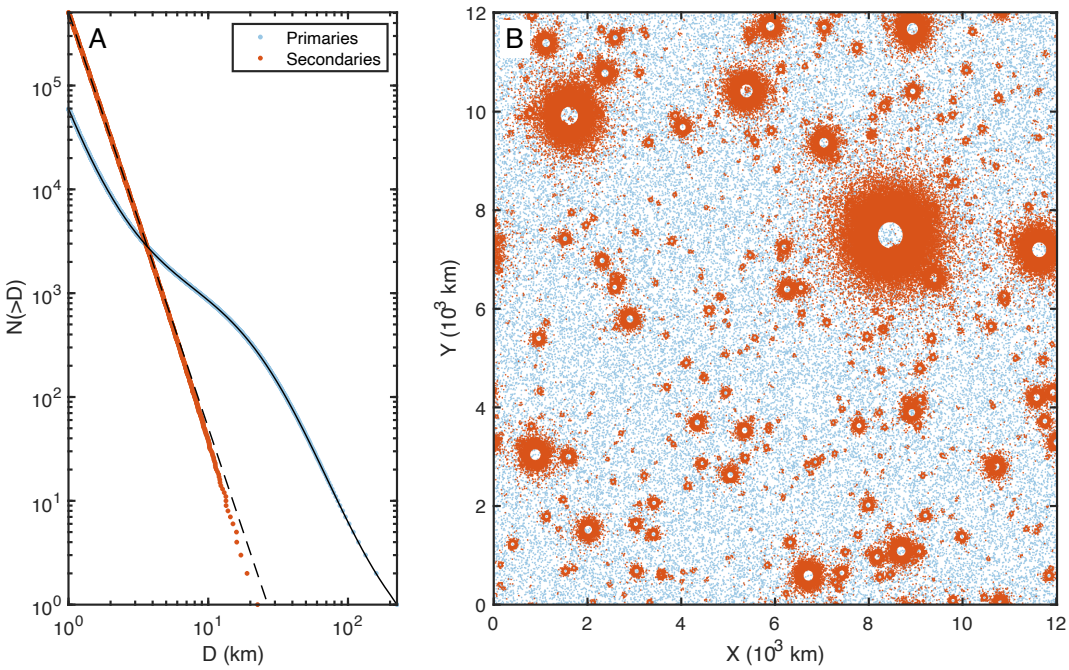

Figure 2.8: Example of a simulated (A) size-frequency distribution and (B) map of primary and secondary craters for a Mars-sized surface after 1 Ga. Each primary crater produces secondaries determined by $f = 10\%$, $b_s = 4$, and $\alpha = 5$. For clarity, only craters larger than 1 km are shown. The total number of km-scale secondaries globally is about an order-of–magnitude greater than the number of primaries. However, secondaries are clustered around large primary craters, resulting in some regions with many secondary craters and others with relatively few.

most secondaries are clustered within the regions proximal to the largest few primaries. These can be easily removed from counts or avoided. The relative abundance of distant field secondaries in regions that are not clearly influenced by nearby large primaries is the more relevant question for crater chronology, and the spatial distribution of secondaries becomes important.

2.7 Model of the spatial distribution of secondaries

We develop a model which accounts for the spatial distribution of secondary craters. Primary craters are stochastically placed on a Mars-sized surface and each primary produces a distribution of secondaries determined by parameters f and b_s. However, instead of placing secondaries uniformly on the surface, secondary spatial density drops off radially from each primary as $n \propto r^{-\alpha}$ with the maximum spatial density at 2.5 crater radii. Based on our observations of Lomonosov crater, we model secondary accumulation using $f = 10\%$, $b_s = 4$, and α values of 4 and 5 (figure 2.5). We also include model results based on Lyot crater ($f = 7\%$, $b_s = 4$, and $\alpha = 3$), which has fewer secondaries than Lomonosov relative to its size but with a more gradual drop-off with distance. However, we note that the parameters determined for Lyot may be influenced by the erasure of secondaries or by regional variations in the background spatial density of primaries (discussed in section 2.5.1). For a given simulation, we model the production of all primary and secondary craters that are larger than a specified minimum diameter, which is selected such that $\sim 10^7$ craters are produced in total (e.g., this threshold is 500 m for a 1 Ga surface). The surface is then gridded and the spatial density of primaries and secondaries within each bin is calculated. The local crossover diameter within each bin is determined by extrapolating the SFD of primaries and secondaries to smaller sizes and calculating the diameter at which their differential SFDs intersect. While we apply this model to Mars, it can be adapted for any planetary body if the number and spatial distribution of secondaries produced by primaries is constrained (accounting for differences in gravity, impact velocity, etc.).

Figure 2.8 shows model results for a 1 Ga surface using parameters: $b_s = 4$, $f = 0.1$, and $\alpha = 5$. Globally, there is an order of magnitude more km-scale secondaries than primaries. Primary craters >1 km are uniformly distributed across the surface with a mean spatial density of $\sim 3 \times 10^{-4}$ km^{-2}. The secondary spatial density can exceed this by several orders of magnitude in regions close to large primaries but is much lower elsewhere. Figure 2.9A and B show cumulative histograms for primary and secondary crater spatial density compared to

the global average. As expected, primary spatial density is normally distributed around the global mean. However, the global mean secondary spatial density is not a good predictor for a typical region on the surface of Mars. For a model run using Lomonosov-like parameters and $\alpha = 5$, the fraction of secondaries larger than 1 km on a median surface (corresponding to a CDF value of 0.5) is ∼19%, significantly lower than the global average of ∼90%. For a model run using $\alpha = 4$, secondaries are distributed at greater range and ∼38% of craters >1 km on a median surface are secondaries. When using Lyot-like parameters, secondaries are even more spatially uniform, but the global mean fraction of secondaries is lower due to fewer secondaries overall. These results agree qualitatively with the modeling results of Bierhaus et al. (2018) for the Moon, who showed that the maximum and minimum spatial densities of secondaries vary quite significantly across the surface compared to the more homogeneous primary population.

Figure 2.9C presents cumulative histograms showing the spatial variation in crossover diameter for modeled surfaces of various ages. The crossover diameter for a median surface after 1 Ga is between 70 and 300 m depending on the model parameters considered. Figure 2.10 shows the evolution of the median crossover diameter with time. The median crossover diameter exceeds 1 km on surfaces older than ∼1–2 Ga. This suggests that secondaries may contaminate counts for craters of this size on Ga old terrains, even in regions that are not obviously affected by large primaries. However, at 100 Ma the median crossover diameter is less than 10 m, which is about the limit of what can be easily counted using current orbital imagery. This suggest that distant secondaries should not influence counts on young (<100 Ma) surfaces known to be far from obvious sources of secondary craters. We note that the radial drop-off in secondaries, α, is not well constrained, and further study of the distribution of distant secondaries would help to inform this model. However, any radial drop-off will result in spatial clustering and cause the behavior shown in figure 2.8, figure 2.9, figure 2.10.

Our model likely overestimates the effect of secondaries in several ways. We do not account for possible focusing of secondaries along rays. Clustering of secondary craters azimuthally would further exaggerate the differences in local secondary spatial density. Ad-

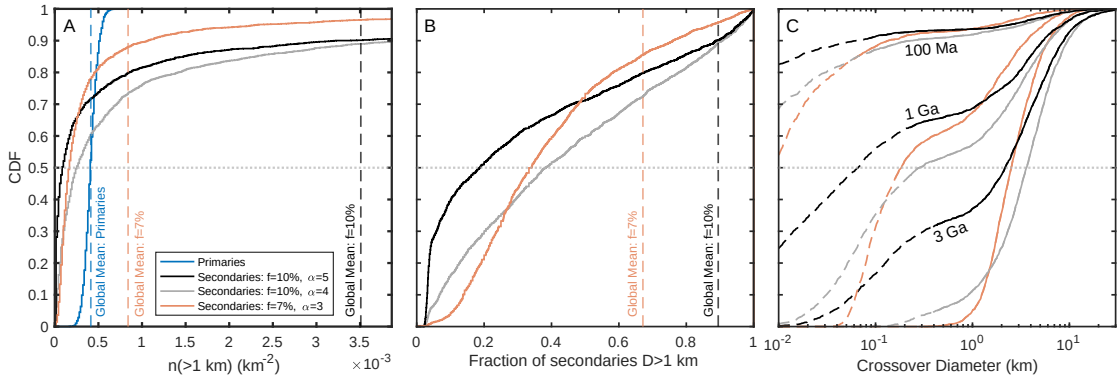

Figure 2.9: Primary and secondary accumulation modeled using parameters informed by Lomonosov crater ($f = 10\%$, $b_s = 4$, and α values of 4 and 5) and Lyot crater ($f = 7\%$, $b_s = 4$, and $\alpha = 3$). (A) Cumulative histograms of the spatial density of primary and secondary craters >1 km after 1 Ga. The spatial density of primary craters is normally distributed around the global mean. However, most secondaries are clustered around large primaries and the median secondary spatial density (indicated by a CDF value of 0.5) is significantly lower than the global mean. (B) Cumulative histogram of the local fraction of secondaries >1 km after 1 Ga. (C) Cumulative histograms of the local crossover diameter modeled for 100 Ma, 1 Ga, and 3 Ga. The histograms transition to dashed lines when the calculated crossover diameter requires the largest primary to produce more than 10^8 secondaries.

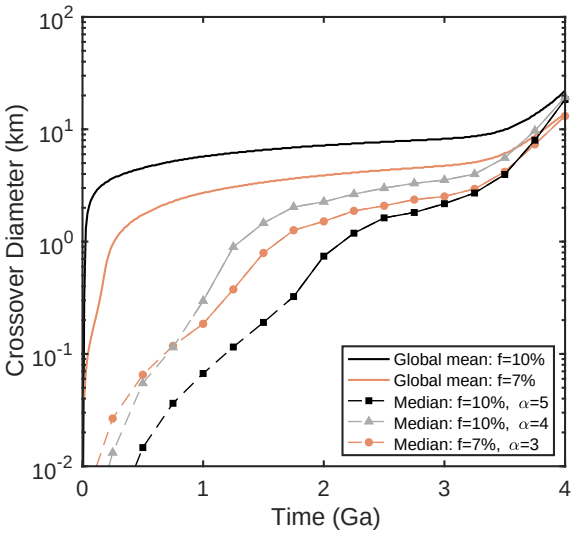

Figure 2.10: The global mean and median crossover diameter calculated for Mars using parameters informed by Lomonosov crater ($f = 10\%$, $b_s = 4$ and α values of 4 and 5) and Lyot crater ($f = 7\%$, $b_s = 4$ and $\alpha = 3$). The global mean crossover diameter is calculated using the approach described in section 2.6. The median crossover diameter, which accounts for the spatial distribution of secondaries, is significantly less than the global mean and is sensitive to α, which controls the spatial clustering of secondaries around primaries. The dashed lines show when the calculated crossover diameter requires the largest primary to produce more than 10^8 secondaries.

ditionally, like the analytical model presented in section 2.6, the determination of crossover diameter assumes that the secondary SFD maintains a steep slope at all diameters. Steep secondary SFDs cannot extend to arbitrarily small sizes. For reference, the dashed-line segments of figure 2.9, figure 2.10 show when the calculated crossover diameter requires the largest primary to produce more than 10^8 secondaries. If this is the appropriate threshold for the number of secondaries produced per primary, then our model overestimates local crossover diameters smaller than a few 100 m for Ga surfaces. The solid-line segments would be unaffected by a constraint of 10^8 craters. This model can be improved if the ray structure and number of secondaries per primary are better understood; however, we prefer to overestimate the contribution of secondaries from these effects in the absence of well-established constraints. This likely overestimate is valuable as it provides crater counters with an upper limit on the largest sizes that may be significantly affected by secondaries.

This model represents a production population and does not account for crater erasure by other craters (i.e., saturation equilibrium (Hartmann, 1984)) or erosion from process like infill. In reality, several processes preferentially erase small craters and many of the secondaries produced throughout Mars' past may no longer be observable today. This is apparent in figure 2.4, where km-scale craters, both primary and secondary, consistently deviate from the expected PF. Additionally, Lyot crater has the most obvious secondary field for a >200 km crater on Mars (Robbins and Hynek, 2011b), despite there being ∼50 craters of similar size or larger on the Martian surface. This indicates that the secondaries of many large primaries have been erased.

2.8 Conclusions

The observation of impact craters is the principal method for determining surface age throughout the solar system. Large primary craters can generate numerous smaller secondary craters nearly instantaneously. Many of these are distributed close to their primary or within obvious rays and can be excluded from crater counts. However, some distant

field secondaries are difficult to differentiate from primaries of the same size. Several young craters on Mars with well-preserved ray systems show that secondaries of a single primary can influence crater counts to distances of ∼100 crater radii (McEwen et al., 2005; Quantin et al., 2016; Williams, 2018; Williams et al., 2018b). The effect that secondaries have on the validity of crater chronology has been heavily debated and still remains a topic of significant discussion.

We present model results for the global accumulation of secondary craters on Mars, accounting for spatial clustering around large primaries. On Ga timescales the global number of >1 km secondary craters produced may exceed the number of primaries by an order of magnitude. However, most secondaries are contained within a few crater radii of the largest few primary craters. The contribution of distant field secondaries to regions that are far from obvious large primaries is lower. We predict the crossover diameter on a median surface after 1 Ga may be as large as 300 m, significantly lower than the global mean of ∼6 km but within the range of crater diameters which may be reasonably used for chronology. For surfaces younger than ∼100 Ma, we predict a median crossover diameter of <10 m, about the limit of what can be easily counted using existing orbital imagery. The median crossover diameter is expected to exceed 1 km on surfaces older than ∼1–2 Ga. These results likely overestimate the number of secondaries still visible today, as the secondaries of many old primaries have since been erased. The high spatial variability of secondaries suggests that care should be taken when counting craters on the scale of or smaller than the expected crossover diameter. Because the SFD of secondaries tends to have a steeper slope than that of primaries, an unexpected increase in slope at smaller sizes may indicate the presence of secondary craters.

The global accumulation of secondary craters is sensitive to the number and spatial distribution of secondaries produced by individual primary craters. Several large (∼20-220 km) craters on Mars show noticeable enhancements in the number of 1-10 km craters in their nearby regions (Robbins and Hynek, 2011b), likely the result of secondaries. We investigate four of these Martian craters and show that the number of secondaries required to explain the observed excess in km-scale craters is greater than previously thought, assuming no or

equal erasure of primaries and secondaries. The spatial density of secondary craters drops off rapidly radially away from these craters, making characterization of secondaries beyond ∼8 crater radii difficult. The number and spatial distribution of distant secondaries produced by primaries of various sizes remains poorly constrained. We recommend further study of distant secondary populations to better quantify their SFD, radial distribution, and degree of clustering along rays.

Acknowledgements

The authors would like to thank Michelle Kirchoff and Stuart Robbins for their valuable insight and feedback on the manuscript during the review process. The contributions of J.-P. Williams were funded by a NASA Solar System Workings grant no. 80NSSC18K0010.

CHAPTER 3

High-resolution nighttime temperature and rock abundance mapping of the Moon using the Diviner Lunar Radiometer Experiment with a model for topographic removal

This chapter was published in: Powell, T.M., Horvath, T., Lopez-Robles, V., Williams, J.-P., Hayne, P.O., Gallinger, C.L., Greenhagen, B.T., McDougall, D.S., and Paige, D.A. (2023). High-resolution nighttime temperature and rock abundance mapping of the Moon using the Diviner Lunar Radiometer Experiment with a model for topographic removal. *Journal of Geophysical Research: Planets*, 128, e2022JE007532.

Abstract

The Diviner Lunar Radiometer Experiment on the Lunar Reconnaissance Orbiter (LRO) has been mapping the surface temperatures of the Moon since 5 July 2009. Diviner has since collected over 500 billion radiometric measurements with excellent spatial and local time coverage. However, the most recently published high-resolution Diviner global maps only use data collected from 2009 to 2016. In this work, we compile ∼13 years of Diviner data to produce improved global maps of nighttime brightness temperature, bolometric temperature, regolith temperature, and rock abundance (RA). Errors in Diviner's pointing have been corrected and past effective field of view modeling has been optimized to improve data georeferencing without spatial interpolation. We estimate an effective resolution of ∼330 m

longitudinally and ∼700 m latitudinally at the equator, which corresponds to an improvement of ∼3.5× longitudinally and ∼1.3× latitudinally. In addition, we develop a thermal model that accounts for indirect scattering and emission from surrounding topography. The resulting temperature anomaly maps better highlight variations in temperature caused by thermophysical properties by removing most topographic effects. These improvements allow for the identification of smaller and fainter thermal features than was previously possible. The improved effective resolution of Diviner maps allows for excellent spatial correlation with other high-resolution data sets. To demonstrate this, we compare Diviner RA to a manual survey of boulders in the Apollo 17 landing site region. We show that Diviner RA correlates well with the areal fraction of rocks larger than ∼1-2 m in diameter visible in LRO Camera imagery.

3.1 Introduction

The Diviner Lunar Radiometer Experiment on the Lunar Reconnaissance Orbiter (LRO) has been mapping the reflected solar and emitted infrared radiation of the Moon since 5 July 2009 (Paige et al., 2010a). Since that time, Diviner has collected over 500 billion radiometric measurements. The Diviner data set has been used to create global and regional maps of surface temperature, derived thermophysical properties, and composition (Bandfield et al., 2011; Greenhagen et al., 2010; Hayne et al., 2017; Lucey et al., 2021; Paige et al., 2010b; Williams et al., 2017, 2019, 2022). However, the most recently published 128 pixel-per-degree (ppd) global maps (Bandfield et al., 2017; Greenhagen et al., 2011; Hayne et al., 2017) do not use data collected more recently than 2016.

In this work, we compile ∼13 years of Diviner data to produce updated nighttime brightness temperature, bolometric temperature, regolith temperature, and rock abundance (RA) maps of the Moon, which extend to ±70° latitude. The greater data volume results in substantially increased spatial and local time coverage. In addition, we implement several improvements which result in noticeably sharper maps with fewer data artifacts: a) Errors in

instrument pointing have been corrected, resulting in better georeferencing of Diviner measurements; b) past effective field of view (EFOV) modeling (Williams et al., 2016) used to determine the center of each Diviner observation accounting for topography and spacecraft motion has been optimized to produce sharper maps; and c) curve fitting of nighttime temperatures is used to calculate temperatures at a uniform local time. These updates allow for the exploration of the lunar thermal environment at a much finer scale than was previously possible.

Nighttime surface temperatures are strongly influenced by thermophysical properties, often characterized by thermal inertia which describes a material's resistance to changing temperature. High thermal inertia materials (e.g., rock) remain warmer throughout the night than lower thermal inertia materials (e.g., regolith). However, topography also affects surface temperatures. Local slopes influence the amount of direct solar illumination received by a particular surface, and the surrounding topography can scatter and emit radiation onto a surface which results in additional indirect heating (Aharonson and Schorghofer, 2006; Paige et al., 1994). It is often desirable to remove the effect of topography on nighttime temperature to better highlight variations in temperature that are caused by thermophysical properties. In this work, we present a model for topographic removal that accounts for scattered and emitted radiation from surrounding surfaces.

3.2 Data and methods

3.3 Diviner data set

Diviner is an infrared radiometer with nine spectral channels covering a wavelength range of 0.3-400 μm (Paige et al., 2010a). Channels 1 and 2 (0.3-3.0 μm) measure solar reflectance, channels 3-5 (7.80$\pm$0.25, 8.20$\pm$0.25, and 8.60$\pm$0.20 μm) measure the peak of the Christiansen thermal emission feature (Conel, 1969), which is indicative of silicate mineralogy (Greenhagen et al., 2010), and channels 6-9 (13-23, 25-41, 50-100, and 100-400 μm) measure

thermal emission over the wide range of lunar surface temperatures. Each channel consists of a 21-element thermopile detector array. Diviner normally operates as a nadir-pointing pushbroom mapper, though it can point off-nadir for targeted observations.

We collected Diviner Reduced Data Records (RDRs) for channel 6-9 from the start of the mission (July 2009) through July 2022. Data were restricted to emission angles less than 15° to avoid phase-angle dependent thermal emission behavior (Bandfield et al., 2015; Warren et al., 2019). We also employ several constraints on data quality described in the Diviner RDR's documentation (Sullivan et al., 2013): quality flag for calibration - 0; quality flag for miscellaneous - 0; noise quality flag - 0 to 1.5; activity flag - 110-192. Diviner radiance measurements were binned at 128 pixels-per-degree, which corresponds to ∼237 m at the equator, and in 0.25 lunar hour timesteps. Binned radiance values were then converted to brightness temperatures.

3.3.1 Correction of angular pointing offsets

In 2019, it was found that the Diviner instrument had been experiencing a systematic cross-track pointing offset since the start of the mission. This was discovered when analyzing features that were smaller than the effective field-of-view (EFOV) of a Diviner observation, such as lunar collapse pits (Horvath et al., 2019, 2022) and small rocky craters. These small, sub-resolution features should contribute to the temperature of only one spatial bin when gridded at 128 ppd; however, such features were observed to be several spatial bins wide in nighttime temperature maps derived from binning data throughout the night. Further investigation revealed that the apparent location of these features varied slightly in longitude for different orbits due to an unknown angular pointing error in Diviner's elevation actuator in the cross-track direction.

To characterize the angular pointing offset, we tracked the apparent location of several candidate targets throughout the duration of the mission. Suitable targets were selected based on the following criterion: a) about the size of or smaller than the EFOV of a single

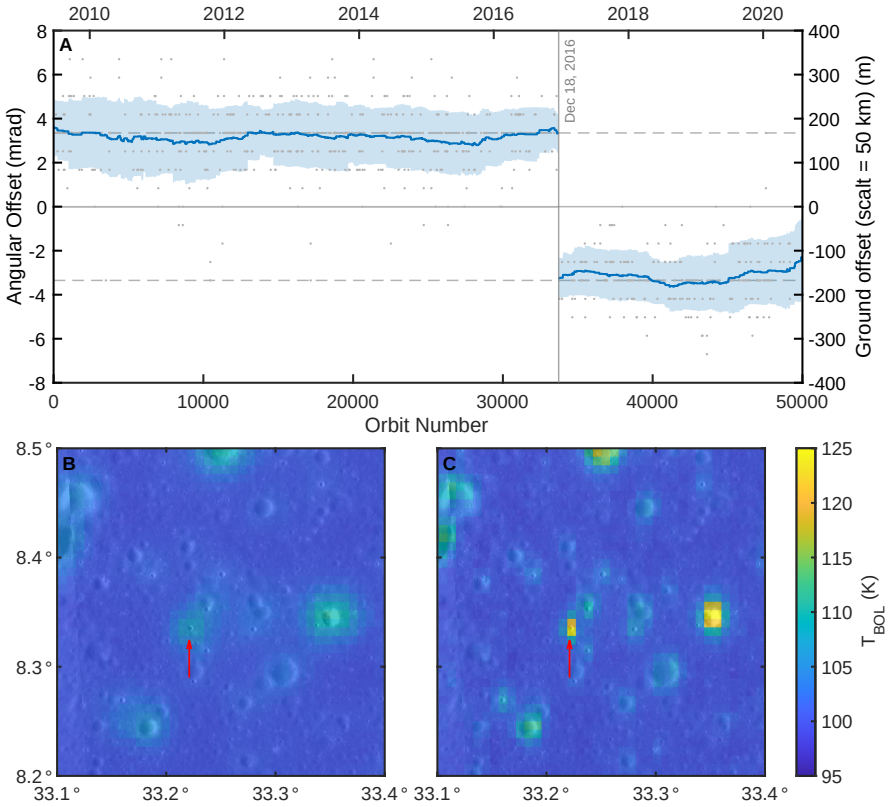

Figure 3.1: A) Cross-track angular offset versus time for Diviner where the positive and negative cross track direction is defined relative to the Diviner detector array. From the start of the mission until December 2016, Diviner observations were offset by ∼3.4 mrad. After December 2016 the detector offset was also ∼3.4 mrad, but in the opposite cross-track direction. The blue line was constructed using a rolling average with a window of 5000 orbits. B and C) Example of midnight bolometric temperatures for a region before (B) and after (C) the angular offset correction in (A) and the updated effective field-of-view modeling approach (section 2.3) are applied. After correction, warm spatial bins correspond more accurately to geologic features like rocky impact craters, and the temperature magnitude is more pronounced. The warm feature at 8.33° N and 33.22° E (red arrow) is a collapse pit.

Diviner observation; and b) thermally pronounced from their surroundings throughout the night. We selected 13 targets consisting of lunar collapse pits and small rocky craters ranging in size from 100 to 300 m. We retrieved all channel 6-7 Diviner data with $<10^{\circ}$ emission angles and manually measured the offset between their apparent location and the true target location in LRO Camera (LROC) Narrow Angle Camera (NAC) imagery. This was converted to an angular offset by accounting for spacecraft altitude and orientation. On average, there were $\sim$25 observations per target per channel. Figure 3.1A shows the trend of the angular offset magnitude and direction throughout the mission duration. The offset was approximately constant at $\sim$3.4 mrad in the positive cross-track direction (defined relative to the Diviner detector array) from the start of the mission until December 2016. This is equivalent to a ground-projected offset of $\sim$170 m at a spacecraft altitude of 50 km, or $\sim$70% of an equatorial 128 ppd spatial bin. Although the offset was roughly constant during this period, this does not mean that targets were simply shifted in early Diviner maps. LRO occasionally performs 180° yaw flips to maintain the Sun on the solar array side of the spacecraft, resulting in the detector arrays reversing direction relative to the spacecraft in-track direction (Tooley et al., 2010). Therefore, a target's apparent location can vary by $\sim$3.4 mrad from its true location in either longitudinal direction when binned spatially, depending on the orientation of the spacecraft. In December 2016, the angular pointing offset abruptly shifted to $\sim$3.4 mrad in the negative cross-track direction. This was found to correspond with the Diviner instrument temporarily entering safe mode from 15 to 18 December 2016 after registering multiple actuator position errors.

Offsets in the georeferencing of Diviner observations leads to blurring of features, hence decreasing the effective resolution of the measurements when creating binned maps. This is especially apparent for small features and sharp thermal contrasts. Data from a particular point on the surface will pollute adjacent bins, suppressing unique thermal signals and causing sharp thermal boundaries to become blurred. Luckily, because the angular pointing error has been fairly predictable with time, we can use the results of figure 3.1A as a calibration to properly georeference Diviner data. The result of this correction applied to Diviner

bolometric temperature is shown in figure 3.1 B and C. This lunar mare example region contains several rocky craters and a lunar collapse pit (8.33° N, 33.22° E) which have elevated nighttime temperatures. Figure 3.1B shows the bolometric temperature at midnight without correcting for the Diviner pointing offsets or using the updated approach to EFOV modeling, which we discuss in section 2.3. In this map, thermal features are smeared in the longitudinal direction and temperatures are muted because of incorrectly georeferenced observations originating from neighboring spatial bins. Figure 3.1C shows the same region but applies the pointing correction and the updated EFOV modeling approach (section 2.3). With these improvements applied, thermal features are properly localized to their corresponding geologic features. While both maps are binned at 128 ppd, the ability to resolve smaller features in the new maps demonstrates an increase in effective resolution. For example, the apparent size of the temperature feature associated with the lunar collapse pit is ∼3-4 pixels wide before the corrections are applied and ∼1-2 pixels wide afterward. Additionally, the thermal contrast between warm and cool regions is substantially improved, allowing fainter thermal features to be identified than was previously possible.

3.3.2 Effective field-of-view modeling

Diviner data is typically stored as a point-based data set with measurements centered at the temporal midpoint of the observation. This sometimes results in gaps in data when spatially binning, especially when the LRO spacecraft is at a greater altitude. Williams et al. (2016) presents a method for determining the ground-projected EFOV of a Diviner measurement accounting for spacecraft viewing geometry and motion, surface topography, and the thermal response time of each detector. Figure 3.2A-C shows the ground projected footprint of a single Diviner channel 7 detector measurement at several spacecraft altitudes. In past maps, spatial bins which were within the EFOV of a measurement but did not contain the center-point of the measurement were populated with data. This allowed all bins within the ground track observed by Diviner to be filled in, which was necessary for previous Diviner products to achieve sufficient spatial coverage. However, this can result in some blurring due to

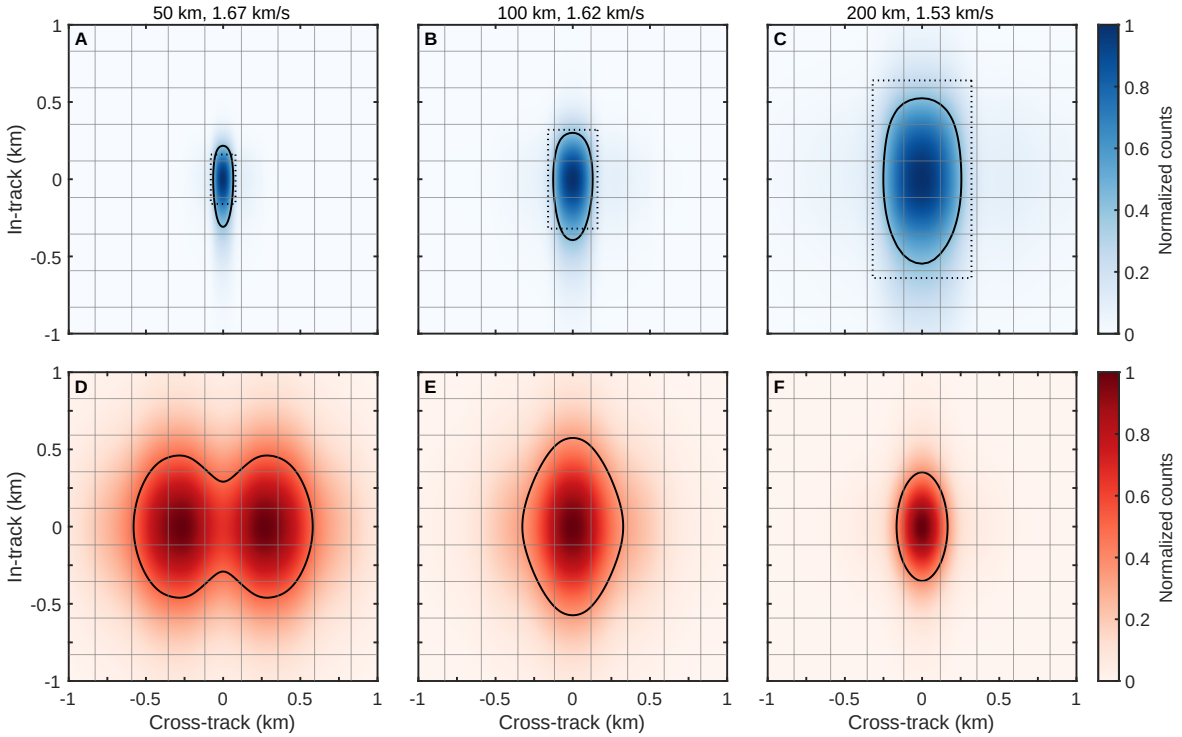

Figure 3.2: A-C) The effective field-of-view of a Diviner detector observation at several spacecraft altitudes. The black contours outline the region within which 50% of the observation response originates. The gray lines represent a 128 ppd grid at the equator, and the dotted rectangle shows the nominal instantaneous field of view of a Diviner detector (Paige et al., 2010a; Williams et al., 2016). D-F) the modeled spatial response function (SRF) for an equatorial 128 ppd spatial bin, constructed for the following approaches: D) no correction for detector offsets and neighboring observations contribute to the target spatial bin's response; E) offsets are corrected and neighboring observations contribute to the target spatial bin's response; and F) offsets are corrected and only observations centered within the target spatial bin contribute to the bin's response.

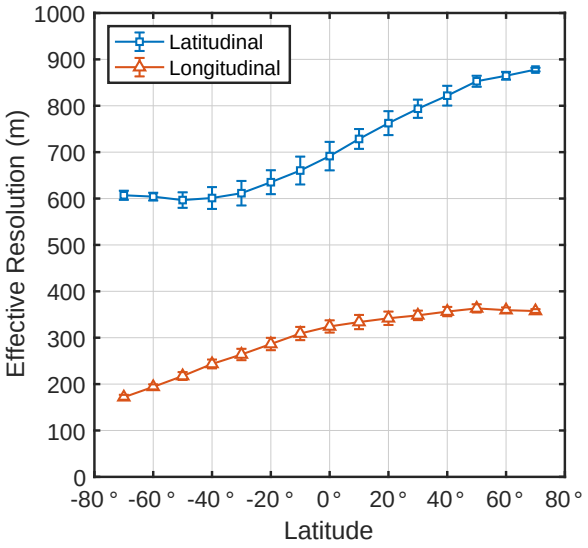

Figure 3.3: The effective resolution of a 128 ppd spatial bin in the longitudinal and latitudinal direction as a function of latitude. The marker at each latitude shows the average and standard deviation of the effective resolution determined for 8 locations with varying longitude at that latitude.

averaging of radiances from adjacent overlapping EFOVs, particularly at sharp boundaries in temperature. In this work, we use the Williams et al. (2016) method to find the center-point of each Diviner observation's EFOV, but we do not populate neighboring bins. This is now possible because of the greater data volume from ∼13 years of Diviner observation. The resulting maps benefit from a reduction in averaging between overlapping observations that better isolates the individual brightness temperature measurements while the higher density of the current data provides adequate spatial coverage to eliminate gaps in binned data at this resolution. This approach, along with the correction to the Diviner pointing errors, results in noticeably sharper temperature maps.

To demonstrate the improvement in map sharpness, we model the "spatial response function" (SRF) for a 128 ppd spatial bin considering that the value of a particular spatial bin is constructed by averaging several Diviner observations which have their own unique EFOV. For eight equatorial locations, we collect all Diviner data recorded throughout the duration of the mission and simulate the EFOV of each individual detector measurement accounting for the location of the observation, spacecraft and detector array orientation (traveling either north-south or south-north), spacecraft velocity, and spacecraft altitude (Williams et al., 2016). To produce the SRF, the EFOV of all measurements are weighted by the proportion that they contribute to the target pixel and are summed. Figure 3.2D simulates the SRF of the previously published Diviner maps, where pointing offsets are not corrected for and Diviner measurements centered outside of the target spatial bin contribute to the value of the bin. The black contour outlines the region that contributes to 50% of the total response. We define the extent of this region as the effective resolution. This shows that the equatorial effective resolution of the previously published Diviner maps is ∼1.15 km by ∼920 m in the longitudinal and latitudinal directions, respectively. For reference, the nominal size of a 128 ppd spatial bin at the equator is ∼237 m in both directions. Figure 3.2E uses the same EFOV modeling approach as figure 3.2D but includes a correction for pointing offsets. Figure 3.2F both corrects for pointing offsets and uses the updated EFOV modeling approach, where only observations whose centers fall within the target spatial bin

are considered. The effective resolution of a spatial bin at the equator following this method is ∼330 m by ∼700 m in the longitudinal and latitudinal directions, respectively. This constitutes an improvement of ∼3.5× longitudinally and ∼1.3× latitudinally.

The effective resolution of a spatial bin is also expected to vary in size with latitude due to differences in spacecraft altitude. During the first ∼2 years of operation, LRO was in a near-circular polar orbit with an average altitude of ∼50 km (Mazarico et al., 2012, 2018). LRO then transitioned to a quasi-frozen elliptical orbit with periapsis near the South Pole and spacecraft altitude varying between ∼30 and ∼180 km, and the orbit has continued to evolve throughout the duration of the mission (Mazarico et al., 2018). In general, this results in higher effective resolution in the southern hemisphere and lower effective resolution in the northern hemisphere. This is demonstrated in Figure 3.3, which shows the simulated effective resolution in the longitudinal and latitudinal directions as a function of latitude.

3.3.3 Slope-adjusted midnight brightness temperature

We create brightness temperature maps for channels 6-9 by calculating the temperature at a particular local time from the nighttime data using non-linear curve fitting. For each channel and 128 ppd spatial bin, we fit the nighttime cooling curve with an exponential function of the form: $T_B = Ae^{B/t} + C$ where T_B is brightness temperature, t is local time, and A, B, and C are constants (figure 3.4). This form was chosen empirically, as it reproduces the cooling curves on the Moon better than other simple mathematical forms (e.g., linear or polynomial). Data within half an hour of sunrise and sunset are excluded to avoid the complex illumination conditions that can occur near the terminator because of topography. We require that spatial bins have at least three nighttime observations, with at least one observation occurring both before and after midnight. Spatial bins that do not meet these criteria are assigned as null values. A typical 128 ppd spatial bin has ∼14 nighttime observations per channel which are used for fitting (figure 3.4), and only ∼0.003% of spatial bins do not meet the fitting criteria. The median fit standard error for each channel is 2.24 K, 0.74 K, 1.13 K, and 2.46 K for channels 6, 7, 8, and 9, respectively. The best-fit cooling curve is then used to calculate the

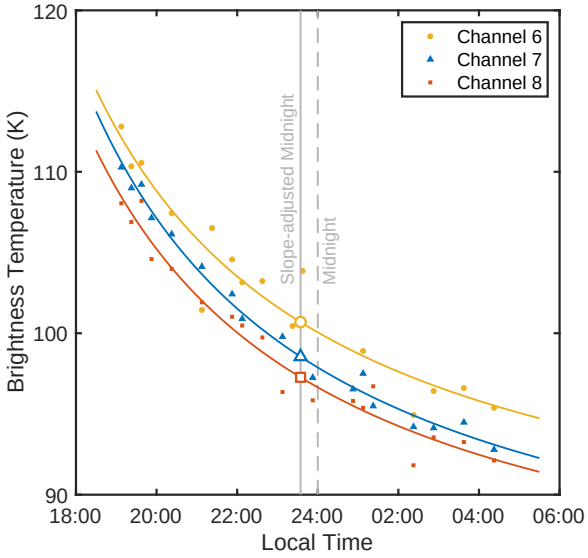

Figure 3.4: Channel 6-8 nighttime brightness temperature curves at an example location (-176.6523°E, -16.4492°N). Each nighttime curve is fit to an exponential function, which is used to calculate the temperature at midnight and slope-adjusted midnight. The surface has an east-west slope of ∼5.3°, so slope-adjusted midnight occurs ∼0.35 lunar hours earlier in the night.

brightness temperature at a particular local time. We produce brightness temperature maps for channels 6-9 at two local times: local midnight and "slope-adjusted midnight."

For flat surfaces, slope-adjusted midnight is equivalent to local midnight. However, for surfaces sloped in the east-west direction, the time of peak solar illumination is shifted in local time. To first order, the resulting diurnal temperature curve can be approximated by shifting the timing of the diurnal temperature curve of a flat surface by the local east-west slope angle (Hayne et al., 2017). The local slope angle is determined using the 128 ppd SLDEM 2015 topographic map, which merges SELENE Kaguya TC and LRO Lunar Orbiter Laser Altimeter elevation data (Barker et al., 2016). This correction removes some of the effects of topography on midnight temperatures. Further topographic corrections are discussed in section 3.

3.3.4 Bolometric temperature, regolith temperature, and rock abundance

A single Diviner observation may contain a distribution of temperatures due to the presence of spatially unresolved rocks and small-scale slopes within the detector FOV. This results in differences in the brightness temperatures recorded by each of the Diviner channels. Regions with a mixture of temperatures have greater brightness temperatures in the shorter wavelength channels. The bolometric temperature (T_{BOL}) approximates the wavelength-integrated flux from all Diviner channels as an equivalent blackbody temperature. This quantity is useful because it represents the total radiative heat flux leaving the surface expressed as an effective temperature. This makes bolometric temperature a good metric for comparison to thermal models, which generally represent the total heat balance of the surface. We use channels 6, 7, 8, and 9 to produce maps of midnight and slope-adjusted midnight bolometric temperature using the method described in (Paige et al., 2010b).

The differences in brightness temperature measured by each channel can also be leveraged to probe the sub-resolution mixture of temperatures for anisothermal surfaces. Most nighttime anisothermality on the Moon is caused by rocks, which have higher thermal iner-

tia than regolith and remain warmer throughout the night. Unequal heating of small-scale slopes also contributes to anisothermality, but at night, this generally has a smaller effect than the presence of high thermal inertia materials (Bandfield et al., 2015). Bandfield et al. (2011) presents a method for estimating the fraction of rocks larger than ∼1 m contained within a Diviner spatial bin. This process was used to produce the previous generation of RA and regolith temperature maps, which we briefly summarize here.

Bandfield et al. (2011) assumes that the surface is made of just two materials: rock and regolith. Rock temperatures are determined using a one-dimensional thermal model assuming the thermophysical properties of vesicular basalt as described by Horai and Simmons (1972), an albedo of 0.15, and a hemispherical emissivity of 0.95 (Bandfield et al., 2011). We construct a lookup table of rock temperatures at midnight and slope-adjusted midnight accounting for latitude, local slope geometry, shadowing, and scattered and emitted radiation from surrounding topography as described in section 3. For each spatial bin, we then find the mixture of rock and regolith temperatures that best fits the radiances observed by Diviner channels 6-8. This is done by simulating Diviner's spectral response for an imaginary surface with an unknown areal fraction of rock and regolith, where the rock temperature is determined from modeling and the regolith temperature is unknown. The derived RA and regolith temperature (T_{REG}) occur for the combination of these values that best fits the observed channel 6-8 radiance by minimizing RMS differences. We assume a nadir emissivity of unity for both rocks and regolith. Figure 3.5 shows derived bolometric temperature, regolith temperature, and RA for an example region.

Modeled rock temperatures assume an infinitely thick and laterally continuous layer of rock. This is an appropriate assumption for rocks that are sufficiently larger than the thermal skin depth (∼1 m for rock), so the resulting RA should be interpreted as the fraction of the surface covered with rocks larger than ∼1 m in diameter. However, it is important to note that this 2-component model is a simplification. In practice, the Diviner FOV may contain several different materials. Small rocks will have a different cooling behavior than large rocks, as they will eventually be cooled laterally by the surrounding regolith. Addi-

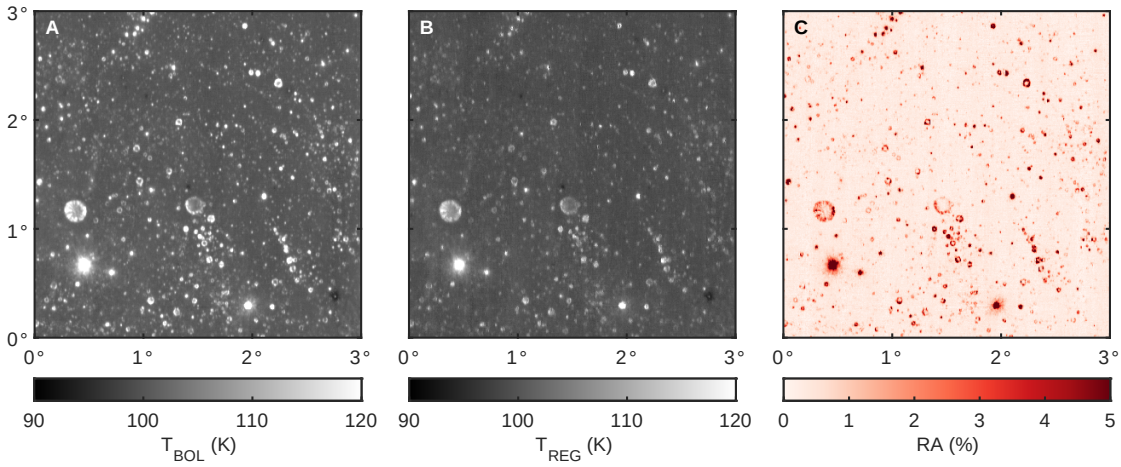

Figure 3.5: Examples of derived A) bolometric temperature, B) regolith temperature, and C) rock abundance at slope-adjusted midnight.

tionally, if rocks on the Moon have been heavily fractured or are covered by a thin layer of regolith, they may be cooler than a large, coherent rock due to differences in their thermophysical properties. For example, a 10% value in the derived RA map may correspond to a greater areal fraction of regolith covered rocks or small rocks. Additionally, derived regolith temperatures likely include some contribution from small rocks or regolith covered rocks, whose nighttime temperatures may be intermediate between typical regolith and coherent rock (figure 3.5B). This can be probed with more complicated models that account for more than two temperature components (Elder et al., 2016). However, this RA metric is a valuable way of interpreting the anisothermality observed by Diviner as a geologically relevant quantity and can be used to compare relative differences in RA between regions.

3.4 Thermal model for topography removal

Nighttime temperature maps are valuable because they are diagnostic of the thermophysical properties of the surface. However, spatial variations in temperature can also be caused by latitude and topography, so it is often desirable to remove these effects. Here we present a

model for topographic subtraction which uses a one-dimensional thermal model that accounts for latitude, slope, shadowing at sunrise and sunset, and scattered and emitted radiation from surrounding surfaces.

3.4.1 Direct solar illumination

Latitude is the dominant first-order effect that influences lunar surface temperatures, as it affects the solar incidence angle and the amount of direct solar illumination received throughout the day. Figure 3.6 shows the trend in median midnight bolometric temperature and regolith temperature with latitude for typical lunar regolith (excluding spatial bins with slopes $>2^\circ$ and rock abundances $>0.5\%$). Median midnight bolometric temperatures vary from $\sim$101 K at the equator to $\sim$83 K at 70° latitude. Median regolith temperatures are slightly cooler than bolometric temperatures. This difference is due to anisothermality, as the contribution from rocks is mostly removed in the calculation of regolith temperature, but is included in the bolometric temperature. Typical regolith has a low-level background RA of $\sim$0.3%.

We fit the trend in midnight temperatures with latitude using a one-dimensional finite volume thermal model based on Hayne et al. (2017). This model describes the vertical density structure of the regolith as an exponential increase in density ρ with depth z (Hayne et al., 2017; Vasavada et al., 2012):

$$\rho(z) = \rho_d - (\rho_d - \rho_s)e^{-z/H} \tag{3.1}$$

where ρ_s and ρ_d are the densities of the surface and at depth, respectively. The parameter H is an exponential scale height describing the thickness of the loosely packed surface layer. We find that an H of $\sim$6.74 cm best fits the trend of midnight regolith temperature with latitude, which agrees very well with the mean H-parameter calculated by Hayne et al. (2017) of $\sim$6.8 cm using the Bandfield et al. (2017) regolith temperatures. For midnight bolometric temperature, we find an H-parameter of $\sim$5.73 cm.

In addition to latitude, local slope also influences the amount of direct solar illumination

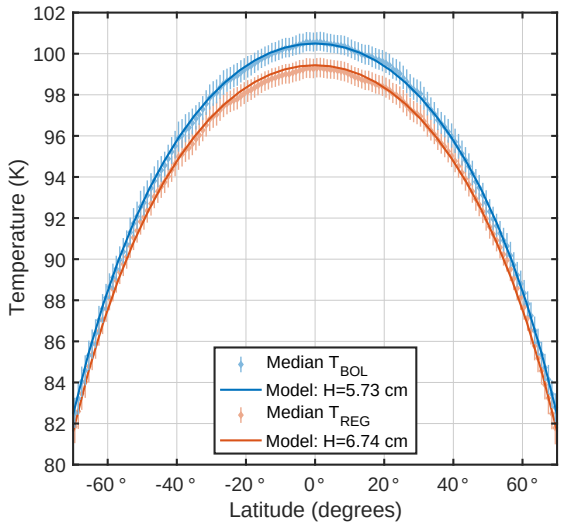

Figure 3.6: Median T_{BOL} and T_{REG} of flat and non-rocky surfaces (slope<2° and RA<0.5%) as a function latitude compared to a 1-dimensional thermal model based on Hayne et al. (2017). Error bars represent the interquartile range within each bin.

received. For example, a 10° pole-facing slope at 20° N latitude will experience the same solar incidence angle at noon as a flat surface located at 30° N latitude. Hayne et al. (2017) implemented a simple correction for slope where the "effective latitude" of a particular spatial bin is shifted from that of a flat surface by the north-south component of the slope. As described in section 3.1, Hayne et al. (2017) also adjusted the "effective local time" by the east-west component of the slope, which we replicate by calculating the temperature at slope-adjusted midnight.

3.4.2 Indirect scattered and emitted radiation

Topography can scatter and emit radiation onto surrounding surfaces. This indirect illumination results in additional heating. The radiative balance for a patch of ground that receives scattering and emission from surrounding topography is:

$$Q = Q_{solar} + Q_{emis} + Q_{scat} \tag{3.2}$$

where the total incoming radiation Q is the sum of direct solar illumination Q_{solar} and indirect illumination from the land in the form of scattered visible Q_{scat} and emitted infrared Q_{emis} radiation. The total amount of thermal emission from the surrounding land received at some time is determined by the radiative flux from each spatial bin within the line of sight of the target spatial bin weighted by the cosine of the incidence angle i and integrated over all spherical angles Ω (Aharonson and Schorghofer, 2006; Paige et al., 1994; Helbig et al., 2009):

$$Q_{emis} = \int \epsilon \sigma T^4 \cdot \frac{1}{\pi} \cos i d\Omega \tag{3.3}$$

where ϵ is emissivity, σ is the Stefan-Boltzmann constant, and T is the temperature of each spatial bin. This can be approximated as:

$$Q_{emis} = \epsilon \sigma T_{land}^4 \cdot \frac{1}{\pi} \int \cos i d\Omega = \epsilon \sigma T_{land}^4 \cdot f_{land} \tag{3.4}$$

where the land view factor f_{land} describes the amount of land within the target spatial bin's line of sight (weighted by $\cos i$), and T_{land} is an equivalent scene temperature which produces the same total emission as the entire scene. A similar equation exists for the incoming scattered visible light:

$$Q_{scat} = A Q_{land} \cdot f_{land} \tag{3.5}$$

where Q_{land} is the average solar flux incident on each spatial bin within the line of sight weighted by $\cos i$, and A is the albedo of the surroundings.

First, we use the SLDEM 2015 topographic map (Barker et al., 2016) to calculate f_{land}. The elevation angle α of a distant point above the horizon can be approximated as $\alpha = \arctan \frac{\Delta h}{L} - \frac{\theta}{2}$ where L is the distance to the point and Δh is the difference in elevation. The second term describes the drop-off of the horizon due to the curvature of the Moon, where θ is the central angle subtended by an arc to the distant point which can be calculated using the haversine formula. Figure 3.7 shows a panorama taken at the Apollo 17 landing site and the same scene constructed using the 128 ppd SLDEM 2015 topographic map. Calculating the elevation angle for every nearby spatial bin as shown in figure 3.7 is too computationally expensive to be repeated for every 128 ppd spatial bin on the Moon. Instead,

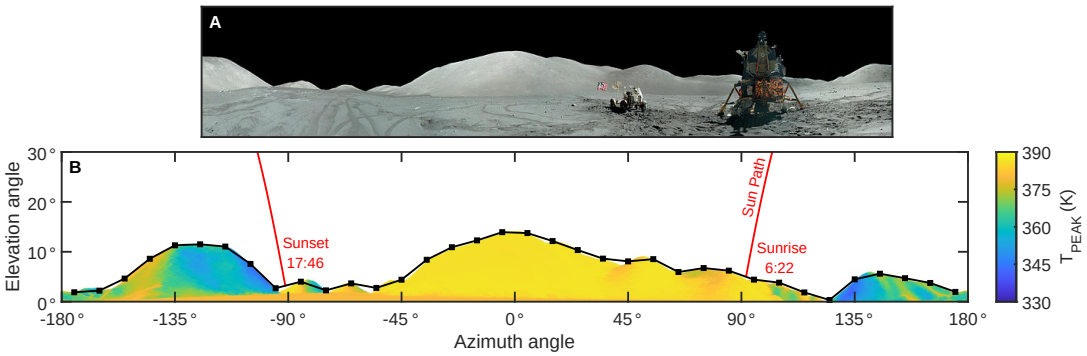

Figure 3.7: A) A panorama taken at the Apollo 17 landing site (30.772°E, 20.191°N) and B) a panorama of the same region constructed using the 128 ppd SLDEM 2015 topographic map (Barker et al., 2016). Peak temperatures for each 128 ppd spatial bin are calculated assuming radiative equilibrium with solar illumination and the emissivity and albedo values described in Hayne et al. (2017). The horizon profile and peak temperatures are used to calculate f_{land} and T_{land}, which describe the amount of scattered and re-emitted radiation that contribute to the energy balance at the Apollo 17 landing site. While this figure shows all 128 ppd spatial bins within the line of sight, the calculation of f_{land} and T_{land} is approximated by sampling along 10° azimuth angle and 1° elevation angle increments. The horizon profile is also used to calculate the sunrise and sunset times.

we only calculate elevation angle for spatial bins that lie along rays cast in 10° azimuth angle increments. A horizon profile is constructed by finding the maximum elevation angle along each of these rays (figure 3.7), and f_{land} is calculated by numerically integrating the horizon profile weighted by the incidence angle relative to the surface normal (equation 3.4).

Next, we calculate the equivalent temperature of the surrounding scene T_{land}. The behavior of the scene temperature throughout the day can be quite complicated, as particular surfaces within the line of sight may experience more solar illumination than others and may become illuminated at different times. Calculating a unique land emission diurnal curve for each spatial bin is computationally expensive and not easily scalable for a global map. However, equivalent scene temperatures throughout the day can be approximated by relating the temperature of the surrounding scene to that of a flat surface at some latitude which emits a similar total flux.

The peak temperature T_{peak} at slope-adjusted noon for each spatial bin within the line of sight is easily calculable based on their latitude and slope angle (section 3.1) by assuming radiative equilibrium with solar illumination (figure 3.7). We use the nominal emissivity and albedo values described in Hayne et al. (2017) which were found to be appropriate for the Moon on average, though this may introduce uncertainties in the surrounding temperatures due to regional differences in albedo and emissivity. We calculate the equivalent scene temperature T_{land} by sampling T_{peak} along rays cast in 10° azimuth angle increments and 1° elevation angle increments. The total flux from land emission Q_{emis} is calculated by numerically integrating equation 3.3. Equation 3.4 is then solved for T_{land}, which is a single scene temperature that produces the same total radiative flux as the entire scene. This equivalent temperature represents the maximum instantaneous emission received from each spatial bin within the line of sight at slope-adjusted noon. To estimate the emitted flux received at other times of the day, we determine the characteristic latitude ϕ_{land} which has the same maximum temperature. We use a one-dimensional thermal model (section 3.1) to approximate the diurnal temperature curve throughout the day at this characteristic latitude. This is also used to determine the solar illumination of the scene throughout the

day Q_{land}. While this method does not account for differences in the timing of illumination within the line of sight, it does approximate the total flux received from each surrounding spatial bin throughout the day.

Lastly, regions that are at the bottom of steep topography may also experience shadowing at sunrise and sunset, which reduces the total amount of illumination received throughout the day. We calculate the time of sunrise and sunset by finding the intersection of the horizon profile with the path of the sun in the sky (figure 3.7).

3.4.3 Selection of albedo and emissivity for land scattering and emission

The amount of emitted and scattered illumination radiated from the surroundings and absorbed by a patch of ground depends on the albedo and emissivity. Diviner results and photometric studies have shown that regolith is not a lambert scatter or emitter; apparent albedo and emissivity vary with the incidence angle of incoming solar illumination and the azimuth and emission angle of the measurement (Bandfield et al., 2015; Foote et al., 2020; Rubanenko et al., 2020; Warren et al., 2019; Winter and Krupp, 1971). This is often attributed to sub-resolution surface roughness which causes small-scale variations in illumination and shadowing. Typical slopes in the lunar highlands are $<10^\circ$ with slopes rarely exceeding 30° (Rosenburg et al., 2011), so most land emission and scattering comes from low in the sky. It is therefore necessary to select values of albedo and emissivity that are appropriate for these very high emission angles.

Foote et al. (2020) presents laboratory measurements of the directional albedo of Apollo soils at various incidence angles. We select a value of albedo of 0.15 which corresponds to the apparent albedo of Apollo 16 soil at $\sim 80^\circ$ emission angle for a nadir-illuminated target. Diviner has been performing systematic off-nadir observations at several points on the Moon to characterize the emission phase function of the lunar surface (Bandfield et al., 2015; Greenhagen et al., 2017). We look at off-nadir Diviner bolometric temperature measurements for two equatorial sites: highlands (141.39°E, 0.36°N) and mare (-54°E, -

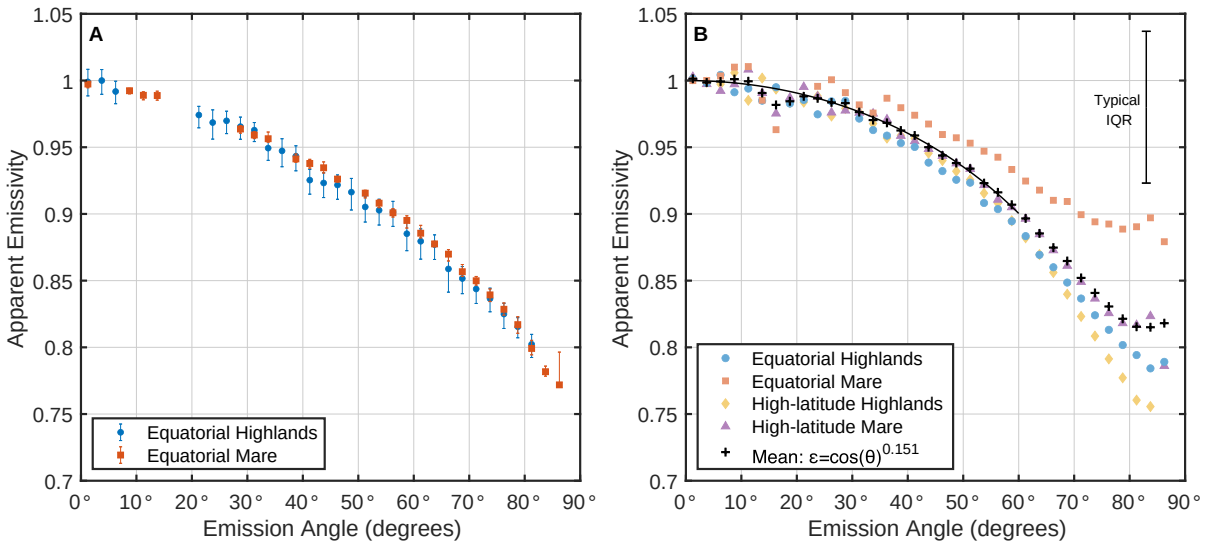

Figure 3.8: A) Median Diviner broadband apparent emissivity as a function of emission angle at noon for two equatorial targets. We constrain solar incidence angle to <2°. We assume a nadir emissivity of ∼1 at 0° emission angle. Error bars represent the interquartile range of each bin. B) Median broadband apparent emissivity around midnight (22:00-02:00 local time) for the same two equatorial targets as well as two targets at ∼50°N latitude. For clarity, the error bar in the upper-right shows the typical interquartile range. The nighttime average apparent emissivity is fit to an empirical function between 0° and 60° emission angle.

0.6°N). The solar incidence angle was constrained to <2°. Figure 3.8A shows the drop-off in apparent emissivity with emission angle relative to an assumed nadir apparent emissivity of 1. We select an emissivity of 0.8, which corresponds to the apparent emissivity of nadir illuminated lunar regolith at ∼80° emission angle as measured by Diviner.

The emission and reflectance phase functions of illuminated surfaces also depend on the solar incidence angle, so assuming a constant value of albedo and emissivity is a simplification. At high solar incidence angles, small-scale sun facing slopes will receive more illumination than slopes facing away from the sun. As a result, the apparent emissivity becomes azimuthally anisotropic, with higher and lower apparent emissivity when viewed from the sun and anti-sun directions, respectively. This effect is most important at high-latitudes, where the sun is at high solar incidence angle throughout the day. However, the approximation of a constant emissivity works fairly well for equatorial and mid-latitude locations where noon solar incidence angles are close to 0°. Further study of the emission and reflectance phase function can help to better inform future models.

The emission phase function also influences the radiances measured by Diviner. When Diviner is nadir-pointing, sloped surfaces will be viewed at emission angles equivalent to their local slope angle. Figure 3.8B shows the nighttime emission phase function (22:00-02:00 local time) for the two equatorial sites as well as a high-latitude mare (-71.52°E, 52.97°N) and a high-latitude highlands (-109.55°E, 49.55°N) location. All locations show a decrease in emissivity with emission angle. Interestingly, the nighttime emission phase function is azimuthally isotropic, indicating that it does not retain significant information about the illumination history of the surface. The equatorial mare location drops off less rapidly with emission angle than the other locations. This may be due to the higher average RA at the location, as rocks remain warmer at night and may influence the temperatures measured by Diviner when viewed off-nadir. However, these regions generally show a similar behavior. We fit the average nighttime emission phase function to an empirical function: $\varepsilon = \cos(\theta)^{0.151}$, where the apparent emissivity drops from 1 at nadir to ∼0.98 at 30° emission angle. While a small effect, this indicates that Diviner should measure slightly reduced brightness temper-

atures on steeply sloped surfaces. We include this slope-dependent nighttime emissivity in our modeled temperatures to match the brightness temperatures measured by Diviner more accurately.

3.4.4 Topographic subtraction

We use a one-dimensional finite volume model to determine the expected nighttime temperature for each point on the Moon. We use the same thermophysical and photometric properties described in Hayne et al. (2017) except for H-parameter, which we set to 5.73 cm for modeling bolometric temperature and 6.74 cm for modeling regolith temperature (figure 3.6). We create a lookup table of modeled temperature at slope-adjusted midnight for typical regolith accounting for the following parameters: latitude, slope angle and azimuth, land view factor, effective latitude of the surroundings, and sunrise and sunset times. The expected slope-adjusted midnight temperature, assuming typical regolith properties, is then determined for each spatial bin by querying this lookup table. The difference between the measured Diviner temperature and the modeled temperature is the temperature anomaly ΔT. If topography is properly accounted for, ΔT should show only the effect of thermophysical properties on nighttime temperature.

Figure 3.9 shows ΔT_{BOL} for a region at equatorial to mid-latitudes (0°-40° N) with progressively increasing levels of topographic removal: a) latitude correction, b) simple slope correction, and c) land scattering and emission correction. Most large-scale topographic features are removed by the simple slope correction, which is equivalent to the slope correction applied in the Hayne et al. (2017) global H-parameter map. However, many smaller features, most notably bowl-shaped craters, remain warmer than their surroundings. These features mostly vanish when scattering and emission is accounted for, indicating that the elevated temperature in many bowl-shaped craters is due to topographic focusing of illumination, and does not necessarily indicate a difference in thermophysical properties. For the equatorial and mid-latitudes, our model largely removes topographic effects and the remaining spatial variations in nighttime temperature mostly indicate differences in thermophysical properties.

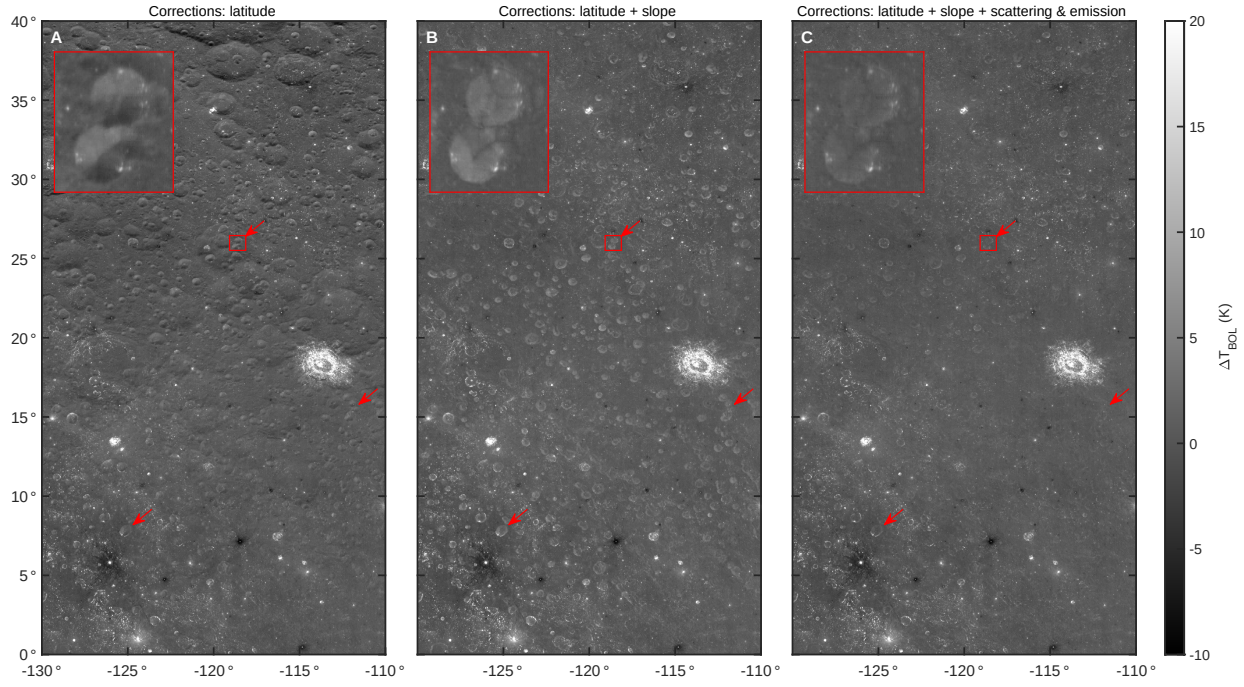

Figure 3.9: An example region showing midnight bolometric temperature anomaly with different levels of topographic removal: A) correction for latitude, but no topography correction; B) correction for latitude and slope angle, but not for scattering and emission; and C) correction for latitude, slope angle, and scattering and emission. The red arrows show examples of bowl-shaped craters which remain warmer than their surroundings when only slope and latitude are accounted for. These features mostly vanish when scattering and emission is included. The inset figure shows a close-up of the region outlined by the red box.

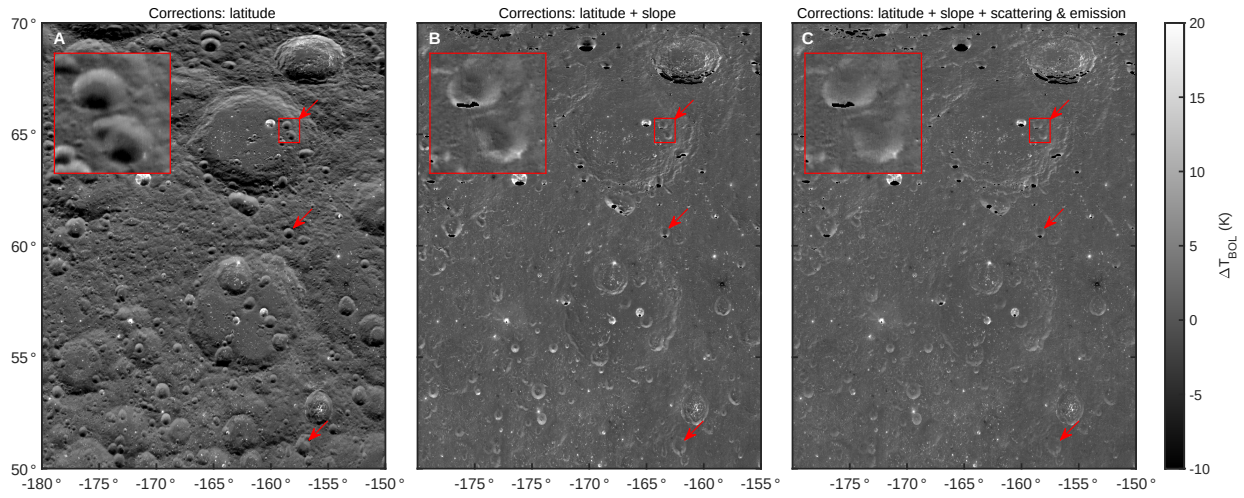

Figure 3.10: An example region showing midnight bolometric temperature anomaly with different levels of topographic removal. At high latitudes, topographic removal is less effective than at equatorial latitudes. The red arrows show several bowl-shaped craters which are partially but not completely removed when scattering and emission from surrounding topography is included. The inset figure shows a close-up of the region outlined by the red box.

Figure 3.10 shows ΔT_{BOL} for a region at high latitudes (50°-70° N). Here, topography subtraction is less effective. Many topographic features, most notably pole facing slopes, show up as warmer than their surroundings. This is likely due to complexities in the emission phase function that are not accounted for in our model. This can be addressed in future work when the emission phase function has been fully characterized. Additionally, our model simplifies the scattered and emitted radiation by assuming that the peak flux occurs at noon and does not account for the timing of illumination from different parts of the surrounding scene. Both effects likely cause errors at equatorial latitudes as well but are more pronounced at high latitudes where indirect illumination constitutes a larger fraction of the total illumination, and where high solar incidence angles lead to directionally anisotropic emission and scattering. However, even at high latitudes the model does partially correct for land emission and scattering when compared to the simple slope correction. Figure 3.10C shows less significant temperature differences due to slope than for a simple slope correction in Figure 3.10B.

3.5 Results and discussion

3.5.1 Global maps

We produce 15 maps in total, each extending to ±70° latitude and gridded at 128 ppd. These are: a) channel 6-9 brightness temperature, bolometric temperature, and regolith temperature at midnight and slope-adjusted midnight; b) derived RA at slope-adjusted midnight; and c) bolometric temperature and regolith temperature anomaly at slope-adjusted midnight. Figure 3.11 shows examples of three of these: midnight bolometric temperature, bolometric temperature anomaly, and RA. Spatial coverage for the brightness and bolometric temperature maps is nearly complete, with only ∼0.003% of spatial bins having too few observations to determine a midnight or slope-adjusted midnight temperature. Coverage is less complete for the RA, regolith temperature, and temperature anomaly maps because pole-facing slopes with effective latitudes greater than ±85° are excluded from the thermal

modeling required to produce them. This affects ∼0.16% of spatial bins, almost all at high latitudes.

Figure 3.12 shows the correlation between the new RA and temperature anomaly products with their previous versions within ±50° latitude. Temperature anomaly data is constrained to flat surfaces (slope<5°) to avoid topographic effects, which were not corrected for in the previous regolith temperature map. Rock abundance and regolith temperature closely follow a 1:1 correlation, indicating very good agreement between the new and old data products. As expected, this demonstrates that our processing method successfully reproduces the values from the previous products. Bolometric temperature is systematically greater than regolith temperature for positive temperature anomalies. This is because warm nighttime temperatures on the Moon are typically caused by rockiness. As described in section 2.5, the contribution of rocks is removed in the calculation of regolith temperature but included in the bolometric temperature, so regolith temperature is necessarily cooler than bolometric temperature. The difference between regolith and bolometric temperature becomes greater at higher temperatures because anomalously warm regions tend to have higher RA. Regolith and bolometric temperatures agree for negative temperature anomalies, indicating that most anomalously cold regions have generally low RA.

Lunar nighttime temperatures are sensitive to the thermophysical properties of the surface to a depth characterized by the thermal skin depth, $z_s \sim \sqrt{\kappa P/\pi}$ where κ is thermal diffusivity and P is the synodic rotational period of the Moon. This corresponds to ∼4-10 cm for typical regolith and ∼1 m for coherent rock. As has been noted by previous authors (Bandfield et al., 2011; Hayne et al., 2017), nighttime temperatures and derived thermophysical properties like the H-parameter on the Moon are incredibly uniform at the global scale, even across dramatically different terrain types like mare and highlands. While the mare can often be distinguished from highlands by an elevated abundance of small rocky impact craters, typical intercrater regolith in the mare and highlands have similar nighttime temperatures. This indicates that a regolith layer with a thickness at least a few times the thermal skin depth has developed across most of the Moon from billions of years of impact

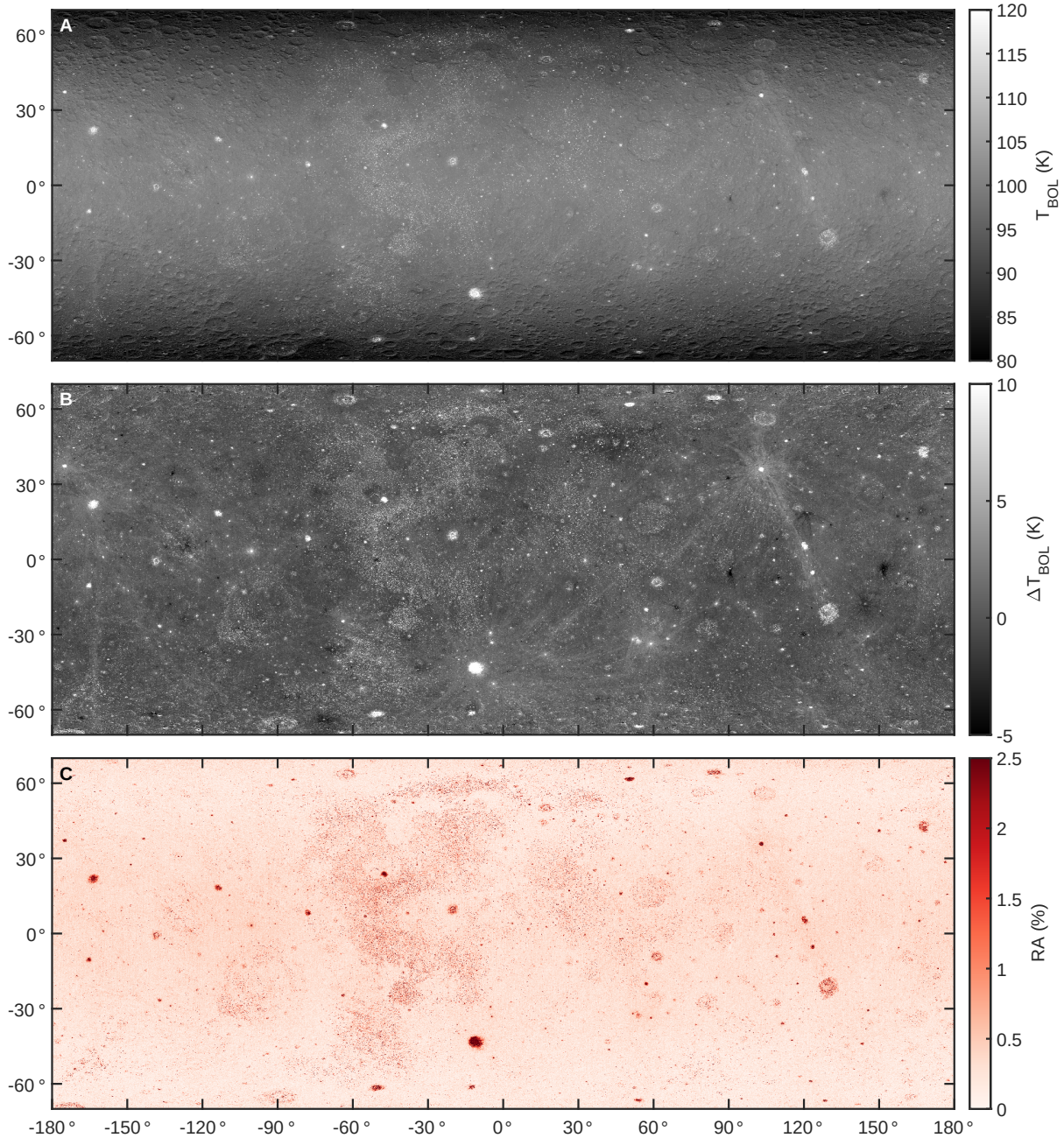

Figure 3.11: Global maps of A) bolometric temperature at midnight, (B) bolometric temperature anomaly at slope-adjusted midnight, and C) rock abundance at slope-adjusted midnight.

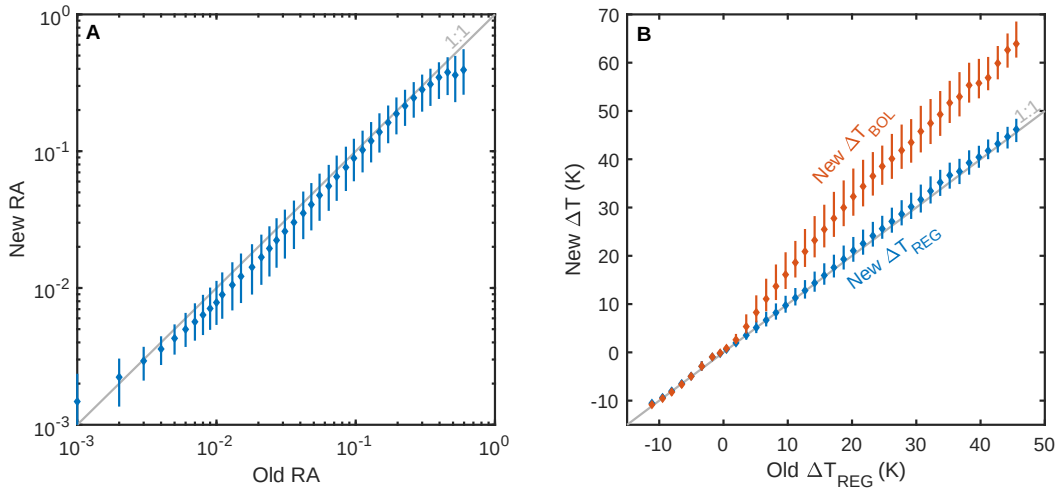

Figure 3.12: Cross plots comparing the new and old A) rock abundance (RA) and B) temperature anomaly products within ±50° latitude. Temperature anomaly data is constrained to flat surface (slope<5°). Data points show binned medians with error bars indicating the interquartile range. The new and old RA and regolith temperatures are in very close agreement globally. Bolometric temperature is greater than regolith temperature for positive temperature anomalies.

bombardment. The increased abundance of rocky craters in the mare is evidence that the regolith layer is thinner in the mare than in the highlands, as more frequent small impacts are able to penetrate the regolith to excavate underlying rocks (Elder et al., 2019).

3.5.2 Examples of map improvements

The primary improvements to the new Diviner maps are an increase in effective resolution due to better data georeferencing and the removal of topographic effects. These effects allow for the identification of smaller and fainter thermal features, which is best demonstrated by looking at smaller-scale example regions.

Figure 3.13 compares the old regolith temperature anomaly map and the new bolometric temperature anomaly map for Taurus-Littrow valley, the landing site of the Apollo 17 mission (30.77°E, 20.19°N). This example highlights that the improved georeferencing in the new maps allows smaller rocky craters to be identified than was previously possible. For example, a cluster of ∼400-600 m diameter rocky craters to the south of the Apollo 17 Lunar Module (LM) appears as an unresolved region of increased nighttime temperature in the old map. In the new map, each crater is individually resolved, and differences in their thermophysical properties are perceptible. In addition, several smaller ∼200 m diameter rocky craters throughout the region do not appear in the old map but are identifiable in the new map (indicated by the red arrows in figure 3.13). One advantage of this improvement is that nighttime temperatures measured by Diviner can be better correlated with other high resolution data sets or with surface measurements in the case of landed missions.

Large rocky impact craters are among the most prominent features in the Diviner nighttime data set. Figure 3.14 shows Tsiolkovskiy crater (180 km, 129.2°E, -20.4°N), which has an anomalously high RA for a crater of its age (>3.2 Ga) (Williams et al., 2013; Pasckert et al., 2015). This can be attributed to a large impact melt deposit to the southeast of the crater (Greenhagen et al., 2016). The melt deposit is more prominent and thermally distinct from the surrounding regolith in the new nighttime temperature map. This is mostly due to

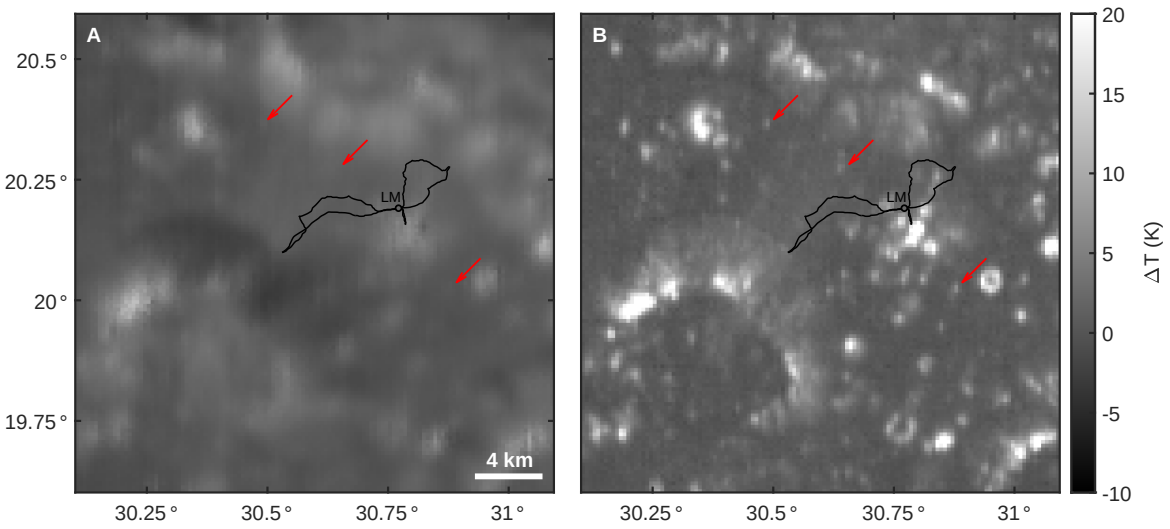

Figure 3.13: Comparison of A) the previously published regolith temperature map and B) the updated bolometric temperature anomaly map at Taurus-Littrow valley, the Apollo 17 landing site. In the previous product, a cluster of rocky craters to the south of the Apollo 17 Lunar Module (LM) appears as an unresolved region of increased nighttime temperature. In the new product, individual craters can be resolved. The red arrows show the locations of several ∼200 m diameter rocky craters that do not appear in the old regolith temperature map but are identifiable in the new bolometric temperature map.

the improved topographic correction, as the slight increase in temperature associated with the impact melt was previously difficult to distinguish above topographic variations in temperature. The sharp, well-defined boundary between impact melt and background regolith apparent in the new maps indicates that the melt deposit is well preserved, despite its old age.

Lunar cold spots are extensive ray-like regions of reduced nighttime temperature associated with very young impact craters (Bandfield et al., 2011; Williams et al., 2018a). Bandfield et al. (2014) proposed that these features can be explained by a fluffing-up of the upper centimeters of regolith out to great distances (∼10-100 crater radii), resulting in a low thermal inertia layer. Figure 3.15 shows an example of a prominent cold spot around a ∼600 m diameter crater (-131.71°E, 34.21°N). The cold spot structure has significantly more detail in the new maps, displaying a distinctive sinuous ray system. Like optical crater rays, individual cold spot rays appear to be made up of chains of smaller low thermal inertia streaks. These rays are sometimes discontinuous. For example, faint traces of a cold spot ray can be identified at distances of ∼60 km or ∼200 crater radii away, which was not observed in the previous map. This indicates that cold spots have a more detailed structure and extend to greater distances from their source crater than was previously known.

Figure 3.15 also shows a smaller cold spot around a ∼150 m crater (-131.30°E, 36.38°N). The central crater and its nearby ejecta now appear as a warm feature ∼1-2 pixel across. Previously this was not observed, likely due to blurring of the warm rocky crater with the surrounding cold spot.

3.5.3 Validating rock abundance with manual boulder counts

A key advantage of the improvement in effective spatial resolution is that the new Diviner maps are better spatially correlated with high-resolution images. To demonstrate this, we compare the Diviner derived RA with the number of boulders visible in LROC imagery for a ∼4.2 by ∼2.9 km region roughly centered on the Apollo 17 LM (figure 3.16). This region has

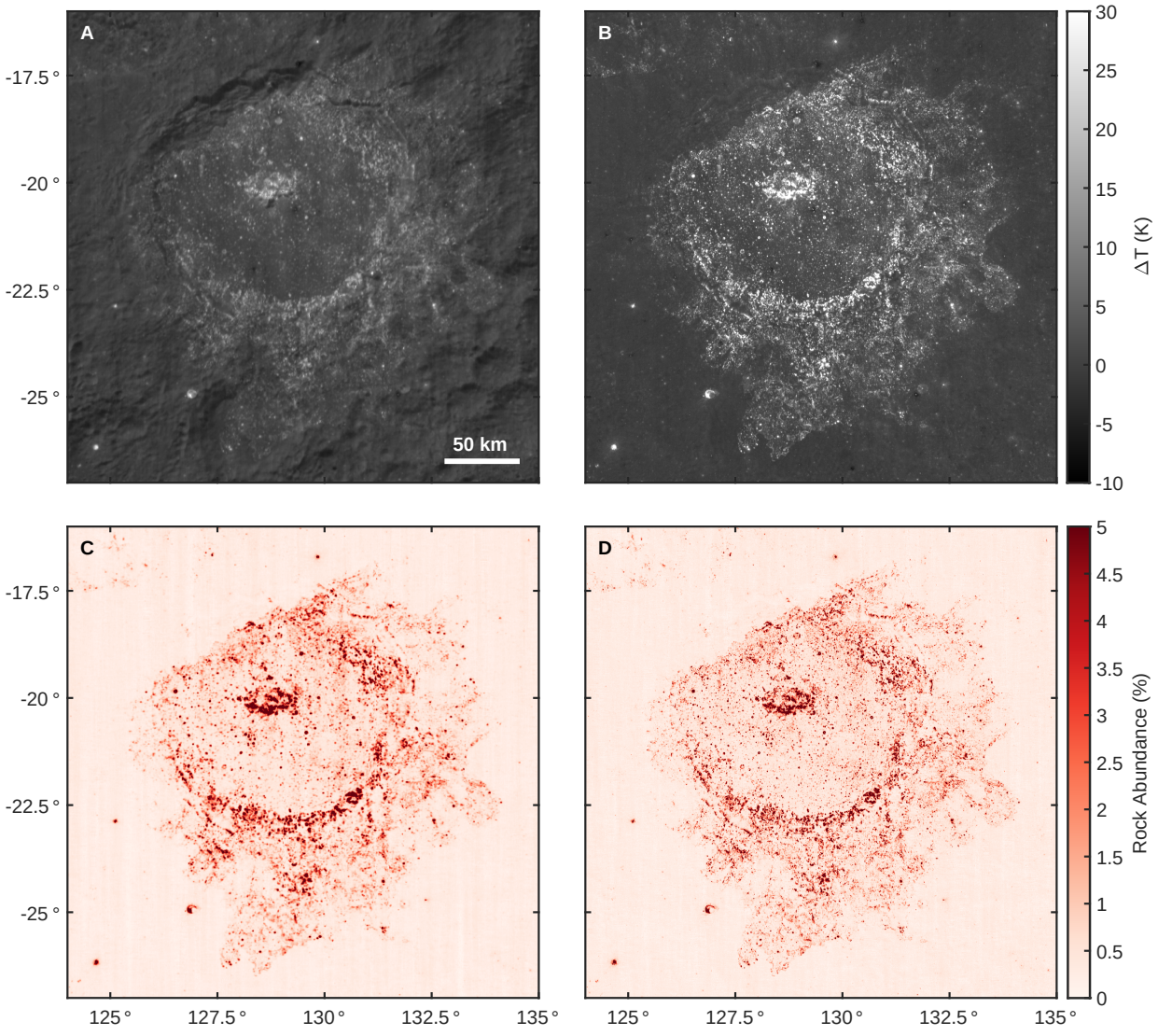

Figure 3.14: Comparison of the previously published A) nighttime regolith temperature and C) rock abundance (RA) maps with the new B) bolometric temperature anomaly and D) RA maps for the Tsiolkovskiy crater (129.2°E, -20.4°N). Topographic removal allows the boundary of the melt deposit to be clearly defined.

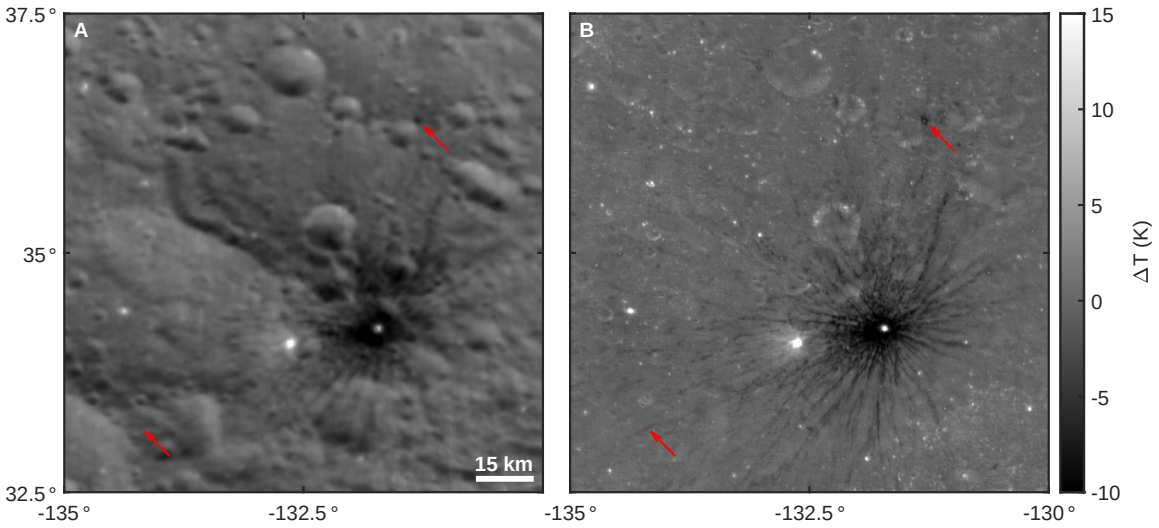

Figure 3.15: Comparison of the A) previously published nighttime regolith temperature map with the B) new bolometric temperature anomaly map for a lunar cold spot. Topographic removal and improved sharpness allow the detailed sinuous structure of the cold spot to be visible at significantly greater distance. The left red arrow shows a faint cold spot ray streak not apparent in the previous map. The top red arrow shows a small cold spot whose ∼150 m diameter central crater is apparent as warm feature ∼1-2 pixels across in the new map.

four craters with notable RA signatures: Camelot crater (30.731°E, 20.195°N, 625 m), Powell crater (30.763°E, 20.160°N, 412 m), Sherlock crater (30.813°E, 20.184°N, 503 m), and Steno-Apollo crater (30.794°E, 20.145°N, 520 m). Of these, Diviner measures the highest RA for Steno-Apollo crater (∼0.074), an intermediate RA for Powell and Sherlock craters (∼0.034), and a comparatively low RA for Camelot crater (∼0.014) (figure 3.16C). We manually count boulders in this region using the Apollo 17 LROC NAC Orthomosaic (Haase et al., 2019) and several additional NAC images (M113751661L, M129086118L, M129086118R, 162107606L, M165645700L, M165645700R, and M172717297R) which were selected to have resolutions of ∼0.5 m/pixel and to cover a range of illumination geometries. The count region extends one 128 ppd spatial bin beyond the pictured count region. This is necessary for comparison to the RA maps because the spatial response of a Diviner spatial bin extends slightly beyond the target bin (figure 3.2F). In total, we identified ∼30,000 boulders in the count region.

Figure 3.17 shows the cumulative size-frequency distribution (SFD) of the boulder survey. We find that the boulder SFD can be described with a power-law:

$$N = CD^{-b} \tag{3.6}$$

where N is the cumulative number of boulders larger than diameter D, C is a coefficient describing the number of boulders of a particular size, and b is the power-law slope which controls the ratio of small boulders to large boulders. For boulders larger than ∼2 m in diameter, the survey SFD has a power-law slope of about -5 to -6. Figure 3.17 also shows the SFD of boulders located within 1.25 crater radii of the four rocky craters of interest. The boulder power-law slopes for each crater are also generally within the range of -5 to -6. Though, interestingly, the boulder SFD for Sherlock crater appears to have a shallower slope (b ∼ 4) for boulders larger than ∼3 m while maintaining a steeper slope (b ∼ 5-6) for smaller boulders. These values generally agree with Watkins et al. (2019), who performed a survey of boulders on the ejecta blankets of several rocky craters (200-950 m) and found power-law slopes ranging from 4.4 to 6.8. For each SFD in figure 3.17, the power-law behavior does not continue for boulders smaller than ∼2 m. This roll-off is due to the resolution limit of NAC images, where boulders smaller than ∼4 pixels across (2 m at 0.5 m/pixel) are difficult to

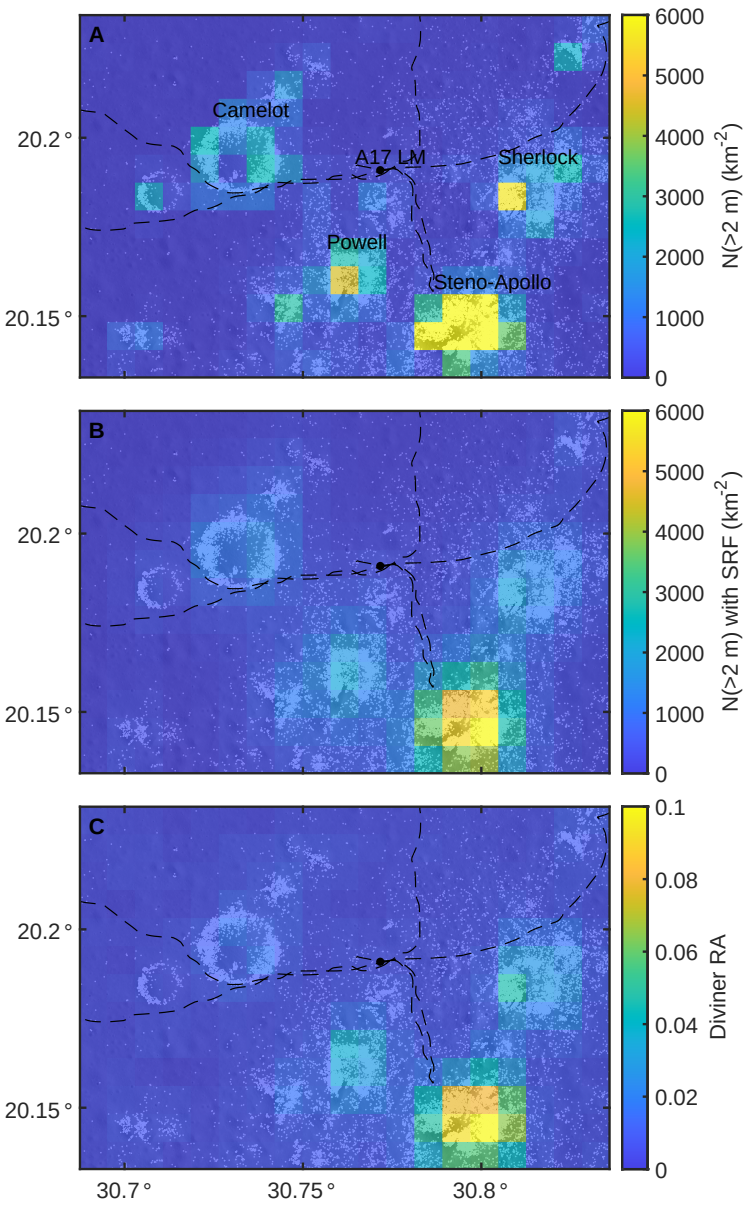

Figure 3.16: Comparison between manual boulder counts and Diviner rock abundance in the Apollo 17 landing site region: A) The spatial density of counted >2 m boulders binned at 128 ppd; B) The spatial density of >2 m boulders accounting for the spatial response function (SRF) of a 128 ppd spatial bin (section 2.3); and C) Diviner derived rock abundance. The white points show boulders >1 m in diameter.

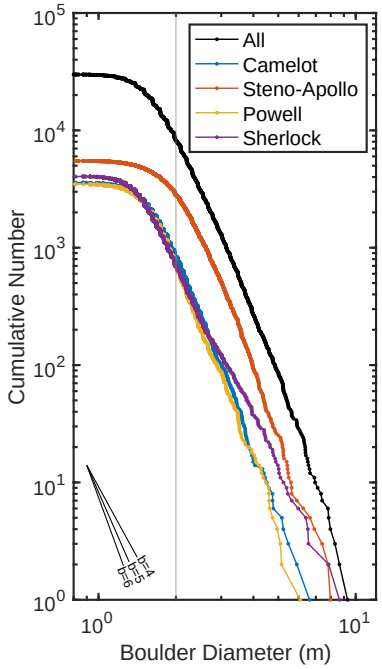

Figure 3.17: Cumulative size-frequency distribution (SFD) for a survey of boulders in the Apollo 17 landing site region. The colored lines show the boulder SFD within 1.25 crater radii of four rocky craters. Each SFD has a power-law slope of ∼5-6.

identify. We assume that our survey is mostly complete for boulder >2 m.

Figure 3.16A shows the spatial density of >2 m boulders gridded at 128 ppd. There is relatively good spatial correlation between the boulder spatial density map and the Diviner RA map (figure 3.16C). The spatial bins with highest boulder density, associated with Steno-Apollo crater, also have the highest Diviner RA. However, there are also some dissimilarities, mostly at the boundaries of rocky features. For example, several of the spatial bins surrounding Steno-Apollo crater have moderate RA measured by Diviner but very few counted boulders. These discrepancies likely arise because the RA of a Diviner spatial bin is also partially sensitive to boulders in neighboring spatial bins as discussed in section 2.3. Figure 3.2F shows that the SRF for a spatial bin is most strongly influenced by the properties within that bin, but also includes some contribution from neighboring regions, mostly to the north and south. Therefore, the RA measured by Diviner for a particular spatial bin

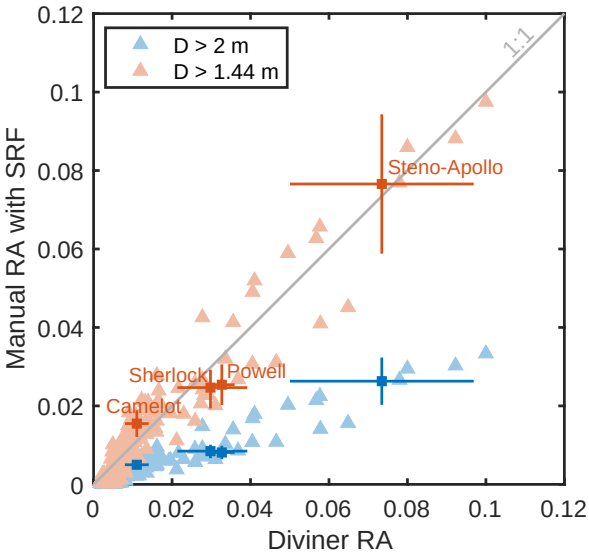

Figure 3.18: Comparison between the Diviner derived rock abundance (RA) and the manual RA calculated from boulder counts, after the spatial response function is accounted for. Diviner RA best agrees with the inferred areal fraction of $>\sim$1.44 m boulders.

represents the properties of a region which is slightly larger than a single 128 ppd spatial bin. To properly compare the Diviner RA map with our manual boulder counts, we convolve the spatial density of counted boulders using the SRF for a 128 ppd spatial bin at 20°N latitude. The resulting map (figure 3.16B) appears very similar to the Diviner derived RA map (figure 3.16C), where spatial bins bordering rocky regions inherit some boulder density from neighboring bins.

Rock abundance represents the areal fraction of the surface covered by rocks. Therefore, we can convert boulder spatial density to a "manual RA" by summing the cross-sectional area of each rock within a spatial bin's SRF and dividing by the total area (weighted by the SRF). The blue points in figure 3.18 show that there is a strong roughly linear correlation between the Diviner derived RA and the areal rock fraction of boulders >2 m in diameter. However, the coverage of >2 m boulders is systematically lower than the Diviner RA. This indicates that Diviner is sensitive to rocks smaller than 2 m, which were not reliably counted

in the boulder survey because of the resolution limit of NAC images. To extend our boulder counts to smaller sizes, we extrapolate the rock counts within each spatial bin according to a power-law with a slope of -5.5, a value appropriate for the overall SFD slope in this region. We achieve the best agreement between Diviner RA and the manual RA when extrapolating to boulders larger than ∼1.44 m in diameter (figure 3.18). This value may be slightly influenced by uncertainties in boulder counting, which may affect both the number of rocks identified and the diameters assigned to each boulder. For a ±20% error in the number and diameter of counted boulders, the best fit rock size remains between ∼1-2 m. This agrees with Bandfield et al. (2011), who estimated that the Diviner RA map should be sensitive to rocks sufficiently larger than the thermal skin depth for rock which is ∼1 m. Rocks smaller than this experience lateral cooling from the surrounding regolith and retain less heat than larger rocks because of their lower mass, resulting in lower nighttime temperatures.

This example demonstrates that the improvements made to the georeferencing of Diviner data allow for excellent spatial correlation with high-resolution data sets, in this case LROC NAC images. The value for a particular spatial bin is influenced by the properties of a region slightly larger than that spatial bin, however this effect does not typically extend more than ∼1 spatial bin away at equatorial and mid latitudes.

3.6 Conclusions

Using ∼13 years of Diviner data, we produce updated nighttime temperature and RA maps of the Moon. In addition to greater data volume, several improvements are implemented that result in significantly sharper maps. Errors in the Diviner instrument's pointing are corrected, resulting in better georeferencing of Diviner observations. Additionally, past EFOV modeling has been optimized to improve data georeferencing without spatial interpolation. We estimate that these improvements result in an increase in the effective resolution of Diviner maps of ∼3.5× longitudinally and ∼1.3× latitudinally. Additionally, we develop a thermal model which accounts for topographic scattering and emission to remove the effect

of topography on nighttime temperatures. Indirect illumination scattered and emitted from surrounding topography can have a significant effect on nighttime temperatures for regions which have a high percentage of land in their line of sight. By subtracting the effect of topography on nighttime temperature, we produce temperature anomaly maps that better isolate differences in thermophysical properties.

The improvement in map sharpness allows the lunar thermal environment to be studied at a finer scale than was previously possible, and topographic removal reveals faint thermal features which were previously hidden by topographic effects. We show that the elevated nighttime temperatures observed in many bowl-shaped craters can be explained by topographic scattering and emission, and does not necessarily indicate a difference in thermophysical properties. The uniformity of intercrater terrain nighttime temperatures suggests a globally ubiquitous regolith layer with a thickness that extends to at least a few diurnal skin depths regardless of surface age. We also find that the impact melt deposit around Tsiolkovskiy crater is sharper and better defined than was previously shown, in spite of its old age. Lunar cold spots have more detailed structure and extend to greater distances from their source craters than was previously known.

The improved effective resolution of Diviner maps enables better spatial correlation with other high-resolution data sets. To demonstrate this, we counted >30,000 boulders larger than $\sim$ 1 m in a region near the Apollo 17 landing site using LROC imagery. Diviner derived RA strongly correlates with rock counts after accounting for the SRF of a gridded spatial bin, which can extend slightly beyond a single 128 ppd spatial bin. Diviner RA best agrees with the inferred areal coverage of rocks larger than $\sim$1-2 m in diameter. Rocks are no longer distinguishable in Diviner RA below this threshold, thereby defining the size of a thermally distinct rock.

Acknowledgments

The authors thank and acknowledge Joshua Bandfield, whose body of work with Diviner formed the foundation of this study. We also thank UCLA summer interns Danielle Shields and Zane Neelin for their contribution characterizing the Diviner pointing offsets, and Emerson Speyerer and an anonymous reviewer for their valuable feedback during the review process. This study was supported by the NASA Lunar Reconnaissance Orbiter project.

Data availability statement

The Diviner RDR data used in this study are publicly available at the Geosciences Node of the Planetary Data System (PDS) (http://pds-geosciences.wustl.edu/missions/lro/diviner.htm) (Paige et al., 2022). The 128 ppd gridded global maps generated in this study are available at the Diviner Dataverse repository at UCLA (https://doi.org/10.25346/S6/LFAVXU) (Powell, 2022). The updated maps will also be made available on the Geosciences Node of the PDS.

CHAPTER 4

Discovery of a lunar cold spot at Apollo 16's South Ray crater

This chapter is in-prep for submission as: Powell, T.M., Williams, J.-P., Greenhagen, B.T., Hayne, P.O., Elder, C.M., and Paige, D.A. (2023). Discovery of a lunar cold spot at Apollo 16's South Ray crater.

Abstract

Lunar cold spots are extensive, ray-like regions of reduced nighttime temperature surrounding very young impact craters. Using improved Diviner nighttime temperature maps, we discover a faint cold spot around South Ray crater at the Apollo 16 landing site. South Ray crater's $\sim$2.08$\pm$0.17 Ma age is consistent with the fading behavior of other large cold spots, making South Ray crater the oldest known cold spot crater. During the Apollo missions, astronaut footprint depths were used to estimate the relative density of the upper $\sim$15 cm of regolith. The relative density at the Apollo 16 landing site is statistically lower than at the other Apollo sites. This agrees with thermal modeling, which requires a lower average density within the upper several centimeters to explain the reduced nighttime temperatures. These results provide both in-situ and orbital evidence that the low thermal inertia of cold spots is caused by a decompaction of the upper centimeters of regolith. Further study of Apollo 16 soils and observations may help to better constrain the properties of cold spots, which will inform our understanding of their formation mechanism and their impact on regolith evolution globally.

4.1 Introduction

Surface temperature mapping of the Moon by the Diviner instrument on the Lunar Reconnaissance Orbiter (LRO) (Paige et al., 2010a) has revealed extensive regions of anomalously low nighttime temperature surrounding fresh impact craters. Termed "cold spots", these features are ∼1-10 K cooler than their surroundings at night, are ray-like in appearance, and typically extend to ∼10-100 crater radii (Bandfield et al., 2014). Cold spot craters are among the youngest known population of impact craters with a global size-frequency distribution (SFD) consistent with an age of ∼150 ka and the largest cold spots fading on timescales of ∼1 Ma (Williams et al., 2018a). Some examples of unusually cold regions were originally noted in data from the Infrared Scanning Radiometer on-board the Apollo 17 Command-Service Model (Mendell and Low, 1974, 1975), however there was insufficient high-resolution data at the time to tie these features to impact craters or to distinguish the ray-like structure of cold spots.

Bandfield et al. (2014) proposed that cold spots could be explained by a decompaction of the upper several centimeters of regolith, resulting in a lower thermal inertia surface layer. Given the size of the cold spots relative to their source craters, the total amount of material necessary to explain the magnitude of cooling is greater than volume excavated by the parent crater, suggesting that cold spots cannot be explained by the emplacement of primary ejecta alone but rather a "fluffing-up" of in-situ material (Bandfield et al., 2014), This is supported by imagery, as cold spots are visually indistinct under most illumination conditions and do not show evidence for significant deposits of optically fresh material. While their mechanism of formation has not been definitively established, cold spots represent a newly identified cratering process which causes modification of the surface to great distances.

South Ray crater (-9.149° N, 15.382° E) is a ∼700 m diameter crater in the Descartes Highlands (Hodges et al., 1973; Ulrich et al., 1975) in close proximity to the Apollo 16 landing site. Based on cosmic ray exposure dating, South Ray crater has an estimated age of 2.08±0.17 Ma (Drozd et al., 1974; Arvidson et al., 1975; Eugster, 1999). This age is

only slightly older than the oldest known cold spot (Williams et al., 2018a), making South Ray crater a cold spot candidate. Recently published nighttime temperature maps with improved resolution and the effects of topography removed (Powell et al., 2023) reveal a region of slightly reduced nighttime temperature surrounding South Ray crater which we interpret to be a cold spot (figure 4.1A). This has implications for the geologic context of the Apollo 16 mission and allows us to retrospectively analyze in-situ measurements to study cold spot properties. In this work, we: 1) investigate the thermophysical properties of South Ray crater's cold spot in comparison to other similarly sized cold spots; and 2) re-examine Apollo era regolith density estimates derived from astronaut footprint depths to understand the properties of cold spots.

4.2 Data and methods

4.2.1 Diviner data and thermal model

The Diviner Lunar Radiometer Experiment on LRO is an infrared radiometer that has been mapping lunar surface temperatures since 2009 (Paige et al., 2010a). Diviner has 9 spectral channels, including 7 thermal infrared channels that span the wavelength range from 8 to 400 μm and are sensitive across the broad range of lunar surface temperatures. We collected all Diviner Reduced Data Records (RDRs) for channel 6–9 available through July 2022 for a $\sim 3^\circ \times 3^\circ$ region centered on South Ray crater. Powell et al. (2023) published global midnight bolometric temperature, T_{BOL}, maps which have better effective spatial resolution than previously published maps due to a correction for Diviner pointing errors. Additionally, they implement a model which mostly removes the effect of topography on nighttime temperature by accounting for the effect of latitude, local slope, and scattering and emission from surrounding topography. The resulting bolometric temperature anomaly, ΔT_{BOL}, maps allow faint thermal features which were previously masked by topography to be more noticeable. Following the approach described in Powell et al. (2023), we produce T_{BOL} and ΔT_{BOL} maps for the Apollo 16 region gridded at 128 pixels-per-degree (ppd) and

in 0.25 lunar hour timesteps.

Nighttime surface temperatures on the Moon are indicative of the thermophysical properties within a few multiples of the thermal skin depth (∼4-10 cm for regolith), and are generally affected by the material properties at greater depth later in the night. Experiments show that the thermal conductivity and volumetric heat capacity of regolith and other granular materials are strongly influenced by their bulk density (Fountain and West, 1970; Hemingway et al., 1981). The temperatures observed by Diviner for typical regolith predict a thin layer of loose, low-density regolith overlying more compacted regolith (Vasavada et al., 2012; Hayne et al., 2017), consistent with Apollo drill core measurements (Carrier III et al., 1991). We use a 1-dimensional thermal model based on Hayne et al. (2017) which models the vertical structure of the regolith as an exponential increase in density, ρ, with depth, z:

$$\rho = \rho_d - (\rho_d - \rho_s)e^{-z/H} \tag{4.1}$$

where ρ_s and ρ_d are the regolith densities at the surface and at depth respectively, and H is an exponential scale height describing the thickness of the loosely-packed surface regolith layer.

4.2.2 Relative density from astronaut footprints

Several investigations of soil mechanics were performed during the Apollo program (Mitchell et al., 1974). These included: 1) core tubes and drill cores which sampled to depths of ∼60 cm to ∼3 m; 2) penetration resistance tests which probed the upper ∼60 cm; and 3) test of soil compaction by astronaut footprints and vehicle tracks, which probe the upper ∼15 cm. The astronaut footprint results are the most relevant for investigating cold spots because they probe to a depth similar to what is sensed by nighttime temperatures. Namiq (1970) used laboratory experiments of footprints in regolith simulant and finite element stress-deformation modeling to develop a scaling between footprint depth and the porosity of the upper ∼15 cm of regolith. Mitchell et al. (1974) used 776 footprint images across all the Apollo sites to estimate the porosities for typical intercrater regolith at each site.

In addition, Mitchell et al. (1972) presents a breakdown of the average regolith porosity at several research station locations along the Apollo 16 Extravehicular Activity (EVA) traverses.

These studies typically reported their results as porosities. However, the conversion between footprint depth and porosity depends on the maximum and minimum packing density of the material, which varies with the regolith grain size distribution, shape, and orientation. Later work showed that the maximum and minimum packing densities for returned regolith samples and lunar simulant were substantially different (Carrier III et al., 1973). As a result, subsequent studies report the results of the footprint analysis in terms of "relative density," D_r (Carrier III et al., 1991), a measure of compactness where 0% and 100% correspond to the minimum and maximum naturally achievable packing density of regolith, respectively (ρ_{min} and ρ_{max}):

$$D_r = \frac{\rho_{max}}{\rho} \frac{(\rho - \rho_{min})}{(\rho_{max} - \rho_{min})} \times 100\% \tag{4.2}$$

We follow this prescription and convert the mean and standard deviation porosity values reported in Mitchell et al. (1972) and Mitchell et al. (1974) to relative densities assuming porosity is normally distributed. For each location, the standard deviation and number of samples were used to calculate standard error of the mean.

4.3 Results

4.3.1 Cold spot thermophysical properties

Figure 4.1A shows a distinct -1 to -2 K temperature anomaly with ray-like structure surrounding South Ray crater, which we interpret to be a cold spot (herein referred to as South Ray cold spot). The low temperature 'rays' of South Ray cold spot match the orientation of optical rays apparent in LRO Camera (LROC) Narrow Angle Camera (NAC) imagery. The continuous portion of the cold spot extends to ∼10-20 crater radii, with individual low temperature rays extending ∼30-40 crater radii. South Ray cold spot is notably fainter and

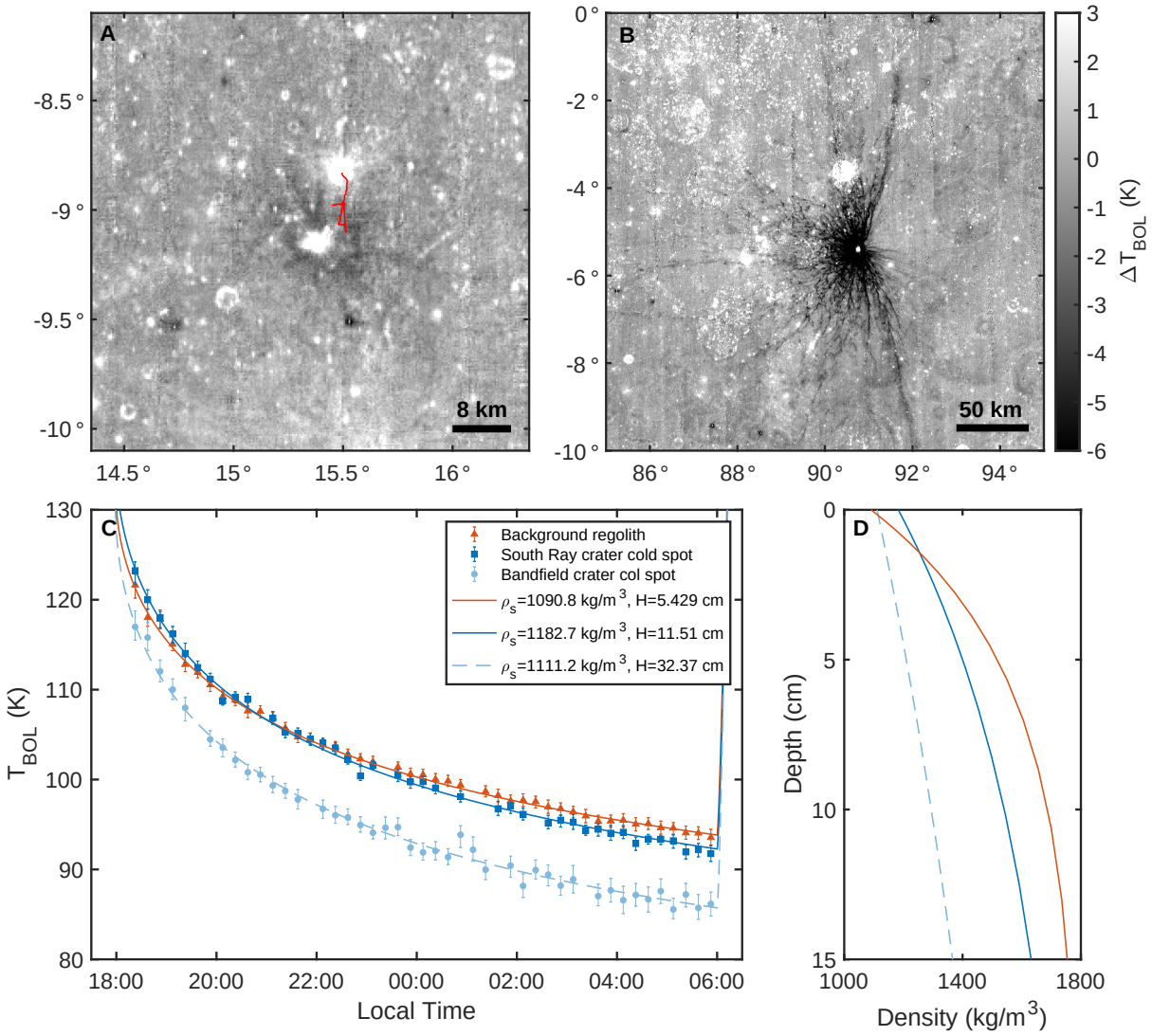

Figure 4.1: A) ΔT_{BOL} at 04:00 for South Ray cold spot. Red line shows the Apollo 16 EVA traverses. B) ΔT_{BOL} at 04:00 for Bandfield cold spot. C) Median and interquartile range T_{BOL} throughout the night for South Ray cold spot, Bandfield cold spot, and typical regolith near South Ray cold spot. The cooling curves were fit using a thermal model. D) Density profile of thermal model fits.

smaller than other cold spots around similarly sized craters. For example, figure 4.1B shows the cold spot associated with Bandfield crater (90.76°E, -5.39°N, 898 m) (herein referred to as Bandfield cold spot) which is one of the most prominent cold spots on the Moon and is also significantly younger than South Ray cold spot at 0.23±0.02 Ma (Williams et al., 2018a). Bandfield cold spot has a continuous region which extends to ∼35 crater radii, within which nighttime temperatures are ∼8-10 K cooler than the surrounding regolith. Discontinuous cold spot rays extend to over 200 crater radii, significantly farther than the greatest extent of the South Ray cold spot.

The thermophysical properties of both cold spots can be inferred from their nighttime cooling behavior, shown in figure 4.1C. Each curve is fit using a 1-D thermal model (Hayne et al., 2017) where ρ_s and H are allowed to vary. The best fit values for typical regolith (ρ_s=1090 kg/m^3 and H=5.43 cm) agree well with previous studies (Bandfield et al., 2014; Hayne et al., 2017; Powell et al., 2023). Bandfield cold spot exhibits temperatures ∼8-10 K lower than typical regolith and is clearly distinct from the surrounding regolith almost immediately after sunset. This is best fit with a typical value for surface density and an H significantly greater than background (ρ_s=1110 kg/m^3 and H=32.4 cm), resulting in a lower average density over the upper centimeters of regolith (figure 4.1D).

South Ray cold spot is ∼1-2 K cooler than typical regolith at its most prominent late in the night. However, it has similar or slightly higher temperatures early in the night and does not become distinct from its surroundings until ∼22:00 local time. Because nighttime temperatures are typically affected by material at greater depth later in the night, this suggests that the near-surface thermal inertia is similar to or greater than that of typical regolith, while the thermal inertia probed throughout the entire night, indicative of the properties of the upper several centimeters, is lower than that of typical regolith. As a result, the best fit model for South Ray suggests a vertical layering where the near surface has typical or greater density, and the subsurface has lower density when compared to typical regolith at the same depth (ρ_s=1183 kg/m^3 and H=11.5 cm).

We use the best fit density profiles to estimate the average density within the upper 15

cm. We find that South Ray cold spot has an average density of ∼1455 kg/m^3, slightly lower than typical regolith (∼1558 kg/m^3). Bandfield cold spot requires a much lower density of ∼1249 kg/m^3. An important caveat is that lunar surface temperatures, while sensitive to the properties within the upper tens of centimeters, are most sensitive to the thermophysical properties near the surface and progressively less sensitive to the properties at depth. Properties below ∼10 cm depth have a minimal influence on surface temperatures, so the average densities we derive for the upper ∼15 cm rely on extrapolation. Additionally, we use a relatively simple model for the subsurface regolith structure, and it is plausible that different or more complex density profiles may yield similar surface temperature trends. However, the inferred density values can be used to reveal relative differences in subsurface density between regions.

4.3.2 Correlation with other cold spots

South Ray cold spot's comparatively smaller size and faint temperature anomaly can likely be explained by fading. We test this hypothesis by comparing the properties of South Ray cold spot to the properties of other cold spots with age estimates. Williams et al. (2018a) dated several large (>800 m) cold spots by counting smaller craters superposed on their continuous ejecta and found ages ranging from ∼220 ka to ∼1.3 Ma. South Ray crater is estimated to be ∼2.08±0.17 Ma (Drozd et al., 1974; Arvidson et al., 1975; Eugster, 1999). Figure 4.2A shows the radially binned median ΔT_{BOL} (Powell et al., 2023) with distance for 3 example cold spots including South Ray cold spot. ΔT_{BOL} typically peaks at around ∼10-20 crater radii and drops off gradually with distance until reaching background levels at ∼30-100 crater radii.

We characterize the strength of each cold spot as the peak value of their radially binned ΔT_{BOL} (table 4.1). Figure 4.2B shows that there is a strong correlation between peak ΔT_{BOL} and age, with the most prominent cold spots being younger than ∼500 ka. We find that the trend for the Williams et al. (2018a) cold spots can be fit using a power-law. South Ray cold spot falls along the trailing end of the best fit power-law, indicating that South Ray cold

Table 4.1: Summary of large cold spot properties. The ages for cold spots 1-15 were determined by crater counting (Williams et al., 2018a), and the age of South Ray cold spot was determined from cosmic ray exposure ages (Eugster, 1999).

Index	Longitude (degrees)	Latitude (degrees)	Diameter (km)	Age (Ma)	-ΔT (K)	Extent (crater radii)
1	144.406	-17.680	2.315	0.99±0.04	1.97(1.39-2.45)	138(124-149)
2	151.681	-4.079	1.753	0.22±0.01	5.06(4.35-5.73)	126(112-137)
3	121.306	18.685	2.112	0.42±0.07	2.61(2.00-3.06)	103(92-121)
4	109.907	-6.737	1.143	0.48±0.03	2.88(2.24-3.53)	64(56-70)
5[a]	90.764	-5.394	0.898	0.23±0.02	8.60(7.10-9.58)	123(109-127)
6	120.117	-29.732	1.051	0.38±0.04	4.51(4.01-4.97)	65(59-74)
7	136.799	-42.158	0.886	0.77±0.06	2.42(1.96-2.94)	53(49-58)
8	-126.006	5.823	1.085	0.42±0.07	4.28(3.61-4.76)	76(71-77)
9	69.143	-18.925	1.140	0.27±0.02	3.45(2.58-4.00)	74(71-76)
10	166.633	19.381	1.714	1.10±0.01	1.8(1.18-2.35)	70(63-77)
11	-126.636	-23.598	1.739	0.81±0.08	1.5(1.02-1.90)	75(73-85)
12	-120.369	-36.750	1.538	1.20±0.05	1.32(0.71-1.82)	56(53-59)
13	-68.071	-35.889	1.750	0.58±0.04	2.26(1.70-2.71)	82(77-89)
14	-33.810	-43.618	1.277	0.62±0.04	1.86(1.21-2.41)	75(67-90)
15	80.732	-21.088	1.670	1.30±0.02	1.36(0.82-1.81)	44(40-45)
16[b]	15.382	-9.149	0.710	2.08±0.17	1.01(0.41-1.35)	21(18-28)

[a]Bandfield crater, [b]South Ray crater

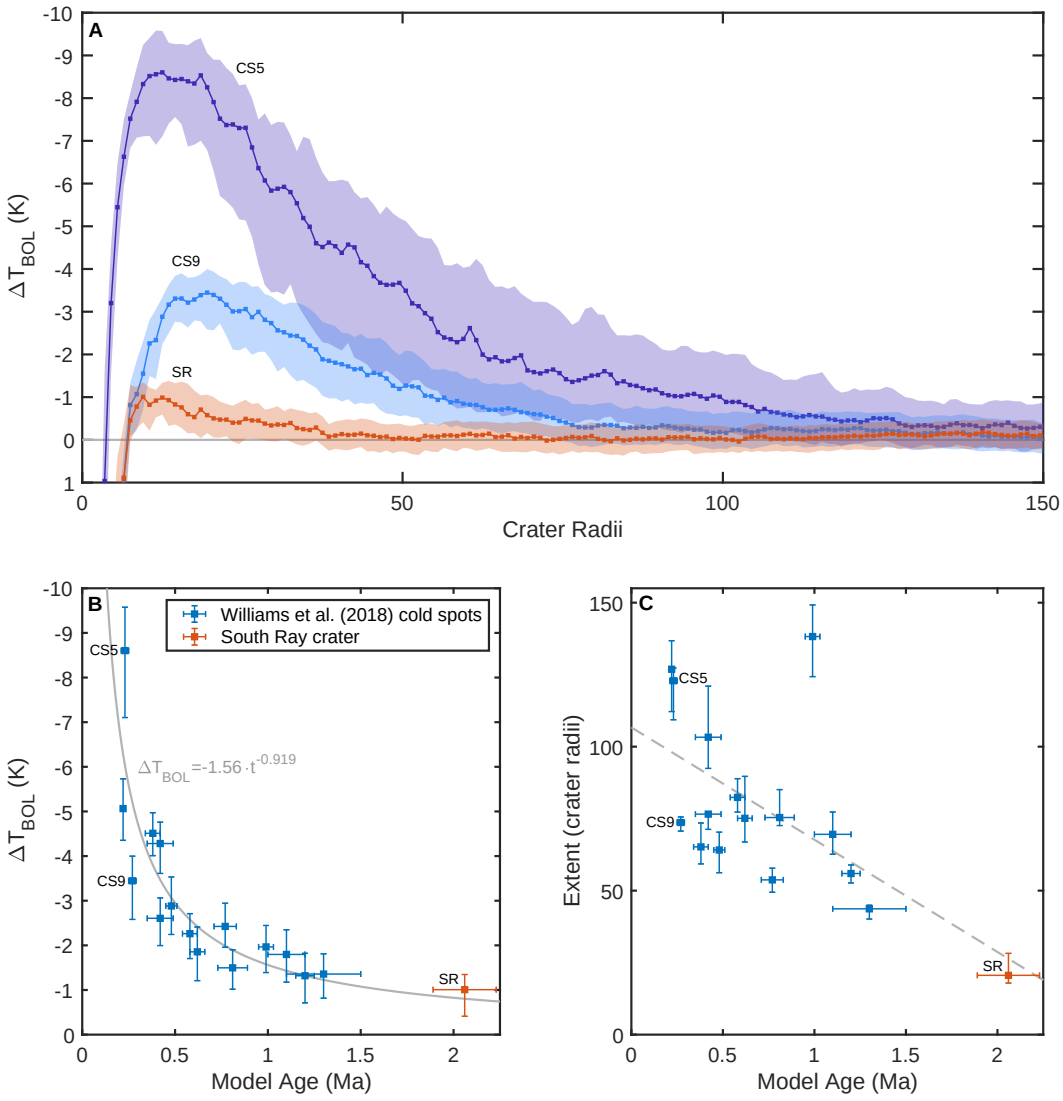

Figure 4.2: A) Radially binned ΔT_{BOL} at slope-adjusted midnight with distance for three example cold spots. Curves show the median and interquartile range. CS5 and CS9 refer to indexed craters in table 4.1 and SR denotes South Ray crater. B) Peak ΔT_{BOL} versus age for the cold spot craters dated by Williams et al. (2018a) and South Ray crater. C) The radial extent of each cold spot versus age, where extent is defined as the distance at which ΔT_{BOL} comes within 0.5 K of the background value (0.4 K and 0.6 K for the error bars).

spot's present day temperature anomaly is consistent with it with being an old and faded cold spot. In addition, this validates ages estimated by Williams et al. (2018a) with absolute ages from Apollo 16 samples. This suggests that the cratering rate over the last ∼2 Ma is roughly in agreement with current models of recent crater production (Williams et al., 2014; Speyerer et al., 2016).

Figure 4.2C shows the extent of each cold spot versus age, where extent is defined as the distance at which the ΔT_{BOL} comes within 0.5 K of background regolith. Cold spot size decreases with age from ∼100 crater radii initially to ∼20 crater radii for a cold spot the age of South Ray crater. This suggests that the present day South Ray cold spot is a small remnant of a once significantly larger and more prominent cold spot.

It is important to note that these trends may be specific to large cold spots craters. Williams et al. (2018a) shows that the global size-frequency distribution (SFD) of cold spot craters is consistent with a retention age of ∼150 ka when fit for ∼100 m diameter craters. This may suggest that larger cold spots persist for longer than smaller cold spots, possibly due to a difference in the initial magnitude of their thermophysical properties.

4.3.3 In-situ regolith properties

South Ray cold spot extends to the location of the Apollo 16 Lunar Module (LM) and Extravehicular Activity (EVA) traverses (figure 4.3A). Therefore, the Apollo 16 regolith samples and in-situ experiments are representative of faint cold spot properties. Figure 4.3B shows the mean relative density of the upper ∼15 cm of regolith inferred from the depths of astronaut footprints at each of the Apollo sites reported by Mitchell et al. (1974) (table 4.2). The mean relative densities for Apollo 11, 12, 14, 15, and 17 are very similar, while Apollo 16 is ∼7 percentage points lower. This difference is much larger than the standard error of any of the calculated mean values. A two-sample z-test comparing the Apollo 16 mean relative density to the other Apollo sites yields a p-value $\ll 0.05$, confirming that the Apollo 16 regolith is statistically different. This result provides in-situ evidence supporting

the hypothesis of Bandfield et al. (2014) that the low thermal inertia of cold spots is the result of a decompaction of the upper several centimeters of regolith.

For comparison, the average densities derived from thermal modeling (figure 4.1C and D) can be converted to equivalent relative densities using equation 4.2. Assuming reasonable values for the minimum and maximum packing density (ρ_{min}=1100 kg/m^3 and ρ_{max}=1800 kg/m^3), our thermal model results predict relative densities of ∼75% and ∼63% for background regolith and South Ray cold spot, respectively. This corresponds to a difference of ∼12 percentage points. This is a larger difference than we infer from footprint depths, which may be caused by uncertainties in the thermophysical parameters used in thermal modeling or in the laboratory testing of footprint depths. However, both methods see a roughly similar decrease in relative density on the order of ∼10 percentage points.

One complicating factor is that Apollo 16 is the only Apollo mission to land in the lunar highlands, so it is possible Apollo 16's lower relative density is intrinsic to highlands material and not specific to South Ray cold spot. An argument against this is that Diviner temperatures indicate a difference in regolith density between South Ray cold spot and the surrounding regolith. Additionally, Diviner nighttime temperatures between mare and highlands are very similar, indicating similar thermophysical properties on average (Bandfield et al., 2011; Hayne et al., 2017; Powell et al., 2023). However, we can further test this by looking at spatial variations in footprint depth relative to South Ray cold spot's extent.

Figure 4.3A shows the locations of several Apollo 16 research stations where footprint depths were measured (Mitchell et al., 1972). The Lunar Module (LM), Apollo Lunar Surface Experiments Package (ALSEP), and Station 4, 5, and 10 locations are comfortably within the cold spot region as seen by Diviner. Stations 1 and 8 are within the cold spot extent but are located at boundaries between the cold spot and regions which Diviner sees as slightly warm. Station 11 is near the rim of North Ray crater, well outside the extent of South Ray cold spot. Figure 4.3C shows the reported relative densities at these locations (Mitchell et al., 1972) as a function of distance from South Ray crater. The radially binned median temperature is also plotted and shows that South Ray cold spot extends to ∼10 km. The

Table 4.2: Summary of porosity and relative density results determined from the depths of astronaut footprints (Mitchell et al., 1972, 1974). For each location, the mean, standard deviation, and standard error of the mean are reported.

Location	No. of observations	Porosity, mean (%)	Standard deviation	Standard error	Rel. dens., mean (%)	Standard deviation	Standard error
Apollo 11	30	43.3	1.8	0.33	66.7	5.9	1.1
Apollo 12	88	42.8	3.1	0.33	67.9	10.1	1.1
Apollo 14	38	43.3	2.2	0.36	66.6	7.3	1.2
Apollo 15	117	43.4	2.9	0.27	66.0	9.6	0.9
Apollo 16	273	45.0	2.8	0.17	60.6	9.9	0.6
Apollo 17	141	43.4	2.4	0.20	66.2	8.0	0.7
All except Apollo 16	414	43.3	2.6	0.13	66.5	8.6	0.4
LM area	43	43.1	2.3	0.35	67.2	7.5	1.1
ALSEP area	59	45.2	3.9	0.51	59.4	14	1.8
Station 1	43	44.8	2.8	0.43	61.3	9.8	1.5
Station 4	26	44.8	1.3	0.25	61.7	4.5	0.9
Station 4 and 5	35	45.8	2.6	0.44	57.8	9.4	1.6
Station 8	20	45.0	2.3	0.51	60.8	8.1	1.8
Station 10	15	45.2	2.1	0.54	60.1	7.4	1.9
Station 11	12	43.7	1.5	0.43	65.4	5.0	1.4
All except LM and Station 11	198	45.1	2.8	0.20	60.3	9.9	0.7

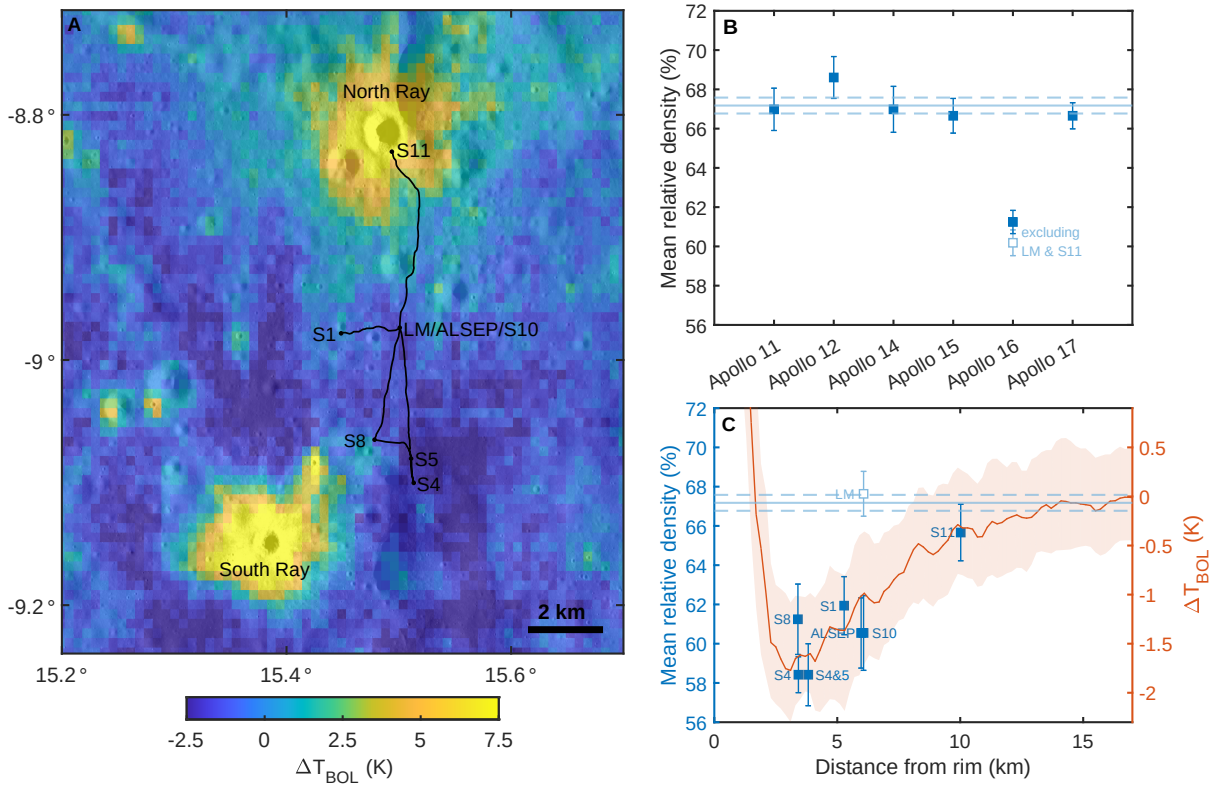

Figure 4.3: A) ΔT_{BOL} overlaid on LROC NAC imagery for the Apollo 16 EVA region. B) Mean relative density at each of the Apollo sites derived from the depth of astronaut footprints (Mitchell et al., 1974). Error bars show 1 standard error. The horizontal lines show the mean relative density for all Apollo sites except Apollo 16. C) Mean relative density for several locations at the Apollo 16 landing site (Mitchell et al., 1972) plotted against distance from South Ray crater. The orange line shows the radially binned ΔT_{BOL}.

research stations within the cold spot region have low relative densities with a slight trend of increasing relative density with distance from South Ray crater. Additionally, stations 1 and 8, which are located at boundaries in the cold spot temperature anomaly, have slightly higher relative density than the stations at similar distance located within the cold spot. This suggests that the Apollo footprint depths are spatially correlated with the observed cold spot thermophysical properties.

One exception to this trend is the Lunar Module (LM) location, which does not have a low relative density. However, the regolith at that location likely experienced significant modification due to exhaust during the descent of the LM. The photometric anomaly associated with the Apollo 16 blast zone extends ∼1 km from the LM (Clegg et al., 2012; Clegg and Jolliff, 2014). The ALSEP site and station 10 are located just outside the mapped extent of the blast zone, and both show relative densities that agree very well with each other and are lower than the LM relative density. Additionally, an investigation of the Lunakhod 1 and 2 rovers' tire tracks (Basilevsky et al., 2021) shows that the tire tracks were shallower near the landing platform than farther away, which they attributed to modification by exhaust during descent. We assert that the LM data point likely does not represent the pre-mission properties at that location.

The comparatively high relative density of Station 11, the only location outside of the cold spot extent, suggests that non-cold spot regolith in the Descartes highlands is similar to the other Apollo sites. However, Station 11 is located near the rim of North Ray crater, a region which Diviner sees as warm due to the presence of large boulders. While the presence of rocks does not necessarily indicate that the inter-rock regolith is anomalous, this geologic context makes it unclear whether the regolith at Station 11 is representative of typical, non-cold spot regolith in the Apollo 16 region. North Ray crater has an estimated age of ∼50±1.4 Ma (Arvidson et al., 1975; Maurer et al., 1978), significantly older than South Ray crater. One interpretation of the ∼Ma fading timescale for cold spots is that the density structure of the upper tens of centimeters returns to "normal" on roughly this timescale. This may suggest that the regolith at Station 11 has had enough time to achieve a

typical near-surface density. However, this is difficult to claim definitively without an in-situ density measurement of typical, non-cold spot highlands regolith. Future landed missions, particularly the Artemis missions which are scheduled to land in the South Polar highlands, can provide this information. In general, we show that a retrospective investigation of the Apollo 16 footprint depths indicate that the Apollo 16 regolith is lower density than the other Apollo sites and that there is a plausible spatial correlation with South Ray cold spot.

4.4 Discussion

Several mechanisms for cold spot formation have been proposed, including: 1) a laterally propagating granular flow initiated by a cascade of secondary impacts (Bandfield et al., 2014); 2) a ground-hugging gas flow of vaporized material (Bandfield et al., 2014); and 3) a seismic impulse which is able to disrupt near-surface regolith (Frizzell and Hartzell, 2022). Apollo 16 observations and orbital data can provide leverage towards deducing the cold spot formation mechanism.

A geologic map of South Ray crater ejecta (Reed, 1981) classifies much of the cold spot region as "thin discontinuous ejecta". This is supported by small incidence angle NAC imagery which shows oblique streaks of high reflectance material which often correspond to the low-temperature rays (figure 4.4). Small chains of secondaries can be identified within these streaks, suggesting that ejecta fragments large enough to produce meter-scale secondaries reached the locations where low temperatures are seen. These secondary chains and optical streaks do not cover the entire surface area of the cold spot, but it is plausible that the larger fragments were accompanied along their trajectories by smaller rocks and regolith grains capable of scouring the surface and reworking the regolith on the ∼cm scale. Muehlberger et al. (1972) reports rock counts from images taken along the Apollo 16 EVAs (figure 4.5), and finds that the concentration of >2 cm rock fragments decreases radially away from South Ray crater from ∼1-3% within the cold spot region to ∼0.5% near North Ray crater. The correlation of cold spot rays with high-reflectance streaks and the abundance of small rock

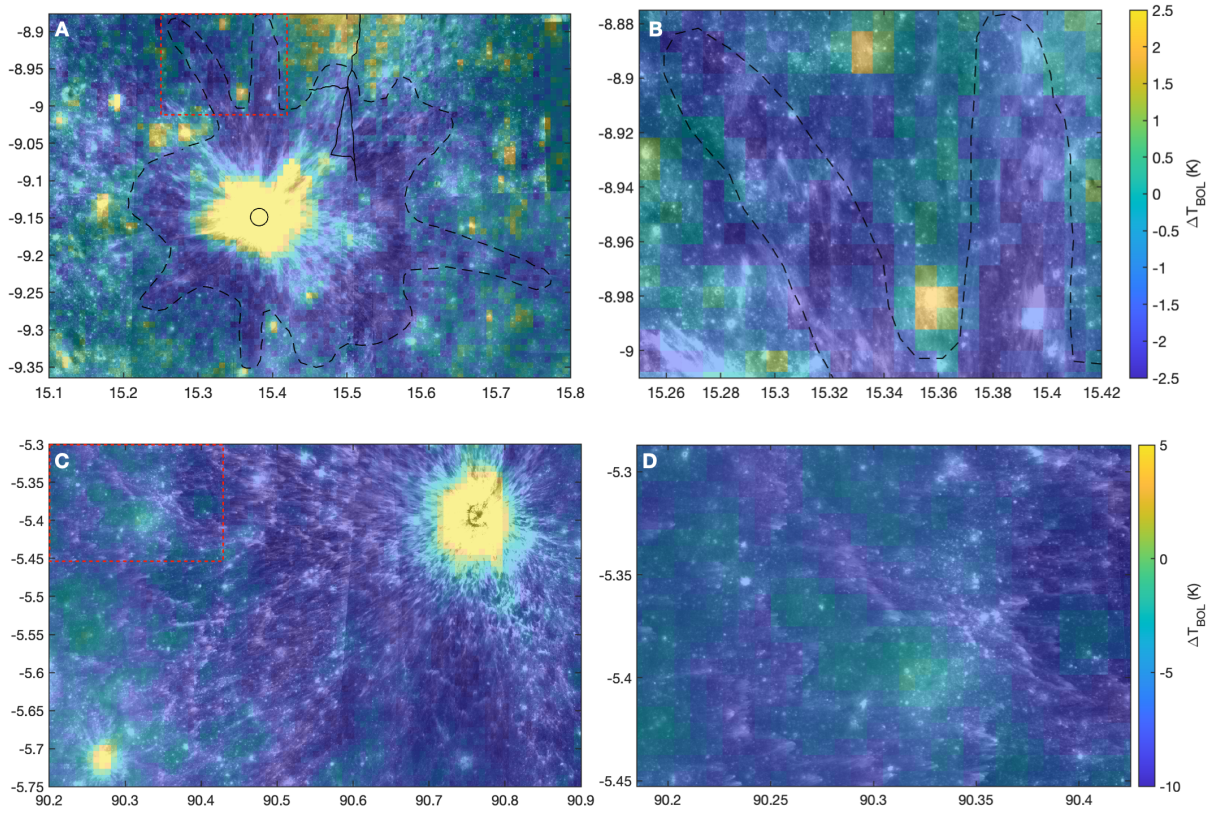

Figure 4.4: Diviner ΔT_{BOL} overlaid on LROC NAC small incidence angle imagery for: A) South Ray cold spot and B) a close-up of a low-temperature ray (indicated by the red box in A); and C) Bandfield cold spot and D) a close-up region with several discontinuous low-temperature rays (indicated by the red box in C). The dashed lines in A-B show the approximate outline of South Ray cold spot, and the solid line shows the Apollo 16 EVAs.

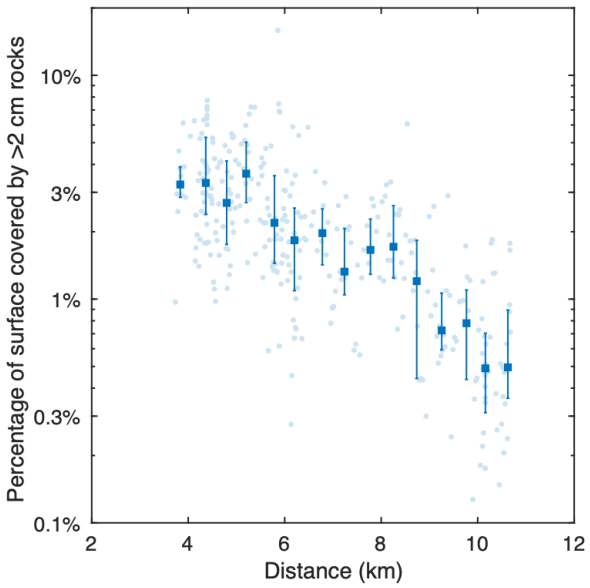

Figure 4.5: Percentage of the surface covered by >2 cm rock fragments based on Apollo 16 images with distance from South Ray crater. Data were extracted from figure 6-6 of Muehlberger et al. (1972).

fragments may suggest that cold spots are formed by reworking of the regolith by ejected material, though further modeling is required.

The measured thermal conductivity of Apollo 16 soil sample 68501 was shown to be lower than other measured Apollo samples after controlling for packing density (Cremers and Hsia, 1974). This is contradictory to the model that we present in this study, where cold spot thermal conductivity is lower because of a decrease in regolith packing and not because of a lower intrinsic thermal conductivity. Relatively few regolith samples were released for thermal conductivity measurements and there is significant variability between the measured values, so sample 68501 may have an anomalously low conductivity not representative of the average properties of the Apollo 16 region. It is also possible that this low conductivity measurement presents an alternative explanation for the low thermal inertia of cold spots, where a surficial layer of regolith with a low intrinsic conductivity covers the surface. In addition to packing density, variations in regolith composition and grain size can have signif-

icant effects on regolith thermal conductivity (Woods-Robinson et al., 2019; Sakatani et al., 2018). However, this would require an explanation for the lower relative density inferred from astronaut footprint depths. Further study of the thermophysical properties of Apollo 16 soils, particularly soils collected on and off of South Ray cold spot and at varying depth, could provide insight into the properties of cold spots.

4.5 Conclusions

The discovery of a cold spot at South Ray crater changes the geologic context of the Apollo 16 mission. We demonstrate that the -1 to -2 K temperature anomaly and $\sim$2.08$\pm$0.17 Ma age of South Ray crater are consistent with the fading behavior of other similarly sized cold spots, making South Ray crater the oldest known cold spot. Relative density estimates derived from astronaut footprint depths provide in-situ evidence that the Apollo 16 regolith is lower density within the upper $\sim$15 cm than the other Apollo sites (Mitchell et al., 1974), in agreement with thermal modeling. Furthermore, the relative density is lowest for locations within the extent of South Ray cold spot, and Station 11, the only location outside of the cold spot, has a similar relative density to the other Apollo sites (Mitchell et al., 1972). These Apollo era data support the hypothesis of Bandfield et al. (2014) that cold spots are caused by a decompaction of the upper centimeters of regolith. This is also relevant for future landed missions, as it demonstrates that meaningful differences in regolith properties can be measured using regolith compaction from astronaut footprints and likely rover wheel tracks, and that these differences correlate with orbital temperature observations.

Acknowledgements

This research was supported by the NASA Lunar Reconnaissance Orbiter project. Some of this research was carried out at the Jet Propulsion Laboratory, California Institute of Technology, under a contract with the National Aeronautics and Space Administration.

CHAPTER 5

Thermophysical characteristics of lunar cold spots: a comparison between the contemporary and pre-existing populations

Abstract

We present the thermophysical properties of a global survey of ∼10,000 cold spots and 20 new craters formed during the LRO mission lifetime. All new craters larger than ∼40 m in diameter have cold spots, suggesting that cold spots are likely formed by all lunar craters of sufficient size. We find that the temperature anomaly of new cold spots increases with crater size, suggesting that larger cold spots modify the regolith to greater depth. We predict that the cold spot of a new 1 km crater may modify the regolith to ∼m-scale depths.

New cold spots have a greater temperature anomaly than pre-existing cold spots, which indicates that the present-day properties of cold spots are mostly determined by size and fading. We use the global size-frequency distribution of cold spots to determine their retention age and fading rate. Using the Neukum production function, we find a retention age of ∼330 Ma. Puzzlingly, this is significantly lower than the ∼Ma fading timescale predicted by crater dating individual cold spots (Williams et al., 2018a). A possible solution to this discrepancy is that the production of 100 m to 1 km sized craters may have been lower than expected over the last ∼1 Ma. Continued detections of new lunar craters can test this hypothesis.

5.1 Introduction

Lunar cold spots are a class of impact feature characterized by regions of reduced nighttime temperature surrounding young impact craters (Bandfield et al., 2014; Williams et al., 2018a). Thermal modeling suggests that cold spots can be explained by a "fluffing-up" the upper several centimeters of regolith out to distances of 10-100 crater radii (Bandfield et al., 2014). This suggests that cold spots represent an important process for the mixing and evolution of the regolith. However, one problem with studying the thermophysical properties of the current cold spot population is that many cold spots are significantly faded and do not express their initial magnitude. For example, in chapter 4, we show that the temperature anomaly of large cold spots fades on ∼100 ka to ∼Ma timescales. During the ∼13 year LRO mission, repeat imagery by the LRO Camera (LROC) has led to the identification of hundreds of new craters formed during the mission lifetime (Speyerer et al., 2016, 2020). Most of these 'contemporary craters' are only a few meters in diameter, too small for a cold spot to be visible at Diviner's resolution of ∼240 m/pixel even considering that a cold spot is ∼30-100 times larger than the crater itself. However, 20 new craters larger than ∼20 m in diameter have been identified to date, with the largest being 70 m (figure 5.1). These may be large enough to form detectable cold spots (Williams et al., 2018a). The cold spots formed by these new craters would have the advantage of being virtually unaltered, allowing us to constrain the initial properties of cold spots without complications associated with fading.

In this work, we show that all of the new craters larger than ∼40 m have noticeable cold spots. We present the thermophysical properties of these contemporary cold spots and compare them with a catalog of ∼10,000 previously existing cold spots. We investigate the scaling of cold spot properties with crater size which can be used to infer the initial properties of larger cold spots that have not been observed forming during the LRO mission lifetime. Additionally, we use the size-frequency distribution of the global cold spot population and crater count derived ages of individual cold spots to constrain the evolution of cold spot properties with time.

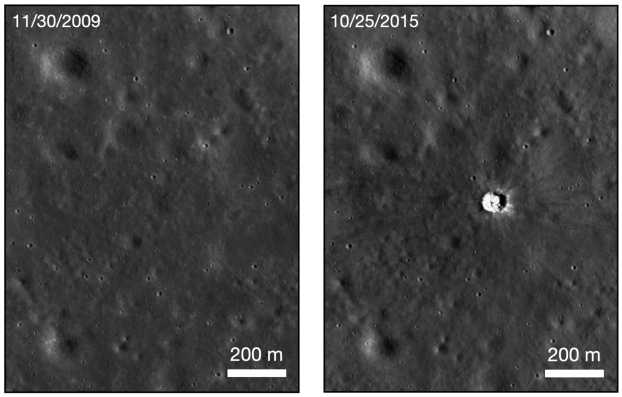

Figure 5.1: LROC NAC imagery pre- and post- impact (M114213813 and M1200397227) for a 70 m diameter new impact crater (crater A in table 5.1).

5.2 Data and methods

5.2.1 Nighttime temperature of contemporary cold spots

Speyerer et al. (2016, 2020) use change detection in LROC Narrow Angle Camera (NAC) and Wide Angle Camera (WAC) images to identify newly formed impact craters. Table 5.1 shows the location, diameter, and formation date for 20 new craters larger than 20 m in diameter. We compile Diviner (Paige et al., 2010a) channel 6-8 (13-23, 25-41, and 50-100 μm) brightness temperature data pre- and post- impact for a $0.5°\times0.5°$ region centered on each of the new craters. Using the methods described in chapter 3 (Powell et al., 2023), we produce midnight bolometric temperature anomaly ΔT_{BOL} maps accounting for the effect of surrounding topography on nighttime temperature. We difference the pre- and post- impact midnight temperature maps to reveal changes in temperature (figure 5.3).

For each crater, we bin ΔT_{BOL} in 3 crater radii annuli and characterize the potential cold spot by their peak median temperature anomaly. Most of the new craters were analyzed using the temperature difference map as it removes temperature signatures from nearby warm rocky regions and slopes fairly well. However, in cases where the pre-impact map had significant noise or unpopulated spatial bins, we instead used the post-impact map and excluded pixels with rock abundances $<0.75\%$.

Table 5.1: Summary of contemporary craters and the properties of their cold spots. Formation dates were determined by the earliest and latest appearance in either Diviner or LROC NAC imagery.

Index	Longitude (degrees)	Latitude (degrees)	Diameter (m)	Formation date min	Formation date max	-ΔT_{BOL} (K)
A	-39.7296	-22.3516	70	2012-10-02	2012-10-29	6.031
B	-63.066	43.3501	55	2010-04-17	2010-08-15	4.439
C	-44.068	-6.4364	50	2013-07-02	2013-08-12	3.224
D	150.216	-11.5148	45	2015-09-13	2015-12-17	2.265
E	-28.271	14.3947	43	2013-12-12	2014-01-08	3.630
F	-135.5103	-40.5259	40	2016-08-27	2016-10-20	2.503
G	-147.426	-32.1103	40	2014-02-26	2014-04-22	3.137
H	-157.826	-15.2894	40	2016-02-06	2016-03-31	2.863
I	52.1856	59.3701	35	2015-10-14	2016-01-21	2.818
J	149.1445	21.8806	35	2013-03-28	2013-07-14	1.367
K	93.2238	-14.6641	35	2015-09-17	2015-11-25	1.309[a]
L	-85.6485	-16.9333	31	2013-01-09	2013-02-05	0.937[a]
M	-20.4015	-17.1661	26	2013-09-11	2013-09-11	2.451
N	-10.793	31.1564	24	2018-07-26	2018-12-22	1.719
O	165.474	-16.7848	25	2017-02-24	2017-08-20	$\sim$0[b]
P	-11.096	-11.2112	25	2017-03-09	2017-04-05	1.478[a]
Q	14.6749	-25.261	24	2014-04-10	2014-02-14	$\sim$0[b]
R	-148.365	-1.3614	23	2013-11-23	2014-01-03	$\sim$0[b]
S	13.9011	-36.8189	22	2014-04-10	2014-05-07	1.220
T	-49.964	15.1696	21	2015-10-25	2015-12-05	$\sim$0[b]

[a]questionable cold spot detection (possibly noise), [b]no cold spot detected

5.2.2 Survey of pre-existing cold spots

Bandfield et al. (2014) and Williams et al. (2018a) created a global catalog of cold spots which includes about 2000 cold spots between ±50° N latitude. However, the most recent nighttime temperature maps (Powell et al., 2023) implement several significant improvements over the maps available at the time (Bandfield et al., 2011). Offsets in Diviner pointing have been corrected, improving the effective resolution and allowing for the identification of much smaller features. Additionally, the previous cold spot catalog shows a deficit of identified cold spots at higher latitudes in the highlands, indicating that variations in temperature caused by topography often hide cold spots. The updated nighttime temperature maps include a correction for topography, allowing for identification of fainter cold spots and cold spots at higher latitudes. The signal-to-noise ratio of the updated maps has also been improved due to the compiling of ∼13 years of Diviner data.

We use the updated bolometric and regolith temperature anomaly maps (Powell et al., 2023) to catalog additional cold spots not identified in the original survey. Because cold spot craters span a broad diameter range from ∼ 30 m to ∼ 2 km, cataloging all cold spots globally complete to the smallest discernible size is difficult. Instead, we perform 3 surveys at different scales that each focus on achieving completeness to progressively smaller diameter cutoffs. The BROAD survey captures cold spots between ±40° N latitude and is focused on obtaining large cold spots (figure 5.2). Investigation of the BROAD survey size-frequency distribution (SFD) indicates that this survey is most complete for craters larger than ∼400 m in diameter based on the diameter at which resolution roll-off occurs. The MID survey samples an equatorial swath from -10° to 0° N latitude and focuses on cataloging all cold spots with resolvable rocky pixels associated with the cold spot central crater. We find that this survey is complete to ∼200 m. The FINE survey was conducted over a region from -180° to -165° E longitude and ±20° N latitude and focuses on identifying all cold spots to the smallest discernible size. In total, we identify ∼10,000 cold spots, 5 times more than the original survey. About 1300 cold spots were identified in the relatively small region investigated in the FINE survey. Therefore, we expect that a global survey performed at

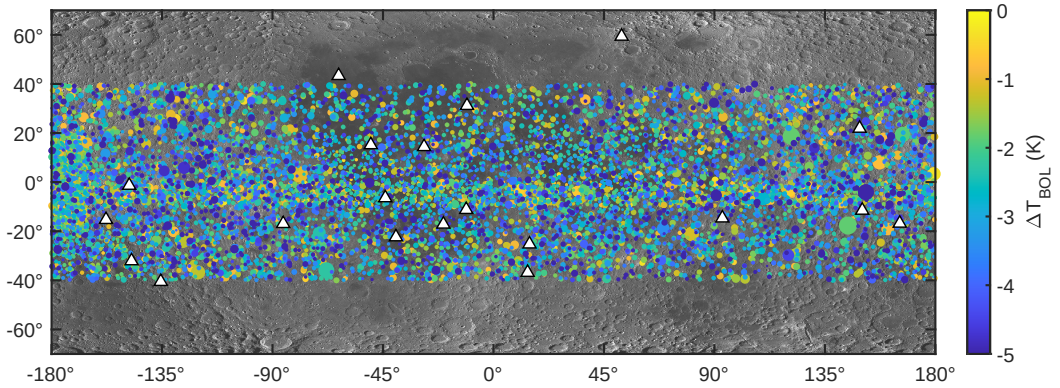

Figure 5.2: Catalog of cold spots from -40° to 40° N latitude with markers sizes scaled to crater diameter. Triangle markers correspond to contemporary craters formed during the LRO mission (Speyerer et al., 2016, 2020).

the highest level of completeness would find ∼90,000 identifiable cold spots. Each cold spot was characterized using the same method described for contemporary cold spots, where bolometric temperature anomaly (Powell et al., 2023) is binned radially away from the crater in 3 crater radii wide annuli, and this is used to determine the peak temperature anomaly.

5.2.3 Cold spot age estimates from superposed craters

Williams et al. (2018a) estimated the formation ages of 15 cold spot craters with D>800 m by counting superposed craters on their continuous ejecta blankets. We expand on this by dating 10 additional cold spots with moderate crater diameters of ∼500 m (table 5.2). Superposed craters were counted within a 2 crater radii annulus around each cold spot crater using LRO Narrow Angle Camera (NAC) images. While the continuous ejecta blanket erased most D<5 m craters within the count region, some pre-existing craters larger than D>10 were only partially buried. This is most apparent farther away from the crater where the ejecta blanket is thinner. Low incidence angle NAC images often show that pre-existing craters are covered by high reflectance material and are indistinct against the ejecta, while superposed craters typically disturb the ejecta. Therefore we exclude craters with noticeably

Table 5.2: Summary of the properties of 10 moderately-sized (D_{cr}∼500 m) cold spot craters. Model ages were determined by counting superposed craters on the central craters' continuous ejecta blankets.

Index	Longitude (degrees)	Latitude (degrees)	Diameter (km)	Age (Ma)	-ΔT_{BOL} (K)	Extent (crater radii)
P1	-148.187	12.599	0.51	0.11±0.03	4.96(4.47-5.30)	45(38-57)
P2	161.337	-9.081	0.43	0.082±0.03	5.84(5.34-6.09)	86(79-112)
P3	6.199	-9.191	0.43	0.18±0.04	4.01(3.76-4.33)	50(44-59)
P4	96.302	-6.984	0.48	0.20±0.05	4.36(3.85-4.67)	49(46-50)
P5	-15.686	-9.023	0.48	0.23±0.05	1.81(1.21-2.18)	39(38-44)
P6	-112.433	-18.236	0.43	0.31±0.06	2.52(2.06-2.76)	40(34-43)
P7	64.868	7.752	0.46	0.48±0.08	2.03(1.59-2.44)	31(26-33)
P8	157.368	17.234	0.57	0.10±0.03	7.83(7.16-8.46)	100(88-118)
P9	174.894	16.883	0.47	0.079±0.03	9.56(9.33-9.93)	67(61-73)
P10	-105.268	15.651	0.41	0.41±0.07	1.74(1.74-2.10)	24(25-27)

subdued morphology or by using low incidence angle NAC images when available, though this judgement may result in some uncertainty in the resulting model ages. Because these features are both small and young, few craters larger than a few meters have had time to accumulate. As a result, the Neukum Production Function (NPF) is inadequate for determining model ages, as it does not extend to craters smaller than 10 m in diameter. We instead fit the SFD of superposed craters using the Williams Production Function (WPF) (Williams et al., 2014), which extends to 1 m diameter craters and agrees well with the NPF at larger sizes.

5.3 Results and discussion

5.3.1 Thermophysical properties of contemporary cold spots

Figure 5.3 shows three examples of cold spots apparent in post-impact Diviner nighttime temperature data. New crater A, the largest new crater at 70 m in diameter, has the most prominent cold spot with a peak temperature anomaly of about -6 K. We find that all of the

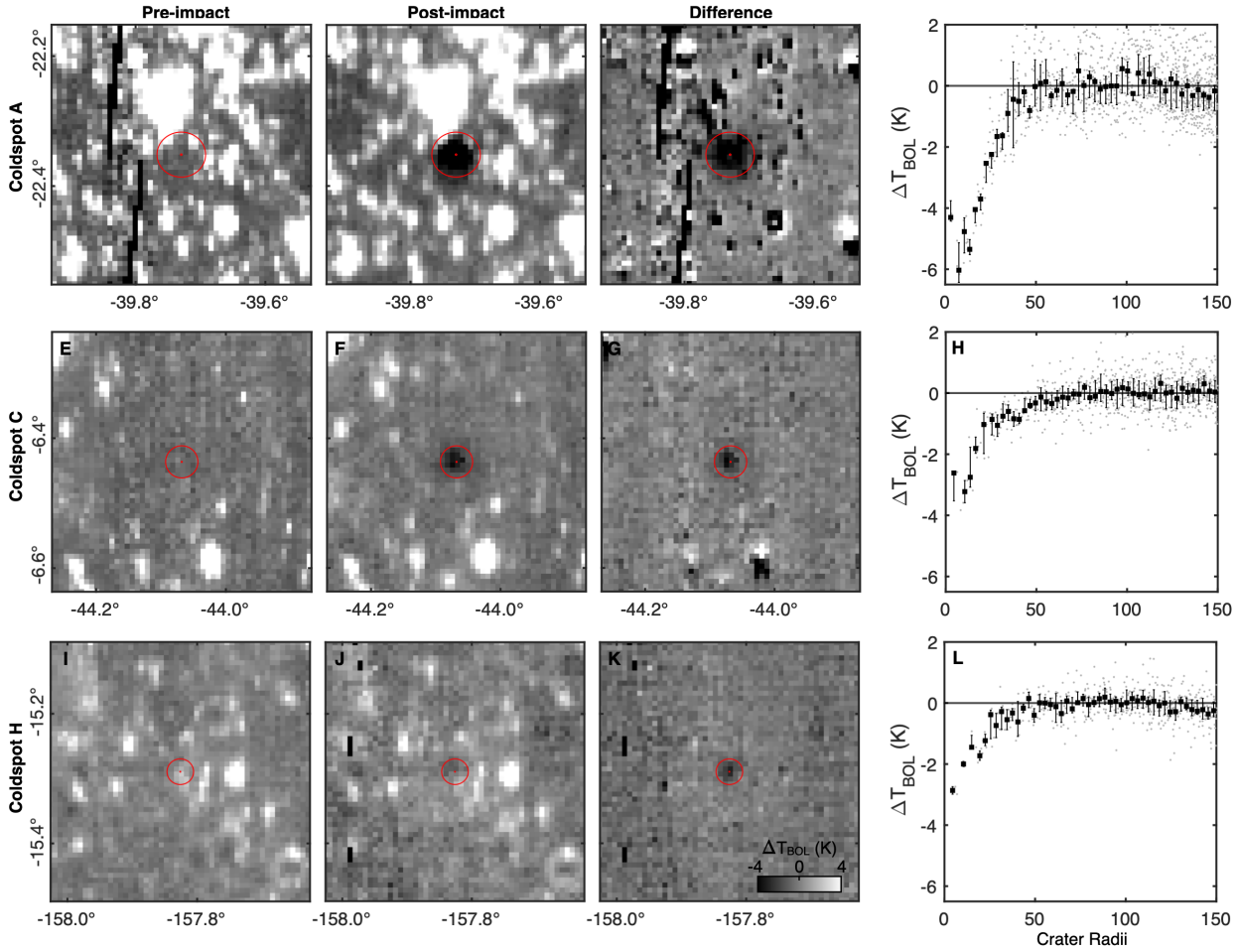

Figure 5.3: Examples of pre- and post- impact ΔT_{BOL} for 3 contemporary craters which have identifiable cold spots. The red circles show an annulus at 30 crater radii. Radial profiles show the median and interquartile range of ΔT_{BOL} in 3 crater radii bins.

new craters larger than 40 m in diameter have noticeable cold spots (Table 5.1). Some of these are difficult to detect in the post-impact temperature maps because they are located near warm rocky craters or on steep slopes, but are apparent in the difference maps which mostly remove these effects. Several of the craters between 25-40 m also have cold spots, though some are questionable detections with only a few pixels of low temperature that are not clearly radial to the central crater. The authenticity of these cold spot candidates is uncertain, and it is not clear whether they are genuine detections or data noise. This can be resolved with further Diviner observations. The new craters 20-25 m in diameter have either questionable cold spots or do not have apparent cold spots. It is possible that cold spots do exist around these smaller craters but with temperature anomalies below the noise floor of our current nighttime temperature maps. The positive identification of cold spots around all of the new craters large enough that cold spots should be reliably detected indicates that cold spots are ubiquitous features likely formed by all lunar impact craters larger than ∼35-40 m in diameter.

Figure 5.3A shows the temperature anomaly of the contemporary cold spots compared with the catalog of pre-existing cold spots. The ΔT_{BOL} of contemporary cold spots scales consistently with crater diameter, suggesting a greater magnitude of regolith modification by larger craters. Furthermore, the properties of the new cold spots form an upper envelope to the properties of pre-existing cold spots such that the new cold spots almost always have a greater ΔT_{BOL} when compared at the same size. This indicates that the present-day variability in cold spot thermophysical properties is dominated by fading, and not significantly by factors like local geology or impact conditions. Despite our global catalog containing cold spots formed across all terrain types, their properties do not exceed the properties of new cold spots. This is likely because most of the Moon is covered in a layer of regolith, and the uniformity of nighttime temperatures suggest that the upper tens of centimeters of regolith is similar for most regions of the Moon (Bandfield et al., 2011; Hayne et al., 2017; Powell et al., 2023).

The upper envelope of ΔT_{BOL} for the global cold spot population does not continue lin-

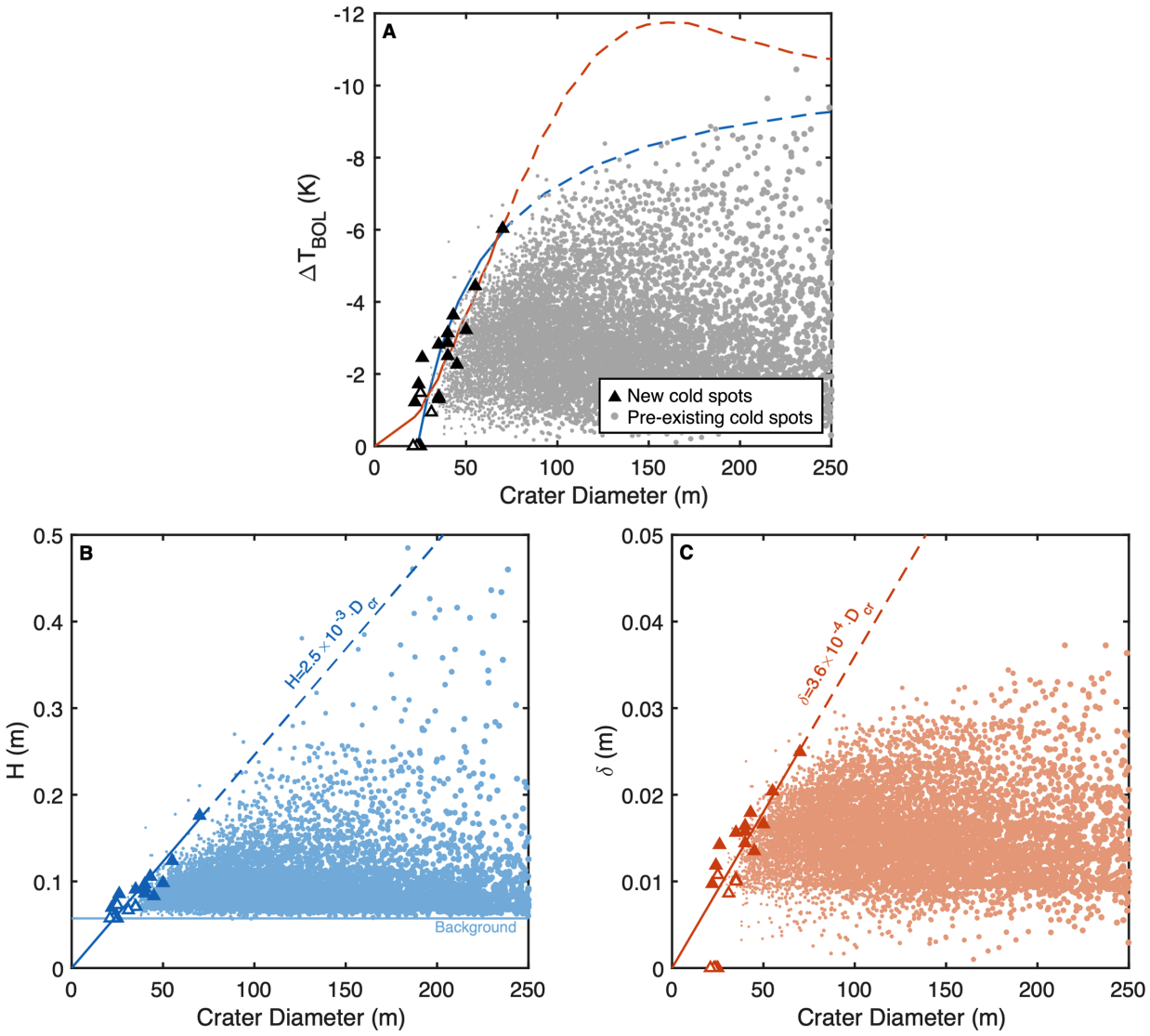

Figure 5.4: A) Peak bolometric temperature anomaly for the contemporary and pre-existing cold spot populations. The white triangular markers indicate new craters without an apparent cold spot or with a questionable cold spot detection. The new cold spots form an upper envelope to the properties of the entire cold spot population. B) and C) show equivalent peak H and δ values determined using a thermal model. The blue and red curves show linear best-fits to the H- and δ- models, respectively.

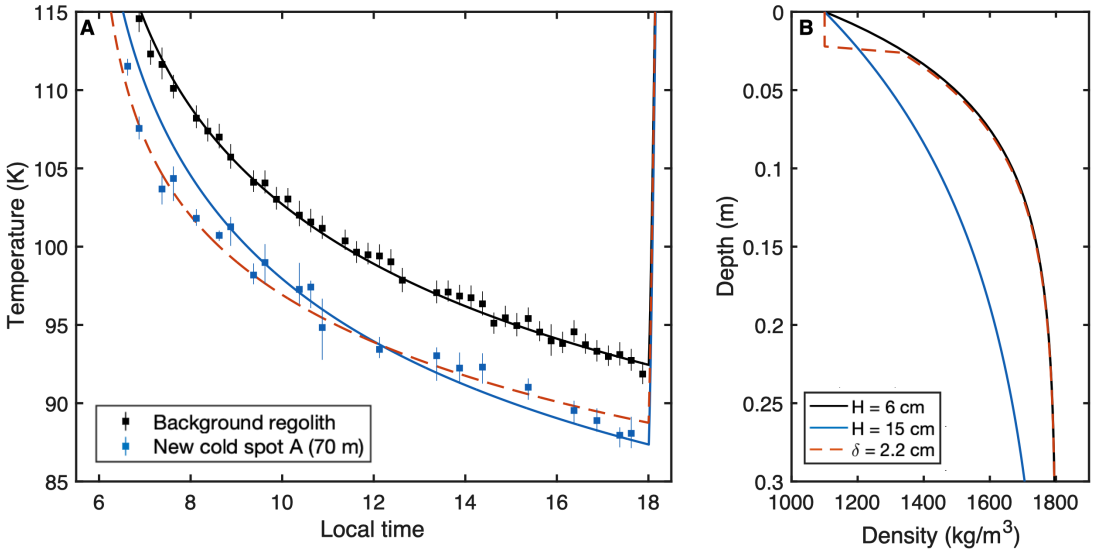

Figure 5.5: A) Median and interquartile range of T_{BOL} throughout the night for new cold spot A and typical surrounding regolith. The cooling curves are fit using a thermal model. We show results for two model types: an exponential increase in density with depth with scale height H, and a 2-layer model with a low-density surface layer of thickness δ overlying regolith with an otherwise typical subsurface density profile. B) shows the subsurface density profile for the best-fit thermal models.

early for larger cold spots, but instead begins to flatten for craters larger than ∼100 m in diameter. This occurs because nighttime temperatures are only sensitive to the thermophysical properties of the upper ∼10 cm of regolith. For example, the nighttime temperature of a surface with the upper 1 m of regolith at the lowest possible packing density would be indistinguishable from a surface with 10 m of regolith at the same density. The depth of regolith modification by cold spots may continue to increase with crater size, but with diminishing effects on nighttime temperature.

The depth of regolith modification can be estimated using a thermal model. Figure 5.5A shows the nighttime cooling trend for the cold spot around new crater A compared with its surrounding non-cold spot regolith. We fit the nighttime temperature curve to a thermal model using 2 different types of subsurface density profiles. The first model uses an exponential increase in density with depth following the equation: $\rho = \rho_d - (\rho_d - \rho_s)e^{-z/H}$, where ρ_s is the density at the surface, ρ_d is the density at depth, and H is the exponential scale height of the lower-density surface regolith layer (Hayne et al., 2017) (figure 5.5B). We refer to this model as the 'H-model'. The cooling behavior of the surrounding non-cold spot regolith is best fit with and H of ∼6 cm, consistent with past studies (Vasavada et al., 2012; Hayne et al., 2017; Powell et al., 2023). New cold spot A requires an H of ∼15 cm to achieve the observed nighttime temperatures, which suggests a significant alteration to the subsurface regolith.

It is possible to achieve similar nighttime temperatures using different subsurface density profiles. Because of this, we also fit the nighttime cooling curve using a 2-layer model where the upper surface regolith is decompacted to create a uniform, low-density layer of thickness δ. Below this layer, the density follows the profile of typical regolith with an H of 6 cm. We refer to this model as the 'δ-model'. We find that new cold spot A can be explained by a δ of ∼2.2 cm (figure 5.5B). This is a shallower depth of regolith modification than we find using the previous H-model, but is still significant for such a small crater given the relatively large spatial extent of its cold spot. These two models provide end-members on the depth of regolith modification by cold spots, where the H-model represents a gradual increase in

density with depth, and the δ-model represents an abrupt change from low density to higher density. The true depth of regolith modification is likely to fall between these two bounds if packing density is the main controller of thermal inertia.

Figures 5.4B and C show the equivalent peak H and δ for each cold spot as a function of crater diameter. We find that a linear fit to the H of new cold spots describes the upper envelope of the cold spot population fairly well even at larger sizes. This linear fit in H accurately captures the flattening of ΔT_{BOL} at larger sizes seen in figure 5.4A. Furthermore, this model accurately predicts the diameter at which cold spots may no longer be visible, as a crater $\sim$25 m in diameter is expected to form a cold spot with an H of $\sim$6 cm, which is the same value as typical, background regolith. It is possible that craters of this size or smaller do cause a decompaction of the regolith, however the upper $\sim$6 cm of regolith is already in a decompacted state so no change is observed. A linear fit to δ also describes the scaling of contemporary cold spots fairly well. However, it does not match the upper-envelope of the larger pre-existing cold spots as well as the H-model, which may suggest that the H-model more accurately captures cold spot regolith structure, though more evidence is required to confirm this. Projecting a linear extrapolation of the H- and δ- models to larger sizes suggests that a new 1 km crater may modify the regolith to depths of 0.36-2.5 m at their most prominent locations, significantly greater than was previously thought (Bandfield et al., 2014).

These results are based on a relatively simple thermal model, which we employ because there is not a unique solution to the Diviner nighttime temperature curve without additional constraints. Future studies would benefit from more accurate measurements of regolith density with depth over the upper 10-20 cm, which may be provided by the upcoming Artemis missions. Additionally, there are some discrepancies between laboratory measurements of regolith thermal conductivity (Fountain and West, 1970; Cremers and Hsia, 1974) and the temperatures at depth recorded during the Apollo missions (Keihm et al., 1973; Keihm and Langseth Jr, 1973; Hayne et al., 2017). Improved laboratory measurements of regolith conductivity under lunar-like conditions could help to improve thermal models, which may

systematically shift our estimated modification depths (Woods-Robinson et al., 2019; Martinez and Siegler, 2021). However, the comparative trends between cold spots are likely to persist even for different thermal models.

The newly-formed cold spots typically extend ∼30-50 crater radii. Ratios of pre- and post- impact NAC images reveal ray-like reflectance changes, termed "distal reflectance zones," which sometimes extend over 100 crater radii from new craters (Speyerer et al., 2016), further than the extent observed for the new cold spots. Visible changes can be caused by disruption of the upper mm of regolith, where thermal inertia requires changes on the cm scale to become noticeable. This may suggest that the process that creates the distal reflectance zones and cold spots is the same, but is only expressed as a cold spot within the region where the modification affects the upper centimeters, about ∼30 crater radii for these small, contemporary cold spot. Interestingly, large prominent cold spots often do extend to ∼100 crater radii, which may result from the equivalent distal reflectance zone for a larger crater modifying the regolith to proportionately greater depth.

5.4 Cold spot retention

We find that the pre-existing cold spot population has consistently lower ΔT_{BOL} than the newly formed cold spots (figure 5.4). This suggests that the present-day characteristics of cold spots are mostly a consequence of fading. ΔT_{BOL} can therefore be utilized as a relatively reliable proxy for age. The retention age of cold spots can be determined by comparing the global abundance of cold spot craters to the formation rate of craters predicted by a production model. By using increasingly restrictive ΔT_{BOL} thresholds, we can investigate the rate of fading within the cold spot population.

Figure 5.6A-C show the SFD of the global cold spot population for 3 levels of ΔT_{BOL}, fit using the Neukum Production Function (NPF) (Neukum et al., 2001). The NPF generally fits well for craters larger than ∼150 m in diameter, but below this size the SFD deviates from the NPF. This can in part be attributed to the resolution limitations of Diviner, which

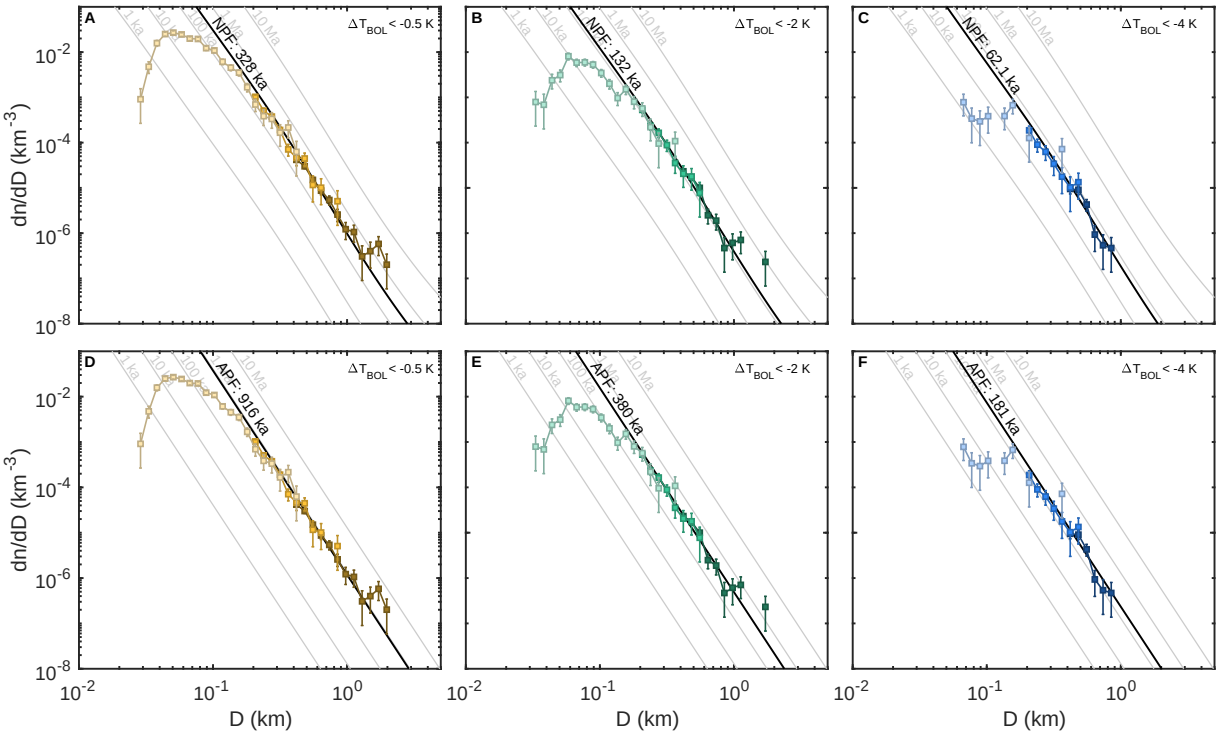

Figure 5.6: SFD of the cold spot population constrained by temperature anomaly. Marker colors differentiate between the FINE, MID, and BROAD surveys. A-C show best-fit retention age estimates using the Neukum Production Function (NPF) (Neukum et al., 2001). D-F show retention age fits using a hypothetical alternative production function where ∼1/3 the number of 100 m to 1 km sized craters form than in the NPF over the same interval.

makes it difficult to detect cold spots at small sizes. However, the lower initial ΔT_{BOL} for cold spots around small ∼30-150 m diameter craters may also contribute the observed roll-off. The diameter at which the SFD diverges from the NPF is similar to the diameter at which cold spot ΔT_{BOL} saturates at ∼8-9 K. The roll-off in the SFD appears to have two segments: a shallow-sloped segment between ∼60 m and ∼150 m diameter, and distinct roll-off for craters smaller than ∼60 m. We suggest that observed roll-off is partially contributed to by a real decrease in the number of smaller cold spots, which suggests that small cold spots fade more rapidly than larger cold spots. However, resolution limitations also certainly play a role and the diameter at which our catalog can be considered complete is difficult to determine.

The population of all identified cold spots has an best-fit retention age of ∼330 ka, while a sub-population with ΔT_{BOL}<-4 K has a much younger retention age of ∼60 ka. These findings generally align with the ∼150 ka retention age estimated by Williams et al. (2018a) using the previous global cold spot survey. However, these ages are in conflict with the ∼Ma fading timescale expected from the ages of individual large cold spots (Williams et al., 2018a) and South Ray crater (Arvidson et al., 1975; Eugster, 1999). There are too few cold spots globally to conform to a ∼Ma fading timescale. We explore several possible explanations for this puzzling discrepancy:

1. Our survey may be incomplete, which would lower the estimated retention age. To account for the observed difference, our detection efficiency would need to be ∼1/3. However, while it is possible that we failed to identify some small cold spots, it is unlikely that we missed a significant number of large cold spots as they are relatively easy to identify even with subtle temperature anomalies.

2. It is possible that not all craters form cold spots, so the cold spot population may not represent all craters formed within the last ∼Ma. However, all eight newly-formed craters larger than ∼40 m created cold spots, so it is unlikely that ∼2/3 of craters do not produce cold spots.

3. The crater counts performed on the dated cold spots may be too high, resulting in artificially inflated ages. This could be caused by contamination of the crater counts with self-secondaries. However, since the youngest age estimate is ∼200 ka (Williams et al., 2018a), the contribution of self-secondaries can't result in a shift in ages greater than this if each crater produced the same number of self-secondaries. Additionally, South Ray crater's ∼2 Ma age is based on cosmic ray exposure dating (Arvidson et al., 1975; Eugster, 1999), which is independent of crater counts.

4. The overall cratering rate within the last ∼Ma may be lower than predicted. However, this would also result in fewer ∼1-10 m craters, which would lead to proportionately lower age estimates from crater counting (Williams et al., 2018a). Additionally, Speyerer et al. (2016, 2020) shows that the contemporary production of ∼10 m craters agrees fairly well with expectations.

5. The form of the production function might be different from the NPF such that there are fewer ∼100 m to ∼1 km craters, but the number of ∼10 m craters is consistent with expectations. This would explain the observed global deficit of cold spots while preserving the ∼Ma age estimate determined from counting small, ∼1-10 m superposed craters. Interestingly, the current search for new craters (Speyerer et al., 2020) has detected slightly fewer 20-100 m craters over the mission lifetime than would be expected by the NPF (figure 5.7), though this may be a statistical artifact caused by the small number of >10 m new craters and detection inefficiencies. However, if this trend continues as more new craters are observed, this could suggest that the contemporary PF is slightly steeper-sloped than the Neukum PF at small sizes.

To test hypothesis 5, we adopt an alternative production function (APF) that describes the SFD of new craters larger than ∼10 m (Speyerer et al., 2020) as a power law: $n(> D) = ctD^{-b}$ where $c = 3.687 \times 10^{-13}$ and b=3.5 in units of km and yr (figure 5.7). It is not clear that this trend will persist as more craters are detected or if this can be extrapolated to larger sizes, so this alternative production function should be considered a hypothetical model. For

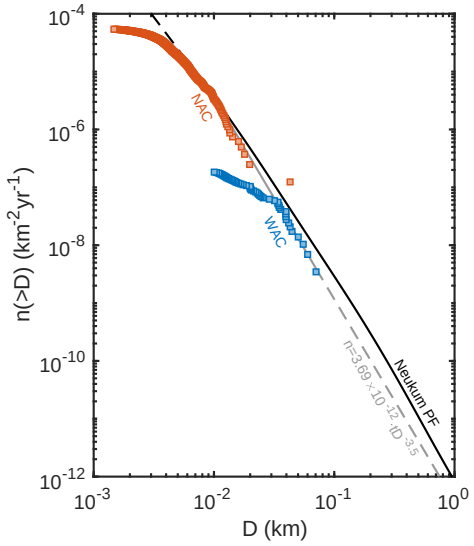

Figure 5.7: SFD of contemporary lunar impacts (Speyerer et al., 2016, 2020) compared to the Neukum production function and a hypothetical alternative production function which predicts fewer ∼100 m to km sized impacts.

craters larger than ∼100 m, the APF is lower than the NPF by a factor of ∼2-3. Figure 5.6D-F show the SFD of the global cold spot population fit using the APF. The estimated retention ages at each ΔT_{BOL} threshold are ∼2-3× greater than their equivalent fit using the NPF. Figure 5.8 shows the fading rate of cold spots determined from global retention and from age estimates of individual cold spots. The retention ages determined using the APF result in relatively good agreement with the fading rate of individual cold spots, with the estimated retention age of all identified cold spots being ∼1 Ma. This analysis may suggest that the observed number of cold spots globally and the ∼Ma fading timescale for cold spots derived from crater counts and radiometric dating may be evidence for a lower than expected production of ∼100 m to ∼ 1 km craters over the last ∼Ma.

While crater chronology models typically assume that the production function and impact rate have remained stable over the past 3 Ga, there is growing evidence for variations on short timescales that are not captured by the long-term average. For example, studies of large lunar and terrestrial craters suggest that the the flux of >1 km impactors may have increased

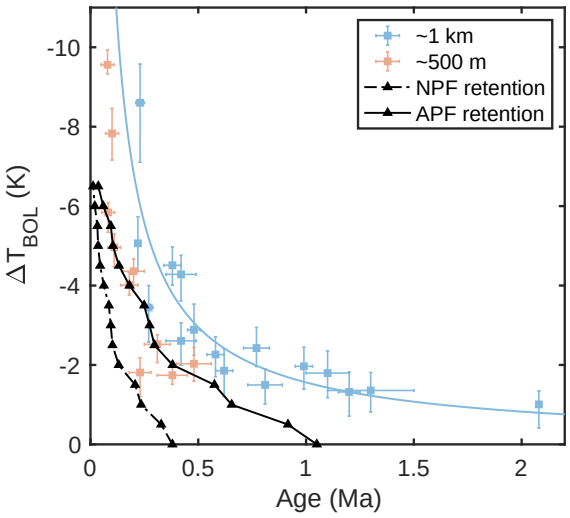

Figure 5.8: Cold spot fading behavior based on global retention age and the age estimates of individual cold spot craters.

by a factor of ∼2 during the last ∼100 Ma (Shoemaker, 1998; Grieve and Shoemaker, 1994; McEwen et al., 1997). This short-term spike has been correlated with the inferred breakup of asteroid Baptistina which is estimated to have occurred ∼160 Ma ago (Bottke et al., 2007). The distribution of meteorite cosmic ray exposure ages show several distinct peaks, likely associated with asteroid breakup events (Eugster et al., 2006; Jenniskens, 2018). Using rock abundance as a metric for crater age (Ghent et al., 2014), Mazrouei et al. (2019) finds a clustering of lunar crater ages at ∼388 Ma. Additionally, Kirchoff et al. (2013) found that a survey of ∼90 km craters on the Moon may indicate extended lulls in the impact rate with a short period of elevated impacts at ∼1.8 Ga. This finding arises from a mismatch between the estimated ages of large craters based on crater counting and the predicted interval of time required for the formation of such craters. Explaining this discrepancy requires that the flux of small impactors is uncoupled from the flux of the larger impactors, a scenario similar to the solution we propose to explain the deficit of large cold spots relative to their inferred ages. While the crater production function appears constant on long timescales, these studies suggest that the impact rate and the characteristic size of impactors fluctuate on short timescales, driven stochastically by asteroid breakup events. The global cold spot

population may provide evidence for a recent lull in the production of 100 m - 1 km sized craters. Continued detection of new craters will verify the contemporary production function and will help to resolve this conundrum.

5.5 Conclusions

We present the thermophysical properties of a global survey of ∼10,000 cold spots and 20 new craters formed during the LRO mission lifetime. We find that all new craters larger than ∼40 m in diameter form detectable cold spots, indicating that cold spots are ubiquitous features likely formed by all lunar craters of sufficient size. The temperature anomaly of new cold spots scales with crater size, suggesting that larger cold spots modify the regolith to greater depth. Projecting the derived thermophysical properties of the newly-formed cold spots to larger sizes, we predict that the cold spot created by a new 1 km crater may modify the regolith to m-scale depths at their most prominent locations.

The properties of new cold spots form an upper envelope to the properties of pre-existing cold spots. This suggests that the present-day cold spot properties are mostly determined by size and fading, and not significantly by other factors like terrain properties or impact conditions. We use the global SFD of cold spots to determine their retention age and fading rate. Using the Neukum production function, we obtain a best-fit retention age of ∼330 Ma. Curiously, this is significantly lower than the ∼Ma fading timescale predicted by crater dating individual cold spots (Williams et al., 2018a) and the radiometrically determined ∼2 Ma age of South Ray crater (Arvidson et al., 1975; Eugster, 1999). While small cold spots may be difficult to identify, it is unlikely that our survey is missing a significant number of large cold spots. In order to reconcile these findings, one option is that the recent (<Ma) production of lunar craters larger than 100 m - 1 km has been 2-3× lower than the expected historic average. This hypothesis can be tested by continued detection of new lunar impact craters.

Acknowledgments

We thank UCLA undergraduate researcher Sophie Taylor for updating the global cold spot catalog. This study was supported by the NASA Lunar Reconnaissance Orbiter project.

CHAPTER 6

Conclusions and future prospects

This thesis concludes six years of research conducted at UCLA. During this time, my research interests have been focused on impact cratering and chronology, ejecta processes, and the thermal modeling of planetary surfaces. This last chapter serves as a summary and proposes several future investigations which would expand on this work.

6.1 Mapping of distant secondaries

In chapter 2 (Powell et al., 2021), we develop a model for secondary accumulation with time, accounting for spatial clustering. Our results show that while the number of km-sized secondaries produced on Mars may exceed primaries after only a few 100 Ma, most of these secondaries are clustered around their parent primary, and regions far from large primaries experience significantly lower contributions of secondaries. Our model predicts that the crossover diameter between primaries and secondaries on a median martian surface exceeds 1 km after ∼1–2 Ga, though subsequent crater erasure has significantly influenced the number of secondaries visible today.

This work characterized the SFD and radial drop-off of secondaries using a catalog of large Martian craters (Robbins and Hynek, 2012). However, because the maximum size of secondaries tends to get smaller with distance, we were unable to definitively characterize the drop-off of secondaries at distances greater than ∼6-8 crater radii away. Small, distant secondaries are the most important for crater counting, as they are more difficult to identify and remove from crater counts. A detailed investigation of small, distant secondaries would

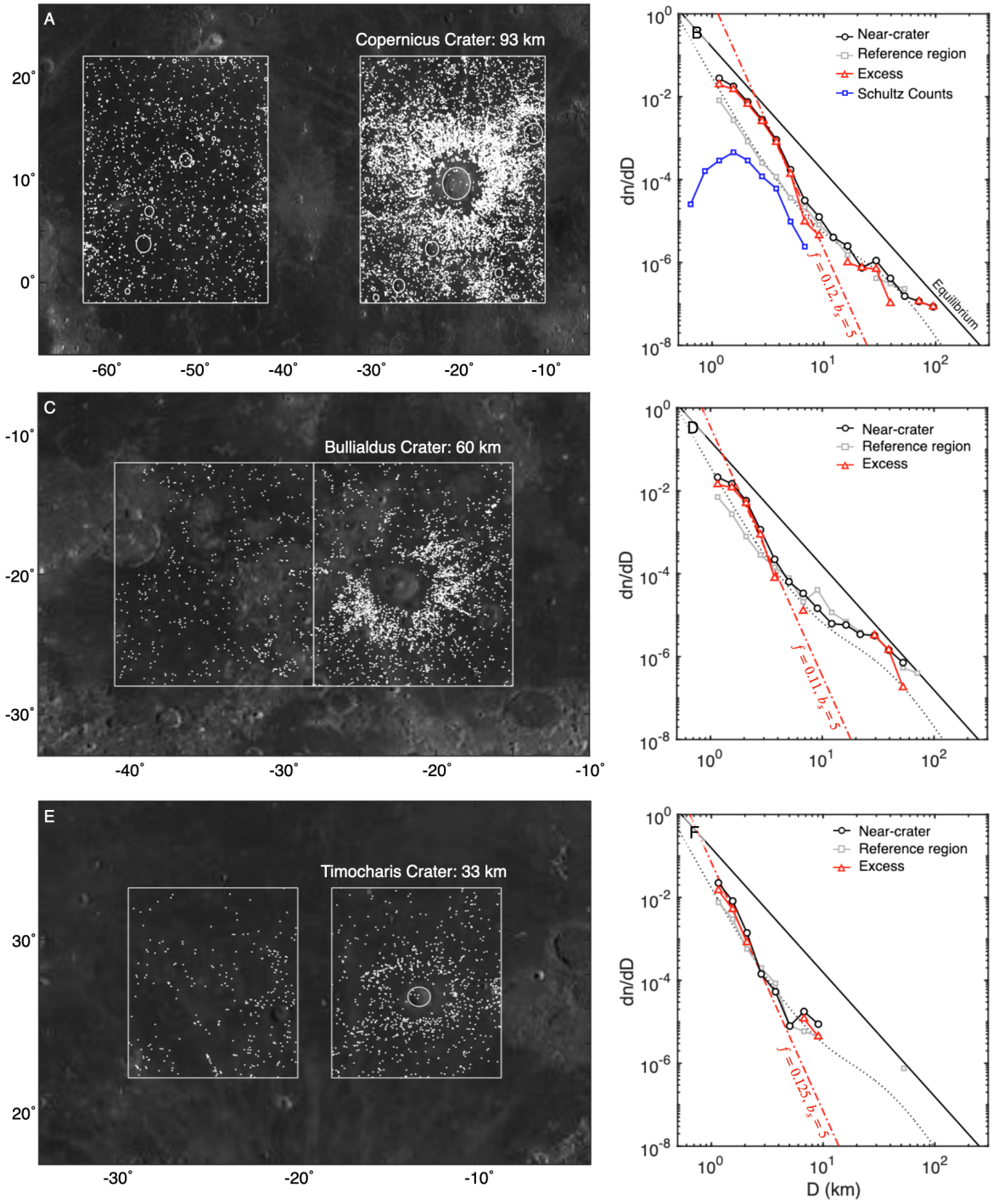

Figure 6.1: All >1 km craters from the Robbins (2019) crater database for three secondary fields compared to reference regions. All examples show an excess of small craters near the primary.

help to inform a more accurate model of global secondary accumulation. One advantage of the analysis we performed on Martian craters is that active surface processes on Mars have eroded many older craters, leading to regions like the northern lowlands which have relatively few background primaries, making the excess of recently-formed secondaries more apparent. However, this active erosion also erases smaller craters, making it difficult to accurately count small, distant secondaries. Conversely, craters on the Moon persist for longer periods of time until they are obliterated by other craters. While this means that there are an enormous number of both primary and secondary small craters that may be difficult to disentangle, we propose that statistical methods and morphological clues can be used to estimate the spatial density of small, distant secondaries.

Figure 6.1 shows the spatial density of craters larger than 1 km surrounding several lunar primaries. This approach is an analogous to our method of characterizing Martian secondaries in chapter 2. As expected, we see an excess of smaller craters which we infer to be secondaries. We fit this to a power law and find $f \approx 0.1$, similar to what we observe on Mars, and $b_s \approx 5$ which is slightly steeper than for Martian craters. This difference may be due to the lack of atmosphere, which allows smaller ejecta fragments to achieve high velocities without being slowed by drag. However, as in chapter 2 (Powell et al., 2021) we are unable to characterize secondaries at distances greater than ∼6-8 crater radii.

Using 0.5-1 m/pixel LROC NAC imagery and derived digital elevation models, we manually count ∼2000 craters larger than ∼100 m in a $4^\circ \times 2^\circ$ region located ∼11 crater radii from the 93 km Copernicus crater (figure 6.2). We classify craters as primary or secondary using morphological indicators and spatial clustering, though it is important to note that the population of assumed primaries may contain some unrecognized secondaries. The SFD of secondaries has a slope of roughly -5, in agreement with large secondaries close to Copernicus crater. Figure 6.2 shows that the extrapolated spatial density of >3 km secondaries at 11 crater radii agrees fairly well with the radial drop-off of secondaries close to Copernicus. This preliminary result suggests that the drop-off of secondaries inferred from the spatial density within ∼6-8 crater radii can be extrapolated to greater distances, though this should be

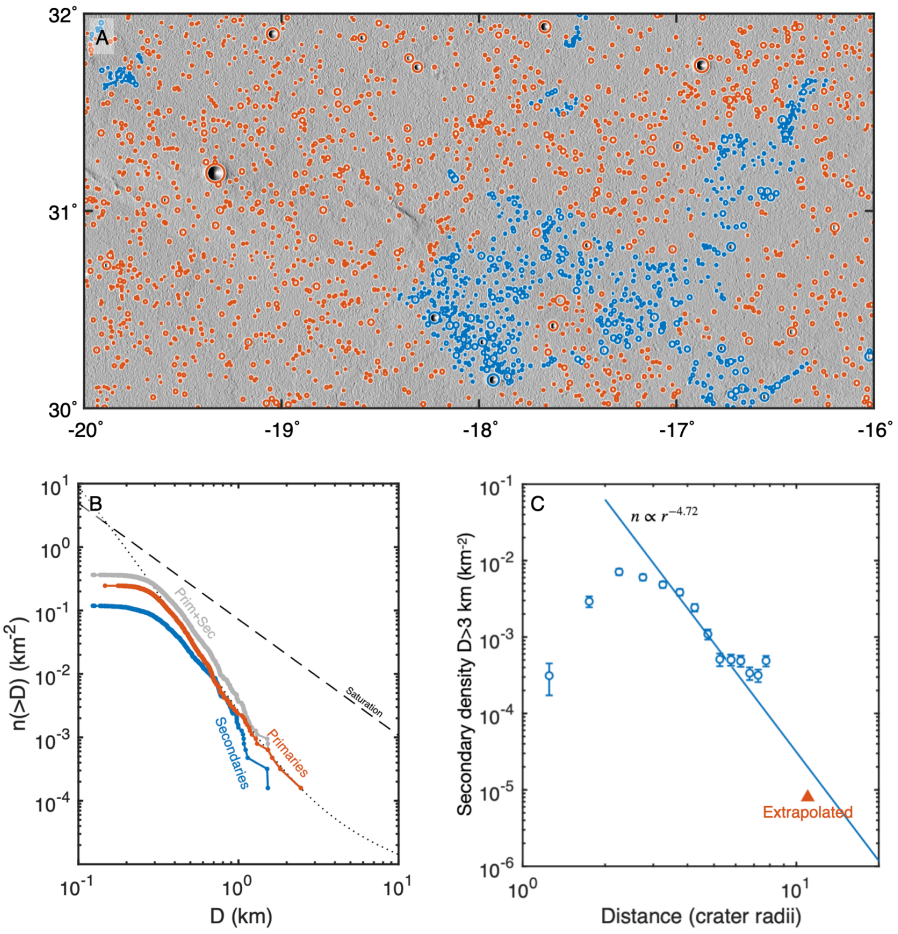

Figure 6.2: A) Counts of small craters (>100 m) in region of small region located ∼11 crater radii north of Copernicus crater, where blue markers indicate probable secondaries based on their morphology or clustering within rays. B) SFD of primaries and secondaries. C) The projected spatial density of secondaries near the crater based on counts of large craters and an extrapolation of the counts of smaller craters at ∼11 crater radii.

repeated over a larger region and for several primary craters of different size. This analysis can also be used to determine the fraction of secondaries clustered azimuthally along rays, which will further help to inform future models of secondary accumulation.

For b_s values >3, the total volume of ejected material required to produce progressively smaller sized craters would eventually exceed the volume excavated by the primary crater itself. Therefore, the power-law behavior observed for secondaries cannot continue to arbitrarily small sizes and instead must transition to a shallow slope or truncate completely below some critical size. The diameter at which this occurs has not been observed, but further study of small, distant secondary craters could identify or put limits on this value. This is significant for our understanding of regolith evolution, as it has been suggested that secondaries may be the principal contributor to impact gardening (Costello et al., 2018, 2021). Further constraints on the spatial and size-frequency distribution behavior of small secondaries could help to inform future models of regolith mixing.

6.2 Advances in thermal modeling

In chapter 3, we use ∼13 years of Diviner data to produce updated global maps of nighttime temperature and rock abundance for the Moon. We implement several improvements, including a correction for errors in instrument pointing, which result in an increase in effective resolution of ∼3.4× and ∼1.4× in the longitudinal and latitudinal directions, respectively. In addition, we develop a model which mostly removes the effect of topography on nighttime temperature by accounting for scattering and emission from the surrounding land.

The work presented in chapter 3 mostly focuses on using a thermal model to predict nighttime temperatures. However, it is worth highlighting that this thermal model can also be used to calculate temperatures at any time of day. Figure 6.3 shows an example of our thermal model applied to the lunar globe for a single solar configuration, illustrating its versatility for all local times. This model can be used to more accurately predict temperatures near the terminator, where topography plays a significant role, or for producing improved

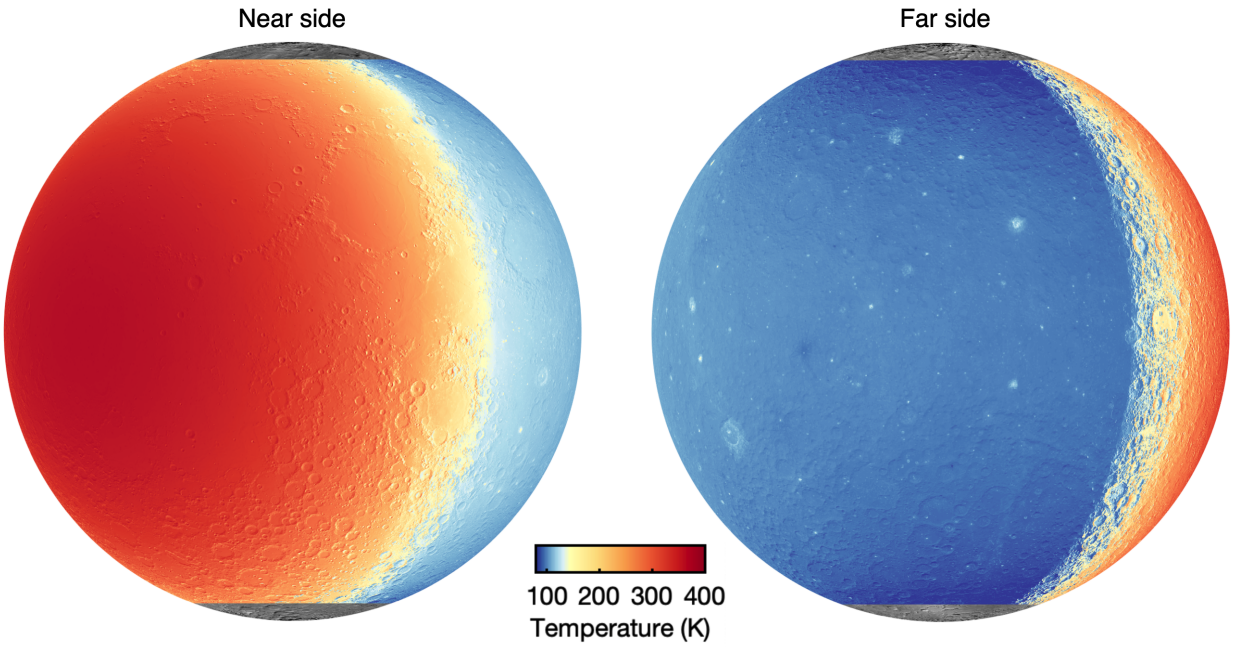

Figure 6.3: Example of the lunar diurnal thermal model described in chapter 3 (Powell et al., 2023) applied for a particular solar configuration (subsolar longitude of -45°E). This demonstrates that the thermal model can be applied for all local times.

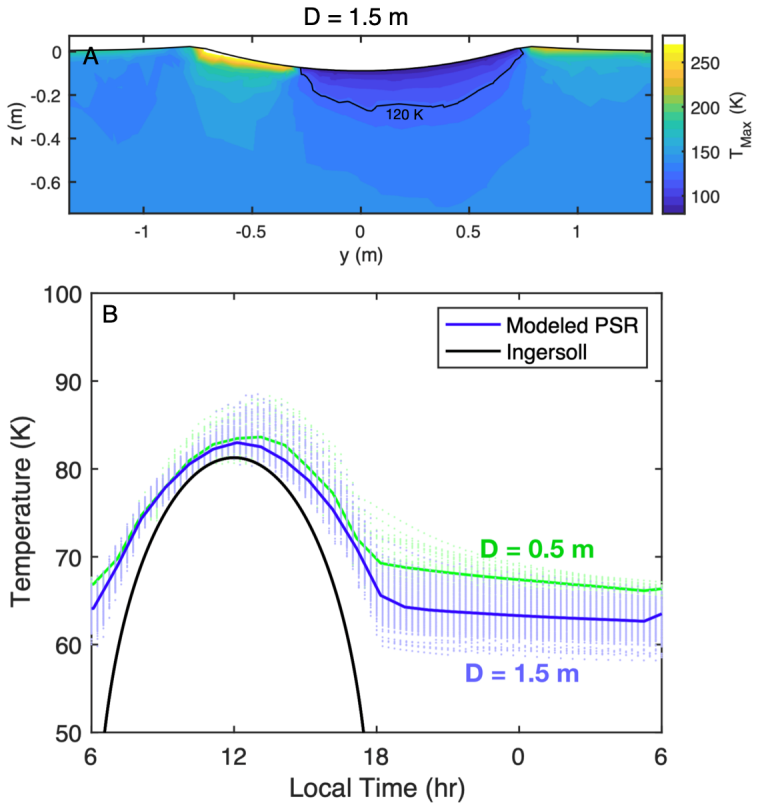

Figure 6.4: A) Example of the subsurface maximum temperature for a 1.5 m bowl-shaped crater with a depth-to-diameter of 1/14 at 85° latitude at B) Modeled diurnal PSR temperatures compared with Ingersoll et al. (1992) for two bowl-shaped craters of different size.

maps of daytime temperature.

The thermal model in chapter 3 accounts for the 3D effects of scattering and emission. However, the subsurface heat conduction for each pixel is treated as 1D and is independent of the thermal state of surrounding regions. For most applications, this is appropriate because the low thermal conductivity of regolith prevents significant lateral heat conduction. However, a full accounting for 3D heat conduction is beneficial for some applications. For example, the temperatures in shadowed regions of centimeter to meter scale topography can be influenced by lateral heat conduction.

We develop a finite volume 3D thermal conduction model. Figure 6.4A shows preliminary results for a permanently shadowed bowl-shaped crater at 85° latitude on the Moon (Powell

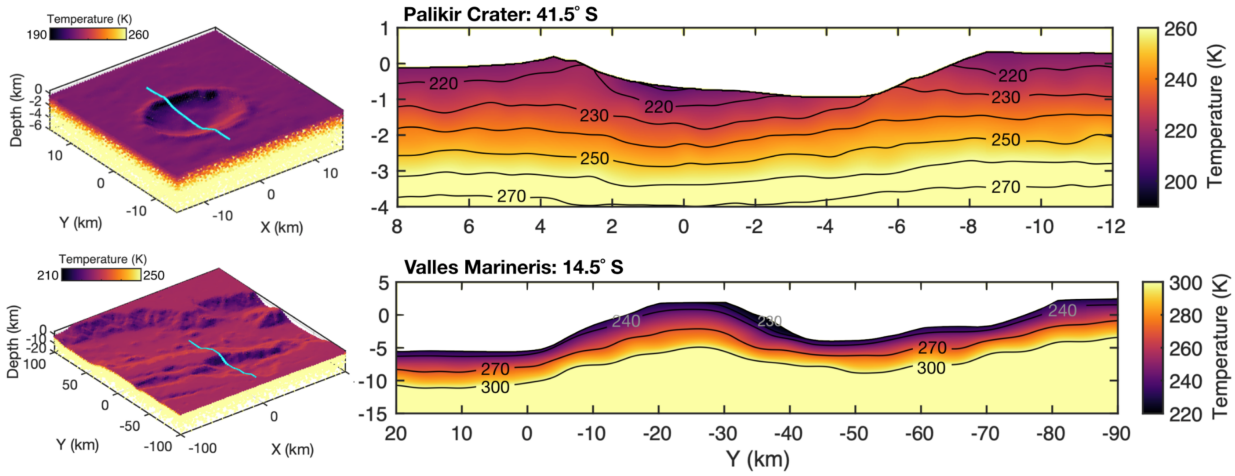

Figure 6.5: Example 3D cross sections of annual mean temperature for 2 regions on Mars using a 3D heat conduction model.

et al., 2020). The maximum shadow temperatures are greater than what would be predicted by radiative equilibrium with scattered and emitted light (Ingersoll et al., 1992). Additionally, this effect is more pronounced for smaller craters, suggesting a contribution from lateral heat flow. This may effect the retention of volatiles on small scales, where shadows below some size may not have adequately low temperatures to trap volatiles.

Additionally, 3D conduction may influence the directional emission characteristics of the Moon at night. The daytime emission phase function is usually explained by invoking a rough surface where certain facets receive more or less solar illumination based on of their orientation (Rubanenko et al., 2020; Jhoti et al., 2023). However, this directional emission behavior continues to persist throughout the night, despite no solar illumination driving differences in temperature. This is likely caused by heat stored in the subsurface escaping during the night, which can be investigate using our 3D thermal model.

This model can also be applied at large scales to determine subsurface heat flow and regions where volatile may be stable. For example, figure 6.5 shows subsurface cross sections of mean temperature for two martian regions. Our preliminary results suggest that topographic variations in annual mean surface temperature can warm the subsurface to a depth

comparable to the scale of the topography (Powell et al., 2019). This has implications for the stability of potential subsurface ice or liquid water on Mars.

6.3 Cold spots and regolith evolution

In chapter 4, we show that South Ray crater at the Apollo 16 landing site has a cold spot. Its faint temperature anomaly and ∼2 Ma age (Eugster, 1999) are consistent with the fading timeline of other large cold spots. Additionally, astronaut footprints are statistically deeper at Apollo 16 than the other Apollo sites, suggesting that cold spots are caused by a decompaction of the upper regolith. In chapter 5, we present the thermophysical properties of a global survey of cold spots and several new cold spots formed during the LRO mission lifetime. We show that the temperature anomaly of pristine cold spots scales with crater diameter, suggesting a greater depth of regolith modification. Using thermal modeling, we present bounds on the depth of regolith modification by cold spots. Additionally, we show that the properties of new cold spots form an upper envelope to the properties of pre-existing cold spots, indicating that the present-day properties of cold spot are a result of fading. Curiously, there are fewer cold spots globally than would be predicted based on a ∼Ma fading timescale. This may suggest either that our cold spot survey is incomplete or that the production of ∼100 m to ∼1 km sized craters has been ∼2-3× lower than expected over the last ∼1 Ma. This can be verified by continued monitoring of newly-formed craters on the Moon.

One of the most interesting aspect of cold spots is that they represent modification of the regolith to great distances, and may be an important contributor to the evolution and mixing of the regolith over time. The regolith is periodically overturned by impact craters in a process called impact gardening (Gault et al., 1974). Small impacts overturn the upper regolith fairly frequently and greater depths are overturned more rarely. The typical depth of regolith overturn progresses to greater depth with time as the surface becomes saturated with craters of a particular size (Gault et al., 1974; Morris, 1978; Costello et al., 2021). A

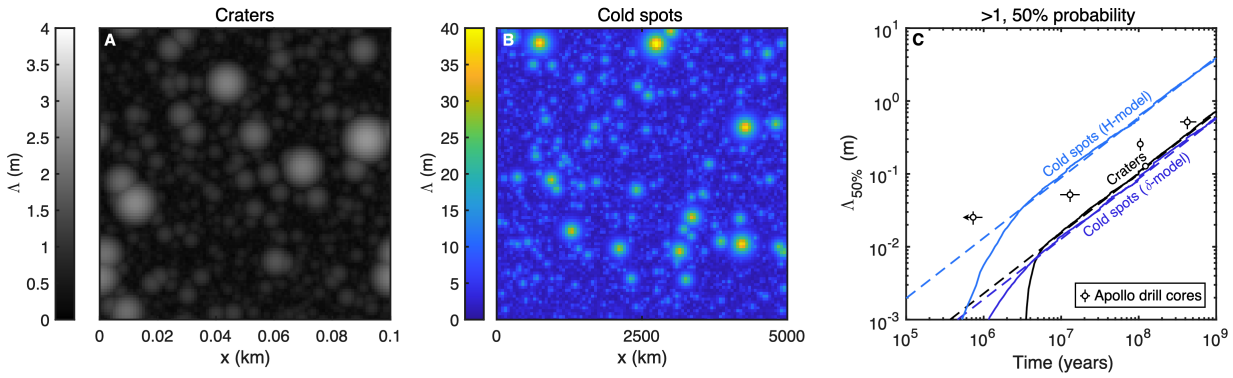

Figure 6.6: Example model for the modification depth Λ by A) craters and B) cold spots. C) The median modification depth with time for craters and cold spots compared to cosmic ray exposure ages from Apollo drill cores (Morris, 1978).

similar argument can be made for cold spots, which also modify the regolith to a depth which scales with crater size. We develop a simple numerical model where both craters and cold spots are formed on a surface, and the maximum modification depth for each pixel is tracked. Figure 6.6 shows preliminary results which may suggest that cold spots modify the regolith to depths similar to or greater than traditional craters. One caveat is that it is not clear whether vertical mixing occurs during cold spot formation. Additionally, it is important to note that the depth of cold spot modification is based on fairly simple thermal model assumptions. Further constraints could help to better define the regolith density profile of cold spots, which would have implications for the evolution of the regolith.

Bibliography

Aharonson, O. and Schorghofer, N. (2006). Subsurface ice on mars with rough topography. *Journal of Geophysical Research: Planets*, 111(E11).

Arvidson, R., Crozaz, G., Drozd, R., Hohenberg, C., and Morgan, C. (1975). Cosmic ray exposure ages of features and events at the apollo landing sites. *The Moon*, 13(1):259–276.

Baldwin, R. B. (1949). The face of the moon. *Chicago] Univ. of Chicago Press [1949.*

Bandfield, J. L., Cahill, J. T., Carter, L. M., Neish, C. D., Patterson, G. W., Williams, J.-P., and Paige, D. A. (2017). Distal ejecta from lunar impacts: Extensive regions of rocky deposits. *Icarus*, 283:282–299.

Bandfield, J. L., Ghent, R. R., Vasavada, A. R., Paige, D. A., Lawrence, S. J., and Robinson, M. S. (2011). Lunar surface rock abundance and regolith fines temperatures derived from lro diviner radiometer data. *Journal of Geophysical Research: Planets*, 116(E12).

Bandfield, J. L., Hayne, P. O., Williams, J.-P., Greenhagen, B. T., and Paige, D. A. (2015). Lunar surface roughness derived from lro diviner radiometer observations. *Icarus*, 248:357–372.

Bandfield, J. L., Song, E., Hayne, P. O., Brand, B. D., Ghent, R. R., Vasavada, A. R., and Paige, D. A. (2014). Lunar cold spots: Granular flow features and extensive insulating materials surrounding young craters. *Icarus*, 231:221–231.

Barker, M. K., Mazarico, E., Neumann, G. A., Zuber, M. T., Haruyama, J., and Smith, D. E. (2016). A new lunar digital elevation model from the lunar orbiter laser altimeter and selene terrain camera. *Icarus*, 273:346–355.

Basilevsky, A., Malenkov, M., Volov, V., Abdrakhimov, A., Kozlova, N., Zubarev, A., and Nadezhdina, I. (2021). Estimation of the strength of the lunar soil by the depth of the lunar rover wheel tracks. *Solar System Research*, 55:285–308.

Benz, W., Slattery, W., and Cameron, A. (1989). Tilting uranus in a giant impact. *Meteoritics*, 24:251.

Bierhaus, E., McEwen, A. S., Robbins, S., Singer, K., Dones, L., Kirchoff, M., and Williams, J.-P. (2018). Secondary craters and ejecta across the solar system: Populations and effects on impact-crater–based chronologies. *Meteoritics & Planetary Science*, 53(4):638–671.

Bierhaus, E. B., Chapman, C. R., and Merline, W. J. (2005). Secondary craters on europa and implications for cratered surfaces. *Nature*, 437(7062):1125–1127.

Bierhaus, E. B., Chapman, C. R., Merline, W. J., Brooks, S. M., and Asphaug, E. (2001). Pwyll secondaries and other small craters on europa. *Icarus*, 153(2):264–276.

Bottke, W. F., Vokrouhlickỳ, D., and Nesvornỳ, D. (2007). An asteroid breakup 160 myr ago as the probable source of the k/t impactor. *Nature*, 449(7158):48–53.

Braslau, D. (1970). Partitioning of energy in hypervelocity impact against loose sand targets. *Journal of Geophysical Research*, 75(20):3987–3999.

Brown, H. (1960). The density and mass distribution of meteoritic bodies in the neighborhood of the earth's orbit. *Journal of Geophysical Research*, 65(6):1679–1683.

Brown, P., Spalding, R., ReVelle, D. O., Tagliaferri, E., and Worden, S. (2002). The flux of small near-earth objects colliding with the earth. *Nature*, 420(6913):294–296.

Canup, R., Barr, A., and Crawford, D. (2013). Lunar-forming impacts: high-resolution sph and amr-cth simulations. *Icarus*, 222(1):200–219.

Canup, R. M. (2004). Simulations of a late lunar-forming impact. *Icarus*, 168(2):433–456.

Canup, R. M. and Asphaug, E. (2001). Origin of the moon in a giant impact near the end of the earth's formation. *Nature*, 412(6848):708–712.

Carrier III, W. D., Mitchell, J. K., and Mahmood, A. (1973). The relative density of lunar soil. In *Lunar and Planetary Science Conference Proceedings*, volume 4, page 2403.

Carrier III, W. D., Olhoeft, G. R., and Mendell, W. (1991). Physical properties of the lunar surface. *Lunar sourcebook*, pages 475–594.

Chapman, C. R., Veverka, J., Belton, M. J., Neukum, G., and Morrison, D. (1996). Cratering on gaspra. *Icarus*, 120(1):231–245.

Christensen, P. R., Jakosky, B. M., Kieffer, H. H., Malin, M. C., McSween, H. Y., Nealson, K., Mehall, G. L., Silverman, S. H., Ferry, S., Caplinger, M., et al. (2004). The thermal emission imaging system (themis) for the mars 2001 odyssey mission. *Space Science Reviews*, 110:85–130.

Clegg, R. and Jolliff, B. (2014). Comparing rocket exhaust effects across lunar landing sites using lro narrow angle camera images. In *Earth and Space 2014*, pages 131–139. 14th ASCE Aerospace Division Conference on Engineering, Construction, and Operations in Challenging Environments, American Society of Civil Engineering, Saint Louis, MO.

Clegg, R. N., Jolliff, B. L., and Metzger, P. T. (2012). Photometric analysis of the apollo landing sites. In *Earth and Space 2012: Engineering, Science, Construction, and Operations in Challenging Environments*, pages 218–227. 14th ASCE Aerospace Division Conference on Engineering, Construction, and Operations in Challenging Environments, American Society of Civil Engineering, Saint Louis, MO.

Conel, J. E. (1969). Infrared emissivities of silicates: Experimental results and a cloudy atmosphere model of spectral emission from condensed particulate mediums. *Journal of Geophysical Research*, 74(6):1614–1634.

Costello, E. S., Ghent, R. R., and Lucey, P. G. (2018). The mixing of lunar regolith: Vital updates to a canonical model. *Icarus*, 314:327–344.

Costello, E. S., Ghent, R. R., and Lucey, P. G. (2021). Secondary impact burial and excavation gardening on the moon and the depth to ice in permanent shadow. *Journal of Geophysical Research: Planets*, 126(9):e2021JE006933.

Crater Analysis Techniques Working Group (1979). Standard techniques for presentation and analysis of crater size-frequency data. *Icarus*, 37(2):467–474.

Cremers, C. and Hsia, H. (1974). Thermal conductivity of apollo 16 lunar fines. In *Lunar and Planetary Science Conference Proceedings*, volume 5, pages 2703–2708.

Curren, I., Paige, D., Russell, P., and Moon, S. (2018). Geologic evidence for an impact ejecta origin of tycho's antipode terrain. In *European Planetary Science Congress*, pages EPSC2018–748.

Daubar, I., Banks, M., Schmerr, N., and Golombek, M. (2019). Recently formed crater clusters on mars. *Journal of Geophysical Research: Planets*, 124(4):958–969.

Daubar, I., McEwen, A., Byrne, S., Kennedy, M., and Ivanov, B. (2013). The current martian cratering rate. *Icarus*, 225(1):506–516.

Daubar, I., McEwen, A., Byrne, S., Kreslavsky, M., Saper, L., and Kennedy, M. (2014). New dated impacts on mars and an updated current cratering rate. In *Eighth International Conference on Mars*, volume 1791, page 1007.

Daubar, I., McEwen, A., Byrne, S., Kreslavsky, M., Saper, L., Kennedy, M., and Golombek, M. (2015). Current state of knowledge of modern martian cratering. *Issues in Crater Studies and the Dating of Planetary Surfaces*, 1841:9007.

Daubar, I. J., Dundas, C. M., Byrne, S., Geissler, P., Bart, G., McEwen, A. S., Russell, P. S., Chojnacki, M., and Golombek, M. (2016). Changes in blast zone albedo patterns around new martian impact craters. *Icarus*, 267:86–105.

Drozd, R., Hohenberg, C., Morgan, C., and Ralston, C. (1974). Cosmic-ray exposure history at the apollo 16 and other lunar sites: lunar surface dynamics. *Geochimica et Cosmochimica Acta*, 38(10):1625–1642.

Duke, M., Woo, C., Sellers, G., Bird, M., and Finkelman, R. (1970). Genesis of lunar soil at tranquillity base. In *Geochimica et Cosmochimica Acta Supplement, Volume 1.*

Proceedings of the Apollo 11 Lunar Science Conference held 5-8 January, 1970 in Houston, TX. Volume 1: Mineraolgy and Petrology. Edited by AA Levinson. New York: Pergammon Press, 1970., p. 347, volume 1, page 347.

Dundas, C. M. and McEwen, A. S. (2007). Rays and secondary craters of tycho. *Icarus*, 186(1):31–40.

Edwards, C., Nowicki, K., Christensen, P., Hill, J., Gorelick, N., and Murray, K. (2011). Mosaicking of global planetary image datasets: 1. techniques and data processing for thermal emission imaging system (themis) multi-spectral data. *Journal of Geophysical Research: Planets*, 116(E10).

Elder, C. M., Douglass, B., Ghent, R., Hayne, P., Williams, J.-P., Bandfield, J., and Costello, E. (2019). The subsurface coherent rock content of the moon as revealed by cold-spot craters. *Journal of Geophysical Research: Planets*, 124(12):3373–3384.

Elder, C. M., Hayne, P. O., Piqueux, S., Bandfield, J., Williams, J.-P., Ghent, R. R., and Paige, D. A. (2016). The lunar rock size frequency distribution from diviner infrared measurements. In *AGU Fall Meeting Abstracts*, pages P24A–04.

Eugster, O. (1999). Chronology of dimict breccias and the age of south ray crater at the apollo 16 site. *Meteoritics & Planetary Science*, 34(3):385–391.

Eugster, O., Herzog, G., Marti, K., and Caffee, M. (2006). Irradiation records, cosmic-ray exposure ages, and transfer times of meteorites. *Meteorites and the early solar system II*, 943:829–851.

Fassett, C. I., Beyer, R. A., Deutsch, A. N., Hirabayashi, M., Leight, C., Mahanti, P., Nypaver, C. A., Thomson, B. J., and Minton, D. A. (2022). Topographic diffusion revisited: Small crater lifetime on the moon and implications for volatile exploration. *Journal of Geophysical Research: Planets*, page e2022JE007510.

Fassett, C. I. and Thomson, B. J. (2014). Crater degradation on the lunar maria: Topographic diffusion and the rate of erosion on the moon. *Journal of Geophysical Research: Planets*, 119(10):2255–2271.

Foote, E. J., Paige, D. A., Shepard, M. K., Johnson, J. R., and Biggar, S. (2020). The bidirectional and directional hemispheric reflectance of apollo 11 and 16 soils: Laboratory and diviner measurements. *Icarus*, 336:113456.

Fountain, J. A. and West, E. A. (1970). Thermal conductivity of particulate basalt as a function of density in simulated lunar and martian environments. *Journal of Geophysical Research*, 75(20):4063–4069.

Frey, H. and Schultz, R. A. (1988). Large impact basins and the mega-impact origin for the crustal dichotomy on mars. *Geophysical Research Letters*, 15(3):229–232.

Frizzell, E. and Hartzell, C. M. (2022). Simulations of a laterally propagating rarefaction shockwave at the interface between a randomly packed 3d cohesive granular assembly and vacuum in microgravity. In *AGU Fall Meeting Abstracts*, volume 2022, pages EP32D–1335.

Gault, D., Hörz, F., Brownlee, D., and Hartung, J. (1974). Mixing of the lunar regolith. In *In: Lunar Science Conference, 5th, Houston, Tex., March 18-22, 1974, Proceedings. Volume 3.(A75-39540 19-91) New York, Pergamon Press, Inc., 1974, p. 2365-2386.*, volume 5, pages 2365–2386.

Ghent, R. R., Hayne, P. O., Bandfield, J. L., Campbell, B. A., Allen, C. C., Carter, L. M., and Paige, D. A. (2014). Constraints on the recent rate of lunar ejecta breakdown and implications for crater ages. *Geology*, 42(12):1059–1062.

Greenhagen, B. T., Bandfield, J., Bowles, N. E., Hayne, P. O., Sefton-Nash, E., Warren, T., and Paige, D. A. (2017). Sideways views of the moon: Mapping directional thermal emission with diviner. In *AGU Fall Meeting Abstracts*, volume 2017, pages P41D–2850.

Greenhagen, B. T., Lucey, P. G., Bandfield, J. L., Hayne, P. O., Williams, J.-P., and Paige, D. (2011). The diviner lunar radiometer compositional data products: Description and examples. In *Lunar and Planetary Science Conference Proceedings*, volume 42, page 2679.

Greenhagen, B. T., Lucey, P. G., Wyatt, M. B., Glotch, T. D., Allen, C. C., Arnold, J. A., Bandfield, J. L., Bowles, N. E., Hanna, K. L. D., Hayne, P. O., et al. (2010). Global silicate mineralogy of the moon from the diviner lunar radiometer. *Science*, 329(5998):1507–1509.

Greenhagen, B. T., Neish, C. D., Williams, J.-P., Cahill, J. T., Ghent, R. R., Hayne, P. O., Lawrence, S. J., Petro, N. E., and Bandfield, J. L. (2016). Origin of the anomalously rocky appearance of tsiolkovskiy crater. *Icarus*, 273:237–247.

Grieve, R. A. and Shoemaker, E. M. (1994). The record of past impacts on earth. *Hazards due to comets and asteroids*, pages 417–462.

Haase, I., Wählisch, M., Gläser, P., Oberst, J., and Robinson, M. S. (2019). Coordinates and maps of the apollo 17 landing site. *Earth and Space Science*, 6(1):59–95.

Harris, A. W. and Ward, W. R. (1982). Dynamical constraints on the formation and evolution of planetary bodies. *Annual review of earth and planetary sciences*, 10(1):61–108.

Hartmann, W. and Daubar, I. (2017). Martian cratering 11. utilizing decameter scale crater populations to study martian history. *Meteoritics & Planetary Science*, 52(3):493–510.

Hartmann, W. K. (1984). Does crater "saturation equilibrium" occur in the solar system? *Icarus*, 60(1):56–74.

Hartmann, W. K. (2005). Martian cratering 8: Isochron refinement and the chronology of mars. *Icarus*, 174(2):294–320.

Hartmann, W. K., Daubar, I. J., Popova, O., and Joseph, E. C. (2018). Martian cratering 12. utilizing primary crater clusters to study crater populations and meteoroid properties. *Meteoritics & Planetary Science*, 53(4):672–686.

Hartmann, W. K. and Neukum, G. (2001). Cratering chronology and the evolution of mars. In *Chronology and Evolution of Mars: Proceedings of an ISSI Workshop, 10–14 April 2000, Bern, Switzerland*, pages 165–194. Springer.

Hawke, B. R., Blewett, D. T., Lucey, P. G., Smith, G., Bell III, J. F., Campbell, B. A., and Robinson, M. S. (2004). The origin of lunar crater rays. *Icarus*, 170(1):1–16.

Hayne, P. O., Bandfield, J. L., Siegler, M. A., Vasavada, A. R., Ghent, R. R., Williams, J.-P., Greenhagen, B. T., Aharonson, O., Elder, C. M., Lucey, P. G., et al. (2017). Global regolith thermophysical properties of the moon from the diviner lunar radiometer experiment. *Journal of Geophysical Research: Planets*, 122(12):2371–2400.

Helbig, N., Löwe, H., and Lehning, M. (2009). Radiosity approach for the shortwave surface radiation balance in complex terrain. *Journal of the Atmospheric Sciences*, 66(9):2900–2912.

Hemingway, B. S., Krupka, K. M., and Robie, R. A. (1981). Heat capacities of the alkali feldspars between 350 and 1000 k from differential scanning calorimetry, the thermodynamic functions of the alkali feldspars from 298.15 to 1400 k, and the reaction quartz+ jadeite= analbite. *American Mineralogist*, 66(11-12):1202–1215.

Hodges, C., Muehlberger, W. R., and Ulrich, G. E. (1973). Geologic setting of apollo 16. In *Lunar and Planetary Science Conference Proceedings*, volume 4, page 1.

Holsapple, K. A. (1993). The scaling of impact processes in planetary sciences. *Annual review of earth and planetary sciences*, 21(1):333–373.

Horai, K.-I. and Simmons, G. (1972). Thermal property measurements on lunar material returned by apollo 11 and 12 missions. *Progress in Astronautics and Aeronautics*, 28:243–267.

Horvath, T., Hayne, P. O., and Paige, D. A. (2019). Thermal environments and illumination

in lunar pits and lava tubes. In *AGU Fall Meeting Abstracts*, volume 2019, pages P31C–3454.

Horvath, T., Hayne, P. O., and Paige, D. A. (2022). Thermal and illumination environment of lunar pits and caves: Models and observations from the diviner lunar radiometer experiment. *Geophysical Research Letters*.

Housen, K. R. and Holsapple, K. A. (2011). Ejecta from impact craters. *Icarus*, 211(1):856–875.

Howard, K. A., Wilhelms, D., and Scott, D. (1974). Lunar basin formation and highland stratigraphy. *Reviews of Geophysics*, 12(3):309–327.

Ingersoll, A. P., Svitek, T., and Murray, B. C. (1992). Stability of polar frosts in spherical bowl-shaped craters on the moon, mercury, and mars. *Icarus*, 100(1):40–47.

Ivanov, B. (2006). Earth/moon impact rate comparison: Searching constraints for lunar secondary/primary cratering proportion. *Icarus*, 183(2):504–507.

Ivanov, B., Melosh, H., McEwen, A., and Team, H. (2014). New small impact craters in high resolution hirise images - iv. In *Annual Lunar and Planetary Science Conference*, volume 45.

Ivanov, B. A. (2001). Mars/moon cratering rate ratio estimates. *Space Science Reviews*, 96(1-4):87–104.

Jenniskens, P. (2018). Review of asteroid-family and meteorite-type links. *Proceedings of the International Astronomical Union*, 14(A30):9–12.

Jhoti, E., Powell, T., and Paige, D. (2023). A semi-analytical model for the thermal emission phase function of the moon. In *Lunar and Planetary Science Conference Proceedings*, volume 54, page 2919.

Keihm, S. and Langseth Jr, M. (1973). Surface brightness temperatures at the apollo 17 heat flow site: Thermal conductivity of the upper 15 cm of regolith. In *Proceedings of the Lunar Science Conference, vol. 4, p. 2503*, volume 4, page 2503.

Keihm, S., Peters, K., Langseth, M., and Chute Jr, J. (1973). Apollo 15 measurement of lunar surface brightness temperatures thermal conductivity of the upper 1 1/2 meters of regolith. *Earth and Planetary Science Letters*, 19(3):337–351.

Kirchoff, M. R., Chapman, C. R., Marchi, S., Curtis, K. M., Enke, B., and Bottke, W. F. (2013). Ages of large lunar impact craters and implications for bombardment during the moon's middle age. *Icarus*, 225(1):325–341.

Kirchoff, M. R., Marchi, S., Bottke, W. F., Chapman, C. R., and Enke, B. (2021). Suggestion that recent (less than 3 ga) flux of kilometer and larger impactors in the earth-moon system has not been constant. *Icarus*, 355:114110.

König, B. (1977). Investigations of primary and secondary impact structures on the moon and laboratory experiments to study the ejecta of secondary particles. Technical report, NASA.

Kreiter, T. (1960). Dating lunar surface features by using crater frequencies. *Publications of the Astronomical Society of the Pacific*, 72(428):393–398.

Li, L. and Mustard, J. F. (2005). On lateral mixing efficiency of lunar regolith. *Journal of Geophysical Research: Planets*, 110(E11).

LRO Project (2008). A standardized lunar coordinate system for the lunar reconnaissance orbiter. Technical report, NASA Goddard Space Flight Center.

Lucey, P. G., Greenhagen, B. T., Donaldson Hanna, K., Bowles, N., Flom, A., and Paige, D. A. (2021). Christiansen feature map from the lunar reconnaissance orbiter diviner lunar radiometer experiment: Improved corrections and derived mineralogy. *Journal of Geophysical Research: Planets*, 126(6):e2020JE006777.

Malin, M. C., Bell III, J. F., Cantor, B. A., Caplinger, M. A., Calvin, W. M., Clancy, R. T., Edgett, K. S., Edwards, L., Haberle, R. M., James, P. B., et al. (2007). Context camera investigation on board the mars reconnaissance orbiter. *Journal of Geophysical Research: Planets*, 112(E5).

Malin, M. C., Danielson, G., Ingersoll, A., Masursky, H., Veverka, J., Ravine, M., and Soulanille, T. (1992). Mars observer camera. *Journal of Geophysical Research: Planets*, 97(E5):7699–7718.

Malin, M. C., Edgett, K. S., Posiolova, L. V., McColley, S. M., and Dobrea, E. Z. N. (2006). Present-day impact cratering rate and contemporary gully activity on mars. *science*, 314(5805):1573–1577.

Martinez, A. and Siegler, M. (2021). A global thermal conductivity model for lunar regolith at low temperatures. *Journal of Geophysical Research: Planets*, 126(10):e2021JE006829.

Maurer, P., Eberhardt, P., Geiss, J., Grögler, N., Stettler, A., Brown, G., Peckett, A., and Krähenbühl, U. (1978). Pre-imbrian craters and basins: ages, compositions and excavation depths of apollo 16 breccias. *Geochimica et Cosmochimica Acta*, 42(11):1687–1720.

Mazarico, E., Neumann, G. A., Barker, M. K., Goossens, S., Smith, D. E., and Zuber, M. T. (2018). Orbit determination of the lunar reconnaissance orbiter: Status after seven years. *Planetary and space science*, 162:2–19.

Mazarico, E., Rowlands, D., Neumann, G., Smith, D., Torrence, M., Lemoine, F., and Zuber, M. (2012). Orbit determination of the lunar reconnaissance orbiter. *Journal of Geodesy*, 86(3):193–207.

Mazrouei, S., Ghent, R. R., Bottke, W. F., Parker, A. H., and Gernon, T. M. (2019). Earth and moon impact flux increased at the end of the paleozoic. *Science*, 363(6424):253–257.

McEwen, A. S. and Bierhaus, E. B. (2006). The importance of secondary cratering to age constraints on planetary surfaces. *Annu. Rev. Earth Planet. Sci.*, 34:535–567.

McEwen, A. S., Eliason, E. M., Bergstrom, J. W., Bridges, N. T., Hansen, C. J., Delamere, W. A., Grant, J. A., Gulick, V. C., Herkenhoff, K. E., Keszthelyi, L., et al. (2007). Mars reconnaissance orbiter's high resolution imaging science experiment (hirise). *Journal of Geophysical Research: Planets*, 112(E5).

McEwen, A. S., Moore, J. M., and Shoemaker, E. M. (1997). The phanerozoic impact cratering rate: Evidence from the farside of the moon. *Journal of Geophysical Research: Planets*, 102(E4):9231–9242.

McEwen, A. S., Preblich, B. S., Turtle, E. P., Artemieva, N. A., Golombek, M. P., Hurst, M., Kirk, R. L., Burr, D. M., and Christensen, P. R. (2005). The rayed crater zunil and interpretations of small impact craters on mars. *Icarus*, 176(2):351–381.

McKay, D., Morrison, D., Clanton, U., Ladle, G., and Lindsay, J. (1971). Apollo 12 soil and breccia. In *Lunar and Planetary Science Conference Proceedings*, volume 2, page 755.

Melosh, H. J. (1989). Impact cratering: A geologic process. *New York: Oxford University Press; Oxford: Clarendon Press.*

Mendell, W. and Low, F. (1974). Preliminary results of the apollo 17 infrared scanning radiometer. *The moon*, 9(1-2):97–103.

Mendell, W. and Low, F. (1975). Infrared orbital mapping of lunar features. In *Lunar and Planetary Science Conference Proceedings*, volume 6, pages 2711–2719.

Meyer, H., Denevi, B., Boyd, A., and Robinson, M. (2016). The distribution and origin of lunar light plains around orientale basin. *Icarus*, 273:135–145.

Mitchell, J., Carrier III, W. D., Houston, W. N., Scott, R. F., Bromwell, L. G., Durgunoglu, H., Hovland, H. J., Treadwell, D. D., and Costes, N. C. (1972). Soil mechanics. *Apollo 16 Prelim. Sci. Rept.*

Mitchell, J., Houston, W., Carrier III, W., and Costes, N. (1974). Apollo soil mechanics experiment s-200, final report. *University of California Space Sciences Laboratory Series*, 15(7).

Morris, R. V. (1978). In situ reworking/gardening/of the lunar surface-evidence from the apollo cores. In *Lunar and planetary science conference proceedings*, volume 9, pages 1801–1811.

Muehlberger, W., Batson, R., Boudette, E., Duke, C., Eggleton, R., Elston, D., England, A., Freeman, V., Hait, M., Hall, T., et al. (1972). Preliminary geologic investigation of the apollo 16 landing site. *Apollo 16 Prelim. Sci. Rept.*

Namiq, L. I. (1970). *Stress-deformation study of a simulated lunar soil*. University of California, Berkeley.

Nesvornỳ, D., Vokrouhlickỳ, D., Morbidelli, A., and Bottke, W. F. (2009). Asteroidal source of l chondrite meteorites. *Icarus*, 200(2):698–701.

Neukum, G. (1983). Meteoritenbombardement und datierung planetarer oberflachen. *Habilitation Dissertation for Faculty Membership, Ludwig-Maximilians-Univ.*

Neukum, G. and Ivanov, B. (1994). Crater size distributions and impact probabilities on earth from lunar, terrestrial-planet, and asteroid cratering data. *Hazards due to Comets and Asteroids*, 359(1):359–416.

Neukum, G., Ivanov, B. A., and Hartmann, W. K. (2001). Cratering records in the inner solar system in relation to the lunar reference system. In *Chronology and Evolution of Mars: Proceedings of an ISSI Workshop, 10–14 April 2000, Bern, Switzerland*, pages 55–86. Springer.

Neukum, G., König, B., and Arkani-Hamed, J. (1975). A study of lunar impact crater size-distributions. *The moon*, 12(2):201–229.

Nimmo, F., Hart, S., Korycansky, D., and Agnor, C. (2008). Implications of an impact origin for the martian hemispheric dichotomy. *Nature*, 453(7199):1220–1223.

Oberbeck, V. R. (1971a). Laboratory simulation of impact cratering with high explosives. *Journal of Geophysical Research*, 76(23):5732–5749.

Oberbeck, V. R. (1971b). A mechanism for the production of lunar crater rays. *The moon*, 2(3):263–278.

Oberbeck, V. R. (1975). The role of ballistic erosion and sedimentation in lunar stratigraphy. *Reviews of Geophysics*, 13(2):337–362.

Öpik, E. (1960). The lunar surface as an impact counter. *Monthly Notices of the Royal Astronomical Society*, 120(5):404–411.

Paige, D. A., Bachman, J. E., and Keegan, K. D. (1994). Thermal and albedo mapping of the polar regions of mars using viking thermal mapper observations: 1. north polar region. *Journal of Geophysical Research: Planets*, 99(E12):25959–25991.

Paige, D. A., Foote, M., Greenhagen, B., Schofield, J., Calcutt, S., Vasavada, A., Preston, D., Taylor, F., Allen, C., Snook, K., et al. (2010a). The lunar reconnaissance orbiter diviner lunar radiometer experiment. *Space Science Reviews*, 150(1):125–160.

Paige, D. A., Siegler, M. A., Zhang, J. A., Hayne, P. O., Foote, E. J., Bennett, K. A., Vasavada, A. R., Greenhagen, B. T., Schofield, J. T., McCleese, D. J., et al. (2010b). Diviner lunar radiometer observations of cold traps in the moon's south polar region. *science*, 330(6003):479–482.

Paige, D. A., Sullivan, M. T., and Williams, J.-P. (2022). Lunar reconnaissance orbiter diviner derived data bundle 1. *NASA Planetary Data System*.

Pasckert, J. H., Hiesinger, H., and van der Bogert, C. H. (2015). Small-scale lunar farside volcanism. *Icarus*, 257:336–354.

Petro, N. E. and Pieters, C. M. (2006). Modeling the provenance of the apollo 16 regolith. *Journal of Geophysical Research: Planets*, 111(E9).

Petro, N. E. and Pieters, C. M. (2008). The lunar-wide effects of basin ejecta distribution on the early megaregolith. *Meteoritics & Planetary Science*, 43(9):1517–1529.

Popova, O., Nemtchinov, I., and Hartmann, W. K. (2003). Bolides in the present and past martian atmosphere and effects on cratering processes. *Meteoritics & Planetary Science*, 38(6):905–925.

Powell, T., Horvath, T., Robles, V. L., Williams, J.-P., Hayne, P., Gallinger, C., Greenhagen, B., McDougall, D., and Paige, D. (2023). High-resolution nighttime temperature and rock abundance mapping of the moon using the diviner lunar radiometer experiment with a model for topographic removal. *Journal of Geophysical Research: Planets*, page e2022JE007532.

Powell, T., Rubanenko, L., and Paige, D. (2020). Modeling ice stability in small permanently shadowed regions on the moon. In *Lunar Surface Science Workshop*, volume 2241, page 5169.

Powell, T., Rubanenko, L., and Paige, D. A. (2019). Warming of the martian deep subsurface by topography. In *AGU Fall Meeting Abstracts*, volume 2019, pages P41C–3468.

Powell, T. M. (2022). Replication data for: High-resolution nighttime temperature and rock abundance mapping of the moon using the diviner lunar radiometer experiment with a model for topographic removal.

Powell, T. M., Rubanenko, L., Williams, J.-P., and Paige, D. A. (2021). The role of secondary craters on martian crater chronology. In *Mars Geological Enigmas*, pages 123–145. Elsevier.

Preblich, B. S., McEwen, A. S., and Studer, D. M. (2007). Mapping rays and secondary craters from the martian crater zunil. *Journal of Geophysical Research: Planets*, 112(E5).

Quantin, C., Popova, O., Hartmann, W. K., and Werner, S. C. (2016). Young martian crater gratteri and its secondary craters. *Journal of Geophysical Research: Planets*, 121(7):1118–1140.

Reed, V. (1981). D3. geology of areas near south ray and baby ray craters. *Geology of the Apollo*, 16.

Robbins, S. J. (2014). New crater calibrations for the lunar crater-age chronology. *Earth and Planetary Science Letters*, 403:188–198.

Robbins, S. J. (2019). A new global database of lunar impact craters¿ 1–2 km: 1. crater locations and sizes, comparisons with published databases, and global analysis. *Journal of Geophysical Research: Planets*, 124(4):871–892.

Robbins, S. J. and Hynek, B. M. (2011a). Distant secondary craters from lyot crater, mars, and implications for surface ages of planetary bodies. *Geophysical research letters*, 38(5).

Robbins, S. J. and Hynek, B. M. (2011b). Secondary crater fields from 24 large primary craters on mars: Insights into nearby secondary crater production. *Journal of Geophysical Research: Planets*, 116(E10).

Robbins, S. J. and Hynek, B. M. (2012). A new global database of mars impact craters 1 km: 1. database creation, properties, and parameters. *Journal of Geophysical Research: Planets*, 117(E5).

Robbins, S. J. and Hynek, B. M. (2014). The secondary crater population of mars. *Earth and Planetary Science Letters*, 400:66–76.

Roberts, W. A. (1964). Secondary craters. *Icarus*, 3(4):348–364.

Rogoszinski, Z. and Hamilton, D. P. (2021). Tilting uranus: Collisions versus spin–orbit resonance. *The Planetary Science Journal*, 2(2):78.

Rosenburg, M. A., Aharonson, O., Head, J. W., Kreslavsky, M. A., Mazarico, E., Neumann, G. A., Smith, D. E., Torrence, M. H., and Zuber, M. T. (2011). Global surface slopes and roughness of the moon from the lunar orbiter laser altimeter. *Journal of Geophysical Research: Planets*, 116(E2).

Rubanenko, L., Powell, T. M., Williams, J.-P., Daubar, I., Edgett, K. S., and Paige, D. A. (2021). Challenges in crater chronology on mars as reflected in jezero crater. In *Mars Geological Enigmas*, pages 97–122. Elsevier.

Rubanenko, L., Schorghofer, N., Greenhagen, B. T., and Paige, D. A. (2020). Equilibrium temperatures and directional emissivity of sunlit airless surfaces with applications to the moon. *Journal of Geophysical Research: Planets*, 125(6):e2020JE006377.

Sakatani, N., Ogawa, K., Arakawa, M., and Tanaka, S. (2018). Thermal conductivity of lunar regolith simulant jsc-1a under vacuum. *Icarus*, 309:13–24.

Schmidt, R. M. and Holsapple, K. A. (1982). Estimates of crater size for large-body impact: Gravity-scaling results. *Geological Implications of Impacts of Large Asteroids and Comets on the Earth*, 190:93–102.

Schmidt, R. M. and Housen, K. R. (1987). Some recent advances in the scaling of impact and explosion cratering. *International Journal of Impact Engineering*, 5(1-4):543–560.

Schultz, P. H. and Singer, J. (1980). A comparison of secondary craters on the moon, mercury, and mars. In *Lunar and Planetary Science Conference Proceedings*, volume 11.

Shoemaker, E., Hackman, R., and Eggleton, R. (1963). Interplanetary correlation of geologic time. *Adv. Astronaut. Sci.*, 8:70–89.

Shoemaker, E. M. (1965). Preliminary analysis of the fine structure of the lunar surface in mare cognitum. *The nature of the lunar surface*, 65:23.

Shoemaker, E. M. (1998). Impact cratering through geologic time. *Journal of the Royal Astronomical Society of Canada, Vol. 92, p. 297*, 92:297.

Simon, S., Papike, J., Shearer, C., and Laul, J. (1983). Petrology of the apollo 11 highland component. *Journal of Geophysical Research: Solid Earth*, 88(S01):B103–B138.

Singer, K. N., Jolliff, B. L., and McKinnon, W. B. (2020). Lunar secondary craters and estimated ejecta block sizes reveal a scale-dependent fragmentation trend. *Journal of Geophysical Research: Planets*, 125(8):e2019JE006313.

Smith, D. E., Zuber, M. T., Frey, H. V., Garvin, J. B., Head, J. W., Muhleman, D. O., Pettengill, G. H., Phillips, R. J., Solomon, S. C., Zwally, H. J., et al. (2001). Mars orbiter laser altimeter: Experiment summary after the first year of global mapping of mars. *Journal of Geophysical Research: Planets*, 106(E10):23689–23722.

Soderblom, L., Condit, C., West, R. A., Herman, B., and Kreidler, T. (1974). Martian planetwide crater distributions: Implications for geologic history and surface processes. *Icarus*, 22(3):239–263.

Speyerer, E., Wagner, R., Povilaitis, R., Robinson, M., Martin, A., and Denevi, B. (2020). Constraining the contemporary impact cratering rate and understanding the impact process with temporal and photometric observations. In *Lunar and Planetary Science Conference Proceedings*, volume 51, page 2369.

Speyerer, E. J., Povilaitis, R. Z., Robinson, M. S., Thomas, P. C., and Wagner, R. V. (2016). Quantifying crater production and regolith overturn on the moon with temporal imaging. *Nature*, 538(7624):215–218.

Stöffler, D. and Ryder, G. (2001). Stratigraphy and isotope ages of lunar geologic units: Chronological standard for the inner solar system. *Space Science Reviews*, 96(1-4):9–54.

Sullivan, M., Paige, D., Arvidson, R., and Grayzeck, E. (2013). Lunar reconnaissance orbiter diviner lunar radiometer experiment: Reduced data record and derived products software interface specification.

Terada, K., Morota, T., and Kato, M. (2020). Asteroid shower on the earth-moon system immediately before the cryogenian period revealed by kaguya. *Nature Communications*, 11(1):3453.

Tooley, C. R., Houghton, M. B., Saylor, R. S., Peddie, C., Everett, D. F., Baker, C. L., and Safdie, K. N. (2010). Lunar reconnaissance orbiter mission and spacecraft design. *Space Science Reviews*, 150(1):23–62.

Tornabene, L. L., Moersch, J. E., McSween Jr, H. Y., McEwen, A. S., Piatek, J. L., Milam, K. A., and Christensen, P. R. (2006). Identification of large (2–10 km) rayed craters on mars in themis thermal infrared images: Implications for possible martian meteorite source regions. *Journal of Geophysical Research: Planets*, 111(E10).

Ulrich, G., Moore, H., Reed, V., Wolfe, E., and Larson, K. (1975). Distribution of ejecta from south ray crater. In *Lunar and Planetary Science Conference*, volume 6.

Vasavada, A. R., Bandfield, J. L., Greenhagen, B. T., Hayne, P. O., Siegler, M. A., Williams, J.-P., and Paige, D. A. (2012). Lunar equatorial surface temperatures and regolith properties from the diviner lunar radiometer experiment. *Journal of Geophysical Research: Planets*, 117(E12).

Vickery, A. (1986). Size-velocity distribution of large ejecta fragments. *Icarus*, 67(2):224–236.

Vickery, A. M. (1987). Variation in ejecta size with ejection velocity. *Geophysical Research Letters*, 14(7):726–729.

Vokrouhlickỳ, D., Bottke, W. F., and Nesvornỳ, D. (2017). Forming the flora family: Implications for the near-earth asteroid population and large terrestrial planet impactors. *The Astronomical Journal*, 153(4):172.

Warren, T., Bowles, N., Donaldson Hanna, K., and Bandfield, J. (2019). Modeling the angular dependence of emissivity of randomly rough surfaces. *Journal of Geophysical Research: Planets*, 124(2):585–601.

Watkins, R. N., Jolliff, B. L., Mistick, K., Fogerty, C., Lawrence, S. J., Singer, K. N., and Ghent, R. R. (2019). Boulder distributions around young, small lunar impact craters and implications for regolith production rates and landing site safety. *Journal of Geophysical Research: Planets*, 124(11):2754–2771.

Werner, S. C., Ivanov, B. A., and Neukum, G. (2009). Theoretical analysis of secondary cratering on mars and an image-based study on the cerberus plains. *Icarus*, 200(2):406–417.

Wilhelms, D., Oberbeck, V., and Aggarwal, H. (1978). Size-frequency distributions of primary and secondary lunar impact craters. In *In: Lunar and Planetary Science Conference, 9th, Houston, Tex., March 13-17, 1978, Proceedings. Volume 3.(A79-39253 16-91) New York, Pergamon Press, Inc., 1978, p. 3735-3762.*, volume 9, pages 3735–3762.

Wilhelms, D. E. and Squyres, S. W. (1984). The martian hemispheric dichotomy may be due to a giant impact. *Nature*, 309(5964):138–140.

Williams, J.-P. (2018). Modification of the martian surface by impact cratering. In *Dynamic Mars*, pages 363–386. Elsevier.

Williams, J.-P., Bandfield, J., Paige, D., Powell, T., Greenhagen, B., Taylor, S., Hayne, P., Speyerer, E., Ghent, R., and Costello, E. (2018a). Lunar cold spots and crater production on the moon. *Journal of Geophysical Research: Planets*, 123(9):2380–2392.

Williams, J.-P., Greenhagen, B., Paige, D., Schorghofer, N., Sefton-Nash, E., Hayne, P., Lucey, P., Siegler, M., and Aye, K. M. (2019). Seasonal polar temperatures on the moon. *Journal of Geophysical Research: Planets*, 124(10):2505–2521.

Williams, J.-P., Greenhagen, B. T., Bennett, K. A., Paige, D. A., Kumari, N., Ahrens, C. J., Rubanenko, L., Powell, T. M., Prem, P., Blewett, D. T., Russell, P. S., Hayne, P. O., and Sullivan, M. T. (2022). Temperatures of the lacus mortis region of the moon. *Earth and Space Science*, 9(2).

Williams, J.-P., Paige, D., Greenhagen, B., and Sefton-Nash, E. (2017). The global surface temperatures of the moon as measured by the diviner lunar radiometer experiment. *Icarus*, 283:300–325.

Williams, J.-P., Pathare, A. V., and Aharonson, O. (2014). The production of small primary craters on mars and the moon. *Icarus*, 235:23–36.

Williams, J.-P., Petro, N. E., Greenhagen, B. T., and Neish, C. (2013). Inferred age of mare fill in tsiolkovskiy crater: Constraints on the preservation of exterior impact melt deposits. In *Lunar and Planetary Science Conference Proceedings*, volume 44, page 2756.

Williams, J.-P., Sefton-Nash, E., and Paige, D. (2016). The temperatures of giordano bruno crater observed by the diviner lunar radiometer experiment: Application of an effective field of view model for a point-based data set. *Icarus*, 273:205–213.

Williams, J.-P., van der Bogert, C. H., Pathare, A. V., Michael, G. G., Kirchoff, M. R., and Hiesinger, H. (2018b). Dating very young planetary surfaces from crater statistics: A review of issues and challenges. *Meteoritics & Planetary Science*, 53(4):554–582.

Winter, D. F. and Krupp, J. (1971). Directional characteristics of infrared emission from the moon. *The moon*, 2(3):279–292.

Wood, J. A. (1970). Petrology of the lunar soil and geophysical implications. *Journal of Geophysical Research*, 75(32):6497–6513.

Wood, J. A., Dickey Jr, J. S., Marvin, U. B., and Powell, B. (1970). Lunar anorthosites and a geophysical model of the moon. In *Geochimica et Cosmochimica Acta Supplement, Volume 1. Proceedings of the Apollo 11 Lunar Science Conference held 5-8 January, 1970 in Houston, TX. Volume 1: Mineraolgy and Petrology. Edited by AA Levinson. New York: Pergammon Press, 1970., p. 965*, volume 1, page 965.

Woods-Robinson, R., Siegler, M. A., and Paige, D. A. (2019). A model for the thermophysical

properties of lunar regolith at low temperatures. *Journal of Geophysical Research: Planets*, 124(7):1989–2011.

Young, J. (1940). A statistical investigation of diameter and distribution of lunar craters. *J. Brit. Astron. Assoc*, 50(9):309326.